Fermi National Accelerator Laboratory

FERMILAB-Pub-99/264-E
D0

New Showering Correction for the Jet Energy Scale at D0

Anna Goussiou
For the D0 Collaboration
SUNY, Stony Brook

Fermi National Accelerator Laboratory
P.O. Box 500, Batavia, Illinois 60510

September 1999

Operated by Universities Research Association Inc. under Contract No. DE-AC02-76CH03000 with the United States Department of Energy

NEW SHOWERING CORRECTION FOR THE JET ENERGY SCALE AT DØ

Anna Goussiou
SUNY, Stony Brook

FERMILAB-Pub-99/264-E

DØ Note # 3606

February 25, 1999

Abstract

We present a new method for deriving the showering correction for the jet energy scale at DØ, using Monte Carlo events which have been processed through a detailed simulation of the DØ detector. The similarity of Monte Carlo to collider data, for showering purposes, is established. The method provides a better control of the systematic uncertainty of the correction in the forward pseudorapidity region than previous attempts.

Contents

1 Introduction

The calibration of the jet energy measured in the DØ calorimeters [1] is performed in three main stages [2]:

1. subtraction of the offset energy. This includes energy due to spectator parton interactions (physics underlying event) and due to multiple $p\bar{p}$ interactions during the same beam crossing, residual energy from previous $p\bar{p}$ interactions, and noise from uranium decay;

2. correction of the jet energy due to the calorimeter response;

3. correction for showering effects.

Showering effects denote the mismeasurement of the jet energy due to the fixed–radius cone jet algorithm that does not fully compensate for the development of the shower of particles in the detector. When the particles originating from the hard scattering interact with the calorimeter material, a wide shower of additional particles is produced. As a result, some particles from inside (outside) the particle–level jet cone deposit a fraction of their energy outside (inside) the calorimeter–level cone. The effect is more pronounced in the forward pseudorapidity (η) region due to the shrinkage of the physical space with η ($\eta = -\ln(\tan(\theta/2))$, where θ is the polar angle of the jet relative to the proton beam).

The correction for the showering effects in the jet energy scale as determined by the CAFIX 5.1 package is based on a comparison of jet energy density profiles between the DØ data and the HERWIG Monte Carlo (MC) at the particle level. After the offset energy is subtracted from the data, the remaining energy outside the jet cone can be due to gluon emission or fragmentation at the particle level *(Physics out–of–cone)* and/or the detector showering effects, as described in the previous paragraph *(Detector out–of–cone)*. Therefore, subtracting the physics out–of–cone energy, which is derived from the HERWIG energy profiles, from the total out–of–cone energy measured in the data, yields in principal the out–of–cone energy due to detector showering. It should be noted here that the comparison of the data and MC energy profiles has been performed *after* they have both been normalized at a large distance from the jet centroid (see section 3).

The showering correction derived from the jet energy profiles involves a large number of poorly controlled systematic uncertainties. To compensate that, the systematic error on the correction has been conservatively chosen large, especially for jets in the forward pseudorapidity region and of low transverse energy (E_T). For the latter, the systematic uncertainty on the correction has been set to almost equal to the correction itself. As an example, the showering correction for jets of $2.5 < |\eta| < 3.0$ and average E_T equal to 25 GeV amounts to 10% with a systematic error of 10%. This uncertainty affects *dramatically* the uncertainty on any jet cross section measurement in the forward-η and low-E_T region.

It is evident from the above that a better control of the systematic uncertainty on the showering correction of the jet energy scale is essential for the forward–jet DØ physics analyses. To achieve that, we need a direct derivation of the showering correction, i.e. comparison of the particle energy produced inside (outside) the cone with the energy deposited outside (inside) the cone at the calorimeter level. This is possible only using

a Monte Carlo model for $p\bar{p}$ collisions combined with a detailed simulation of the DØ detector.

The data and MC samples for this analysis are described in the following section. The comparison of the data and MC jet energy profiles is discussed in section 3. The derivation of the showering correction is described and the results are presented in section 4. A closure test on the correction is presented in section 5. The new correction is compared to the one in CAFIX 5.1 in section 6. Section 7 presents the showering correction for collider data taken at $\sqrt{s} = 630$ GeV. Conclusions are discussed in the final paragraph.

2 Monte Carlo and Data Samples

HERWIG 5.9 [3] is used as the Monte Carlo generator for $p\bar{p}$ collisions. Events are generated requiring the two outgoing partons to be in opposite pseudorapidity ranges. The pseudorapidity bins are given in Table 1. There is a minimum parton p_T threshold at the generation level, which varies from 15 to 45 GeV with steps of 5 GeV, 70, 100, 150 and 200 GeV (the latter is available only in the most central pseudorapidity bin). There is no maximum parton p_T threshold (i.e. it is set equal to the beam energy of 900 GeV). The vertex distribution in HERWIG is matched with the one measured in the Run Ic $\sqrt{s} = 1800$ GeV data, i.e. the interaction point is shifted at $(x, y, z) = (-0.3, 0.2, -0.549)$ and the vertex width is set equal to 27.8 cm. Since the comparison of the Monte Carlo to the data is done, as well as the showering correction is applied, *after* the subtraction of the offset energy from the measured data energy, there is no underlying event included in the HERWIG generation. The HERWIG samples are then passed through a detailed simulation of the DØ detector based on GEANT [4]. The extremely large process time for GEANT enforces a limit on the statistics available for this analysis (100 or 125 events in each pseudorapidity and minimum-p_T bin, which results in a total of $\approx 8,850$ events for the nine η-bins and ten p_T-bins). At the analysis level, the only selection performed on the MC sample is the requirement of events with one or two jets.

The data sample, which is used only for the comparison of MC and data jet energy profiles (see section 3), consists of Run Ib data taken with various QCD jet triggers [2].

Bins in Parton Pseudorapidity			
	pseudorapidity range		pseudorapidity range
1	0.0 – 0.4	6	2.0 – 2.5
2	0.4 – 0.8	7	2.5 – 3.0
3	0.8 – 1.2	8	3.0 – 3.5
4	1.2 – 1.6	9	3.5 – 4.0
5	1.6 – 2.0		

Table 1: Bins in parton pseudorapidity at the generation level.

3 Comparison of Data and MC Jet Energy Profiles

The Monte Carlo can be used for extracting the showering correction only if and to the extend that the development of the shower of particles is modelled in a way similar to the data.

The transverse energy distribution of single pions in the calorimeter has been studied using data from the test beam, and the results have been compared to equivalent distributions in the Monte Carlo [5, 6]. Fig. 1 from ref. [5] shows the transverse hadronic shower shape produced by 100 GeV pions, as measured in end–cap IH calorimeter module, in terms of azimuth ϕ, for data (solid line) and MC (dotted line). Fig. 2 from ref. [6] shows the transverse hadronic shower shape produced by 150 GeV pions, in ECEM layer 3 and ECIH layers 1,3 and 5 at $\eta = 2.55$, as a function of the absolute distance between the impact position $r \cdot \phi_o$ of the beam track and the location of the energy deposition: $x = |x_i - x_o| = |r \cdot (\phi_i - \phi_o)|$. The solid line respesents a Lorentzian fit to the data, and the dotted line to the MC. Data points exist (i.e. the fit can be trusted) up to $x = 18$ cm in EM3, 20 cm in IH1, 24 cm in IH3, and 28 cm in IH5.

Although the test–beam studies mentioned above show a reasonably good agreement between data and Monte Carlo transverse energy distributions for single pions of a certain energy and beam direction, we need to investigate the level of agreement for jets at all energies and pseudorapidities. To that end, we extract the showering correction from the data and Monte Carlo using the method implemeted in CAFIX 5.1, i.e. measure and compare the energy profiles of the jets in MC and data. We use dijet events and calculate the energy density as measured in the calorimeter cells in rings of increasing radius (with a step of $r = 0.1$ in $\eta \times \phi$ space) from the jet centroid. The offset energy density is then subtracted from the measured data energy densities [7]. An example of the energy density profiles for central-η jets of energies between 30–50 GeV is shown in Fig. 3.

We notice that in both data and MC there remains a low but non-zero energy density even far away from the jet centroid *(baseline energy)*. This is due to color connections between the partons. Evidently, the latter are not perfectly modelled in HERWIG, since the level of the baseline is different in data and MC. Before we compare the jet energy profiles, we need to subtract the baseline energy from the measured jet energy, i.e. normalize the data and MC profiles at a large distance from the jet centroid. To validate the comparison, the baseline subtraction in the MC profiles is performed in exactly the same way as it was done in the data profiles for CAFIX 5.1. The profiles after the baseline subtraction for jets of various energies and pseudorapidities are shown in Fig. 4. We notice that there is good agreement in shape of the jet profiles between data and Monte Carlo.

To quantify the comparison between the data and MC jet energy profiles, we integrate them (after converting the energy densities to energies) and measure the fraction of the jet energy contained within the cone of radius $R = 0.7$. We consider as total energy of the jet the energy of all the calorimeter cells from the center of the centroid to the *jet limit*. The jet limit is defined as the distance where the baseline energy starts; it increases with the pseudorapidity of the jet. For the comparison between data and MC energy profiles, we need to use the same jet limit as the one used in the data in CAFIX 5.1. This is shown in Table 2, for the different η-bins.

The fraction of the jet energy contained within the $R = 0.7$ cone for jets of various

Jet Limit in Data–MC comparison					
	jet-η range	jet limit		jet-η range	jet limit
1	0.0 – 0.4	1.0	5	1.6 – 2.0	1.4
2	0.4 – 0.8	1.2	6	2.0 – 2.5	1.6
3	0.8 – 1.2	1.2	7	2.5 – 3.0	1.6
4	1.2 – 1.6	1.4	8	3.0 – 3.5	1.8

Table 2: Distance in $\eta \times \phi$ space from the jet centroid where the jet finishes, for calorimeter-level jets of various pseudorapidities.

energies and pseudorapidities in the data and Monte Carlo samples is shown in Table 3. For $|\eta| < 2.0$ the agreement is at the 1-2% level. For $2.0 < |\eta| < 2.5$ and jet energies less than 200 GeV there is still very good agreement (1-2%), whereas for energies greater than 200 GeV the agreement suddenly deteriorates to the 5-10% level. Apparently, the detector simulation can *not* be at fault for that, since in the same pseudorapidity region the agreement is very good for lower energy jets. The problem arises because the jet limit increases not only with the jet rapidity but also with the jet energy. This, in combination with the fact that for the estimation of the baseline energy in the data profiles only one point after the jet limit was used, results in a wrong estimation of the baseline energy, with a different degree of error in the data and MC; thus, the comparison is not to be trusted any more. The same effect occurs in the last pseudorapidity bin. Figures 5 and 6 demonstrate the effect: going to higher energies in the same pseudorapidity region or to higher pseudorapidities for the same jet energies, increases the error in the estimation of the baseline energy and makes the profile method, as implemented here, not dependable.

In conclusion, the showering effect, as measured with the method implemented in CAFIX 5.1, agrees between data and Monte Carlo at the 2% level.

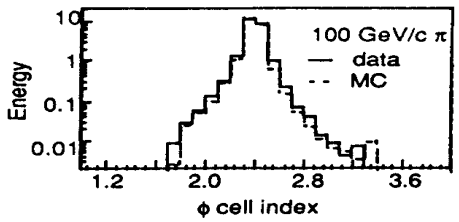

Figure 1: Transverse hadronic shower shape produced by single pions of energy 100 GeV in end-cap IH calorimeter module, for data and Monte Carlo. From ref. [5].

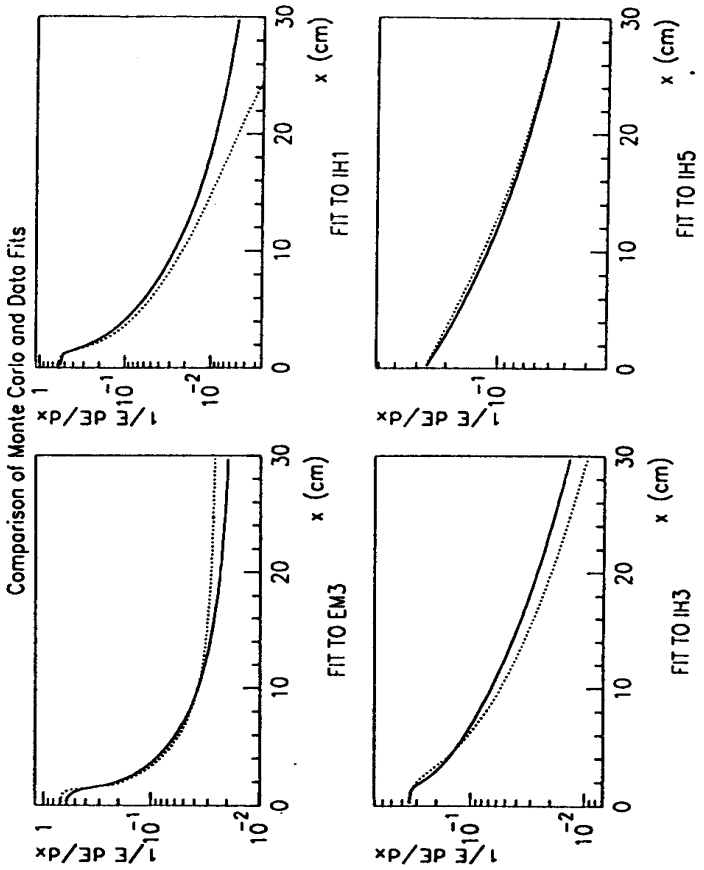

Figure 2: Lorenztian fits to the transverse shower shape produced by single pions of energy 150 GeV, in the data (solid lines) and the Monte Carlo (dotted lines). From ref. [6].

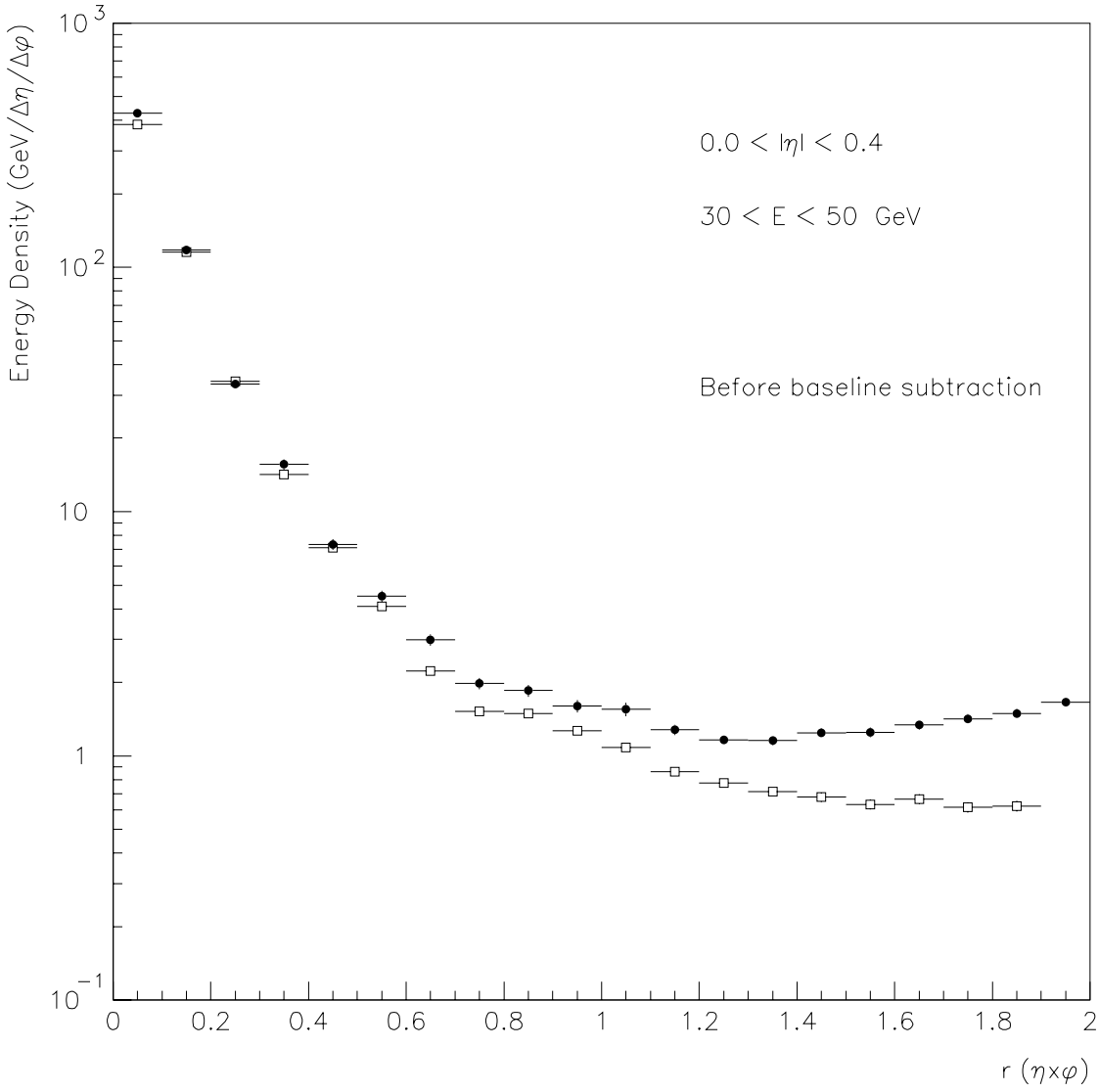

Figure 3: Energy density profiles for data (open squares) and Monte Carlo (full circles) before the baseline subtraction.

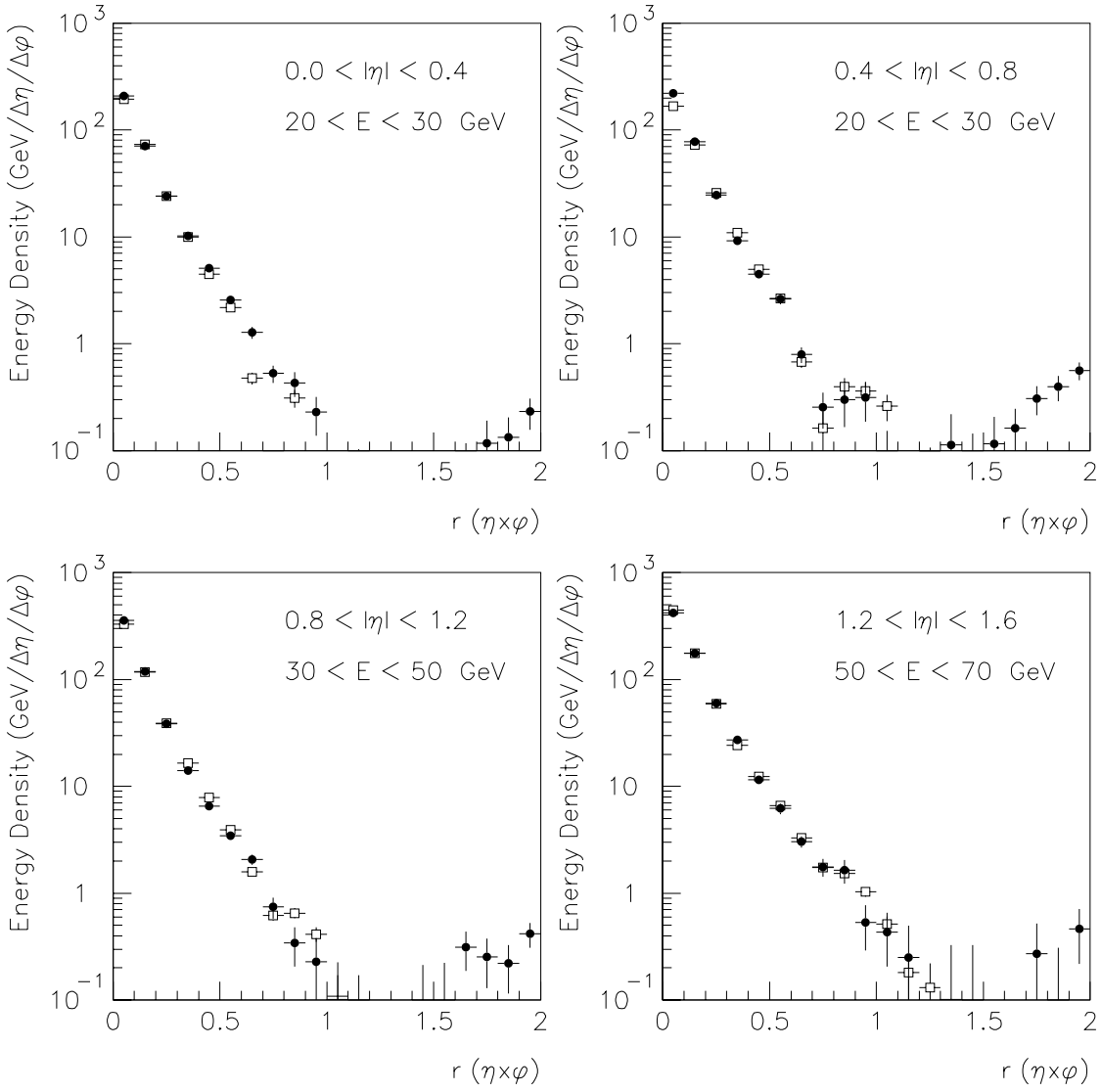

Figure 4: Energy density profiles for data (open squares) and Monte Carlo (full circles) after the baseline subtraction.

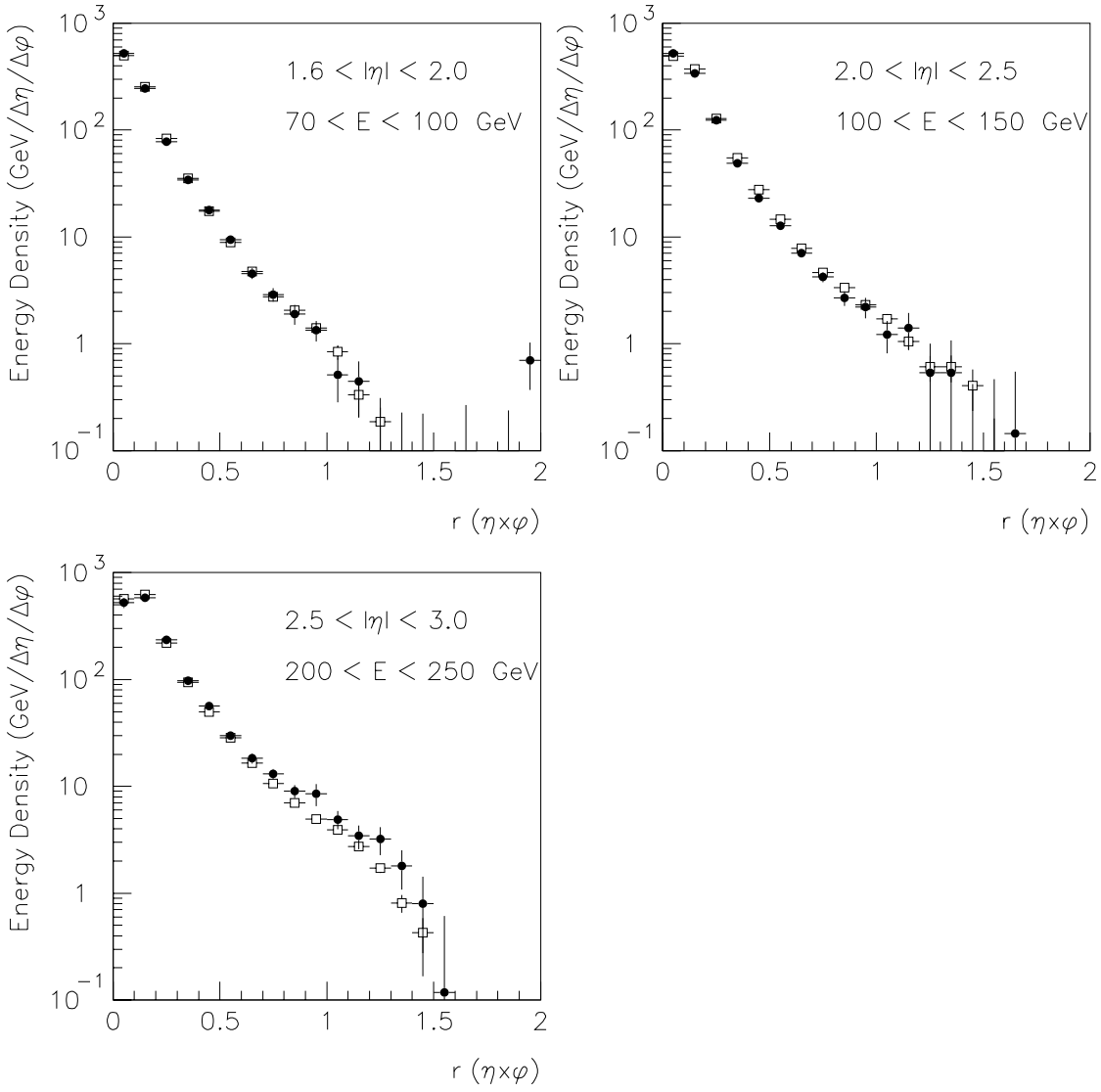

Figure 4: Energy density profiles for data (open squares) and Monte Carlo (full circles) after the baseline subtraction.

Percentage of Energy contained within the 0.7 cone					
η	E (GeV)	$<E>$ in MC (GeV)	$<E_T>$ in MC (GeV)	Data	Monte Carlo
	10 – 20	15.7	14.3	100.0	99.1
	20 – 30	24.1	22.0	99.2	97.3
	30 – 50	38.8	35.6	99.2	98.8
	50 – 70	59.3	54.4	99.2	98.3
0.0 – 0.4	70 – 100	84.4	77.8	98.5	98.1
	100 – 150	118.4	108.1	98.9	97.7
	150 – 200	182.6	168.0	99.9	97.3
	200 – 250	222.0	201.4	100.0	97.8
	250 – 300	266.2	244.9	99.3	97.3
	300 – 350				
	10 – 20	16.0	12.9	98.6	100.0
	20 – 30	25.0	19.9	96.9	97.9
	30 – 50	39.3	31.4	97.6	98.2
	50 – 70	59.1	47.0	97.5	96.8
0.4 – 0.8	70 – 100	84.0	66.4	97.5	97.0
	100 – 150	119.8	94.8	97.5	96.3
	150 – 200	171.1	137.2	96.7	95.7
	200 – 250			89.3	
	250 – 300			100.0	
	300 – 350				
	10 – 20				
	20 – 30	25.1	15.6	97.8	98.3
	30 – 50	39.3	24.4	97.4	97.9
	50 – 70	59.4	36.6	96.9	98.0
0.8 – 1.2	70 – 100	84.2	52.3	97.2	97.3
	100 – 150	122.6	77.8	97.1	95.2
	150 – 200	168.1	100.7	97.3	95.6
	200 – 250			95.2	
	250 – 300			90.2	
	300 – 350			91.7	
	10 – 20				
	20 – 30	25.6	12.1	92.0	89.8
	30 – 50	39.3	17.8	93.4	93.8
	50 – 70	59.3	26.6	94.9	96.4
1.2 – 1.6	70 – 100	81.5	35.6	94.9	93.8
	100 – 150	120.2	53.6	94.7	93.1
	150 – 200	168.9	75.4	94.6	96.1
	200 – 250	220.1	87.9	96.5	91.4
	250 – 300			100.0	
	300 – 350			100.0	

Table 3: Percentage of jet energy contained within the $R = 0.7$ cone for jets of various pseudorapidities and energies in the data and Monte Carlo samples.

Percentage of Energy contained within the 0.7 cone					
η	E (GeV)	$<E>$ in MC (GeV)	$<E_T>$ in MC (GeV)	Data	Monte Carlo
	10 – 20				
	20 – 30				
	30 – 50	42.2	13.5	88.0	91.4
	50 – 70	61.1	19.5	94.5	92.6
1.6 – 2.0	70 – 100	85.0	26.8	94.4	94.7
	100 – 150	121.3	37.2	94.6	93.8
	150 – 200	171.4	53.3	95.0	95.6
	200 – 250	225.9	69.7	96.3	93.4
	250 – 300	275.0	89.5	95.6	
	300 – 350	324.5	97.9	99.1	
	10 – 20				
	20 – 30				
	30 – 50				
	50 – 70	61.7	13.3	85.4	85.2
2.0 – 2.5	70 – 100	84.2	17.6	89.6	91.9
	100 – 150	121.9	25.1	92.0	92.4
	150 – 200	172.9	35.0	91.5	92.3
	200 – 250	221.8	42.2	95.2	85.5
	250 – 300	271.1	55.6	95.2	90.6
	300 – 350	320.8	60.5	95.4	87.9
	350 – 400			99.8	
	10 – 20				
	20 – 30				
	30 – 50				
	50 – 70				
2.5 – 3.0	70 – 100				
	100 – 150	125.5	16.2	82.9	84.8
	150 – 200	171.6	21.9	89.6	85.6
	200 – 250	224.0	28.0	89.7	85.9
	250 – 300	272.0	33.0	93.0	89.0
	300 – 350	321.0	36.8	93.0	85.7
	350 – 400			95.8	
	400 – 450			93.6	

Table 3: Percentage of jet energy contained within the $R = 0.7$ cone for jets of various pseudorapidities and energies in the data and Monte Carlo samples.

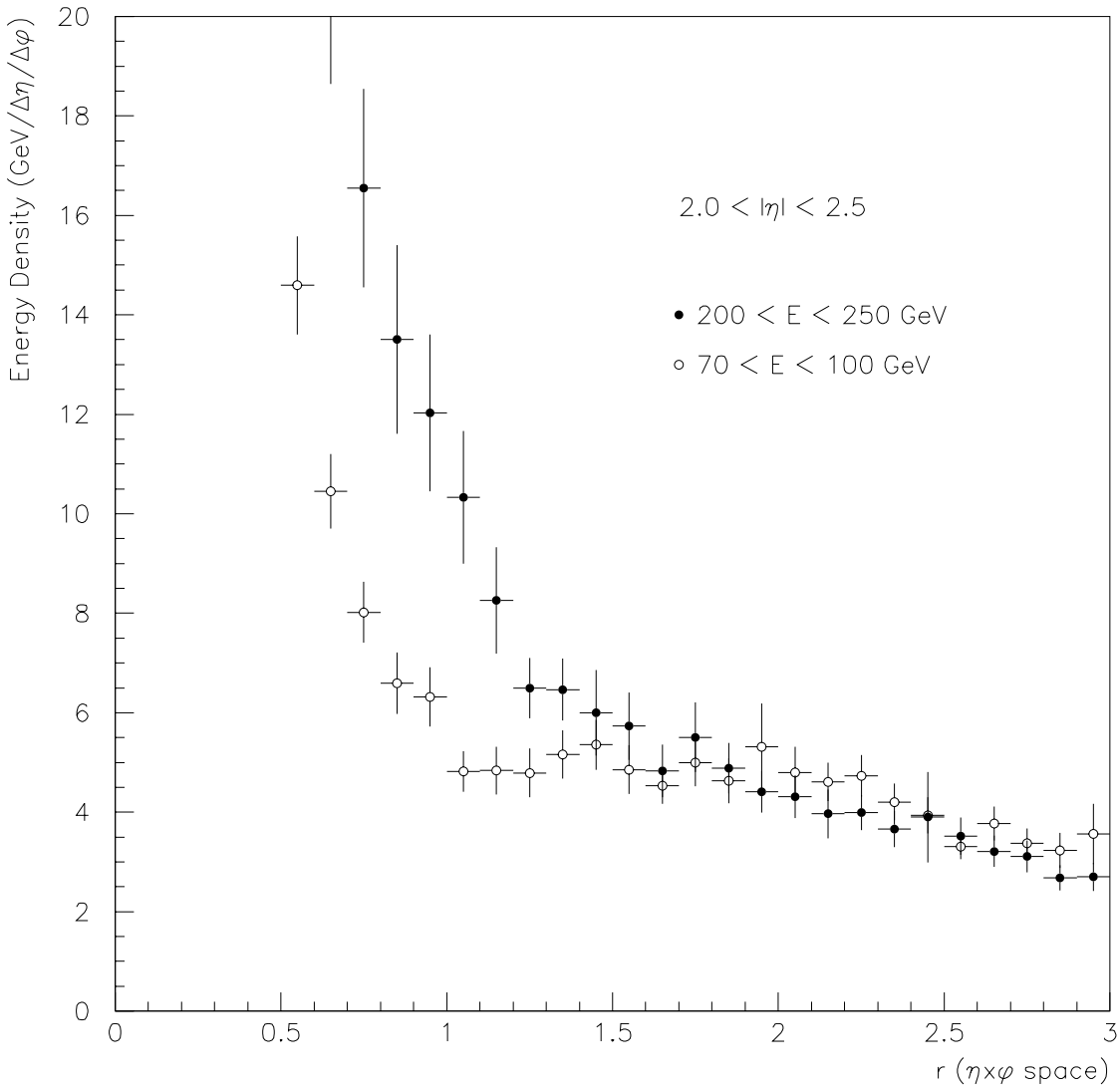

Figure 5: Energy density profiles for jets of the same pseudorapidity and different energies in the Monte Carlo, before the baseline subtraction.

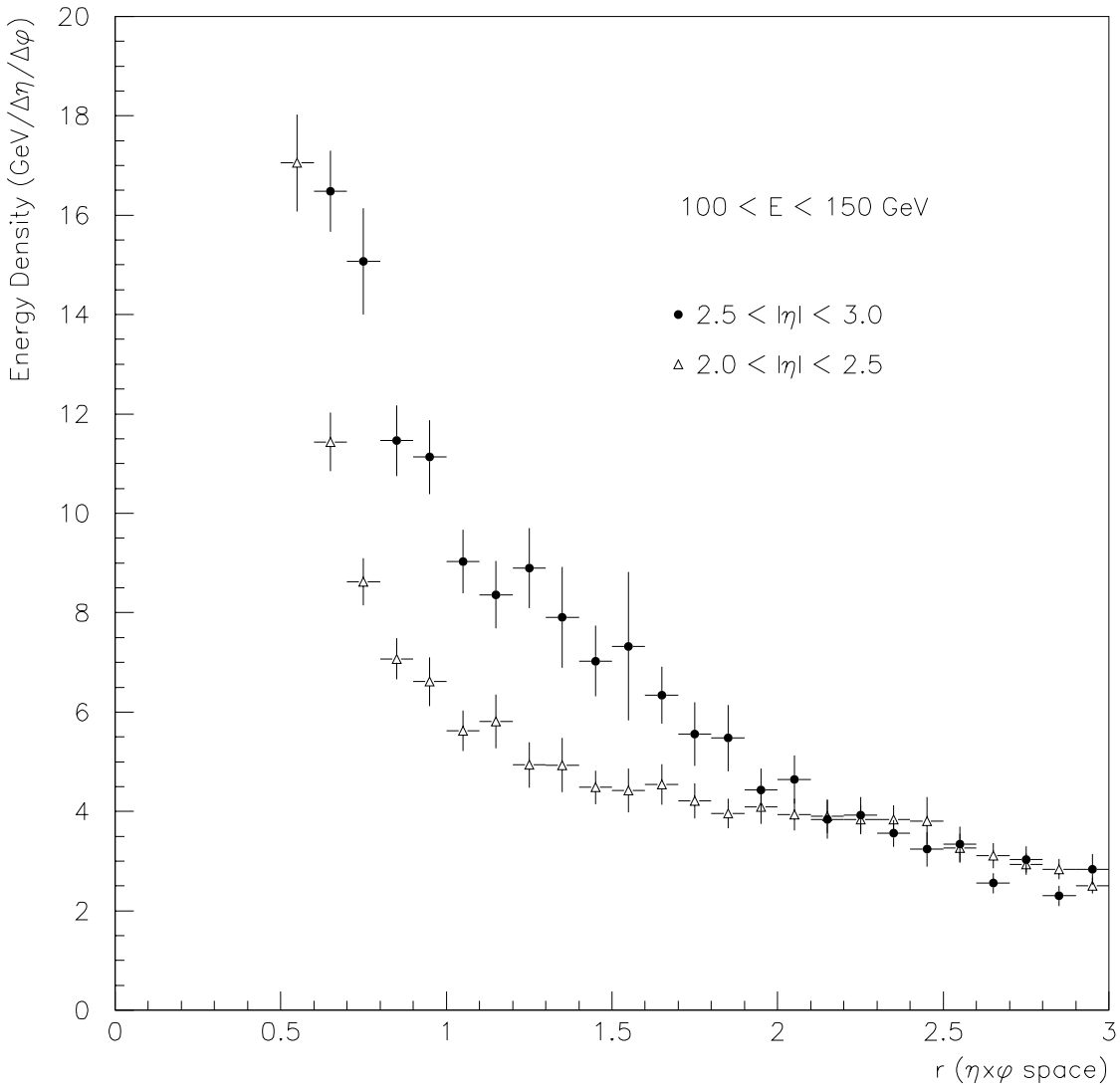

Figure 6: Energy density profiles for jets of the same energy and different pseudorapidities in the Monte Carlo, before the baseline subtraction.

4 The Showering Correction

4.1 Methodology

The derivation of a showering correction from the Monte Carlo sample is based on following each outgoing particle to the calorimeter and recording the energy it deposits in each calorimeter cell. This is done using the GCAH ZEBRA bank. The procedure is described in detail in the following:

- loop over the jets of the event at the particle level (PJET bank);
- loop over the jets of the event at the calorimeter level (JETS bank) and find the one that matches the particle jet (requiring the distance between the two to be less than 0.1 in $\eta \times \phi$ space; see Fig. 7);
- loop over the particles of the event (ISP1 bank), and for each one of them calculate its distance R_{part} from the centroid of the particle jet (see Fig. 8);
- for each particle, loop over the calorimeter cells that received energy from the particular particle (GCAH bank). Comparing the particle energy to the sum of the energies of the cells in GCAH provides the *particle energy response* (see paragraph 4.2);
- for each cell in GCAH, calculate its distance R_{cell} from the centroid of the matched calorimeter jet (see Fig. 9). As a check, we also calculate the distance $R_{part-cell}$ of each cell from the particle this cell originated from (see Fig. 10);
- the *measured* energy of the calorimeter jet is equal to the sum of the calorimeter cell energies for cells with $R_{cell} < 0.7$:

$$E_{jet}^{meas} = \sum^{R_{cell}<0.7} E_{cell} \tag{1}$$

  The fraction of the energy of each cell deposited by a particle is weighted by the corresponding particle energy response.

- the *true* energy of the jet should have been equal to the sum of the calorimeter cell energies for cells that received energy from particles emitted within $R_{part} < 0.7$:

$$E_{jet}^{true} = \sum^{R_{part}<0.7} E_{cell} \tag{2}$$

  The cell energies are again weighted by the corresponding particle energy response.

- the *showering correction* is then equal to:

$$corr = E_{jet}^{true}/E_{jet}^{meas}. \tag{3}$$

The distances R_{cell} versus R_{part} (for selected $|\eta|$ bins) are shown in Figures 11, 12 and 13 for the following three cases, respectively:

1. $(R_{part} < 0.7)$ and $(R_{cell} < 0.7)$
2. $(R_{part} < 0.7)$ and $(R_{cell} > 0.7)$
3. $(R_{part} > 0.7)$ and $(R_{cell} < 0.7)$

All plots have been weighted by the cell energies.
As it is evident from Fig. 12, most of the jet energy deposited at large distances outside the jet cone has originated from the high energy particles at the very core of jet (within 0.1 from the jet centroid). On the other hand, most of the energy showered into the jet cone from particles outside, comes from particles *just* outside the cone that shower *just* inside, as shown in Fig. 13.

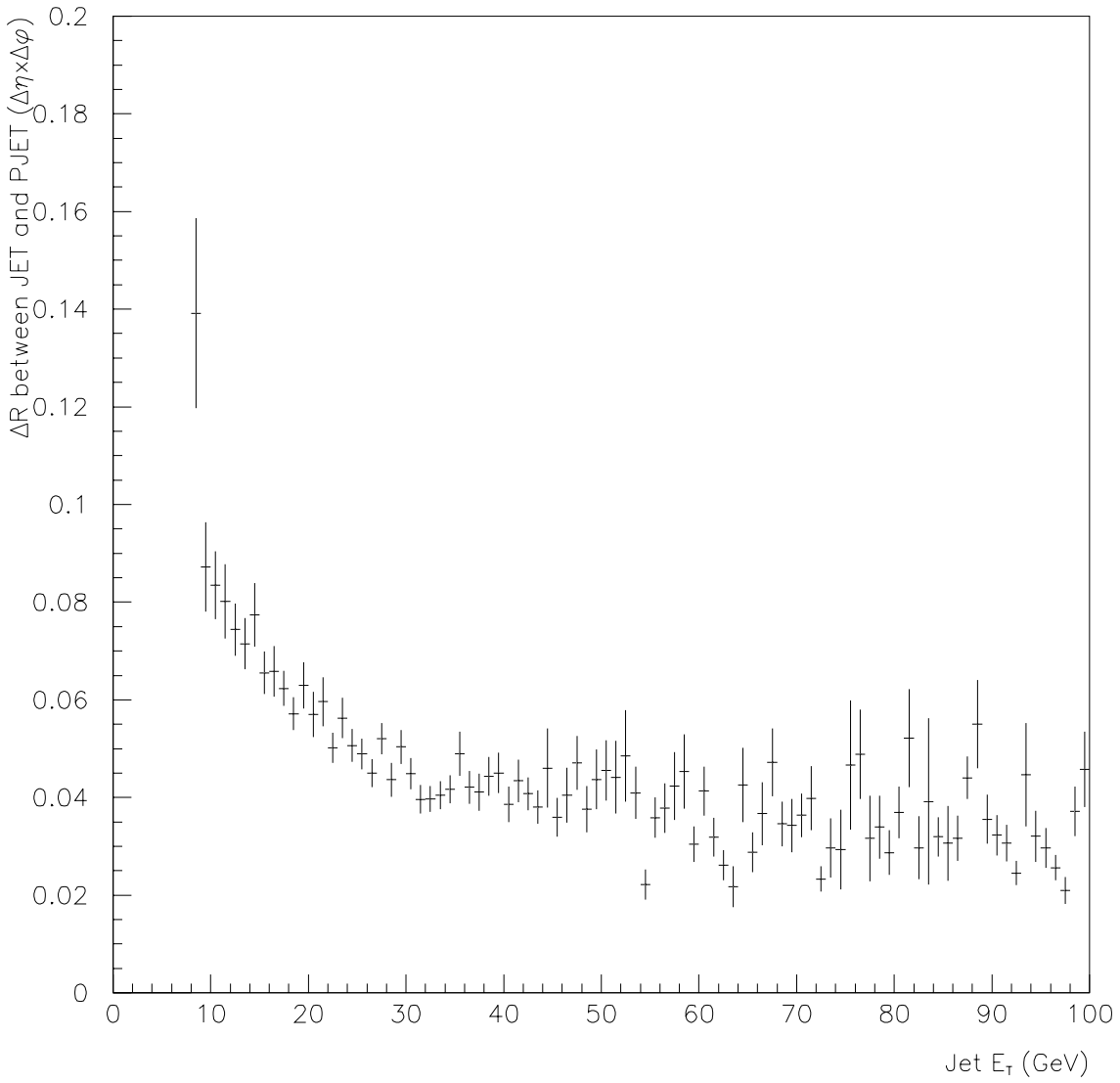

Figure 7: $\Delta R = \sqrt{\Delta\eta^2 + \Delta\phi^2}$ between the particle– and the closest calorimeter–level jets as a function of the calorimeter–level jet E_T.

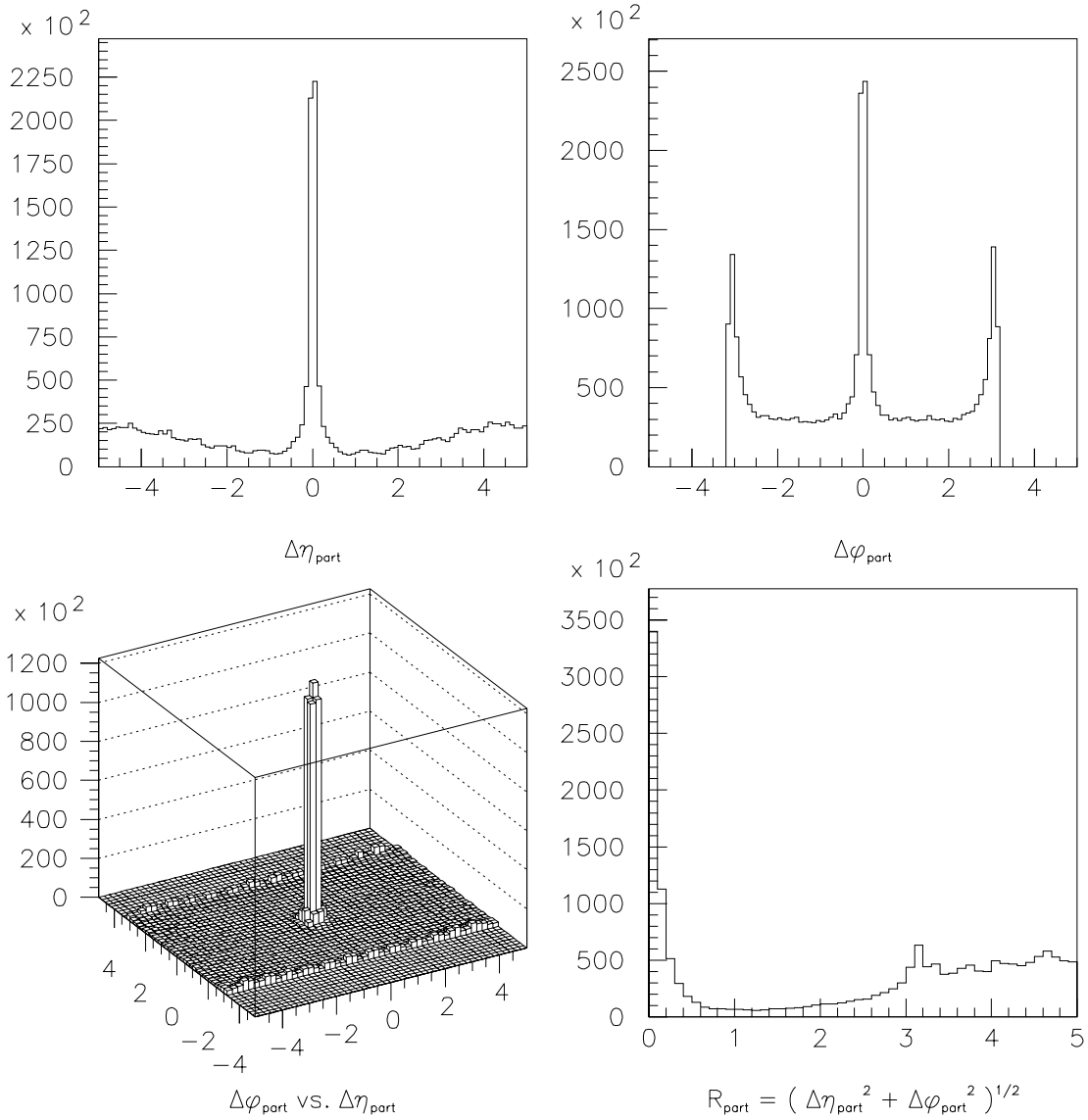

Figure 8: Distance in $\eta \times \phi$ space between a particle and a particle–level jet. All histograms have been weighted by the particle energy.

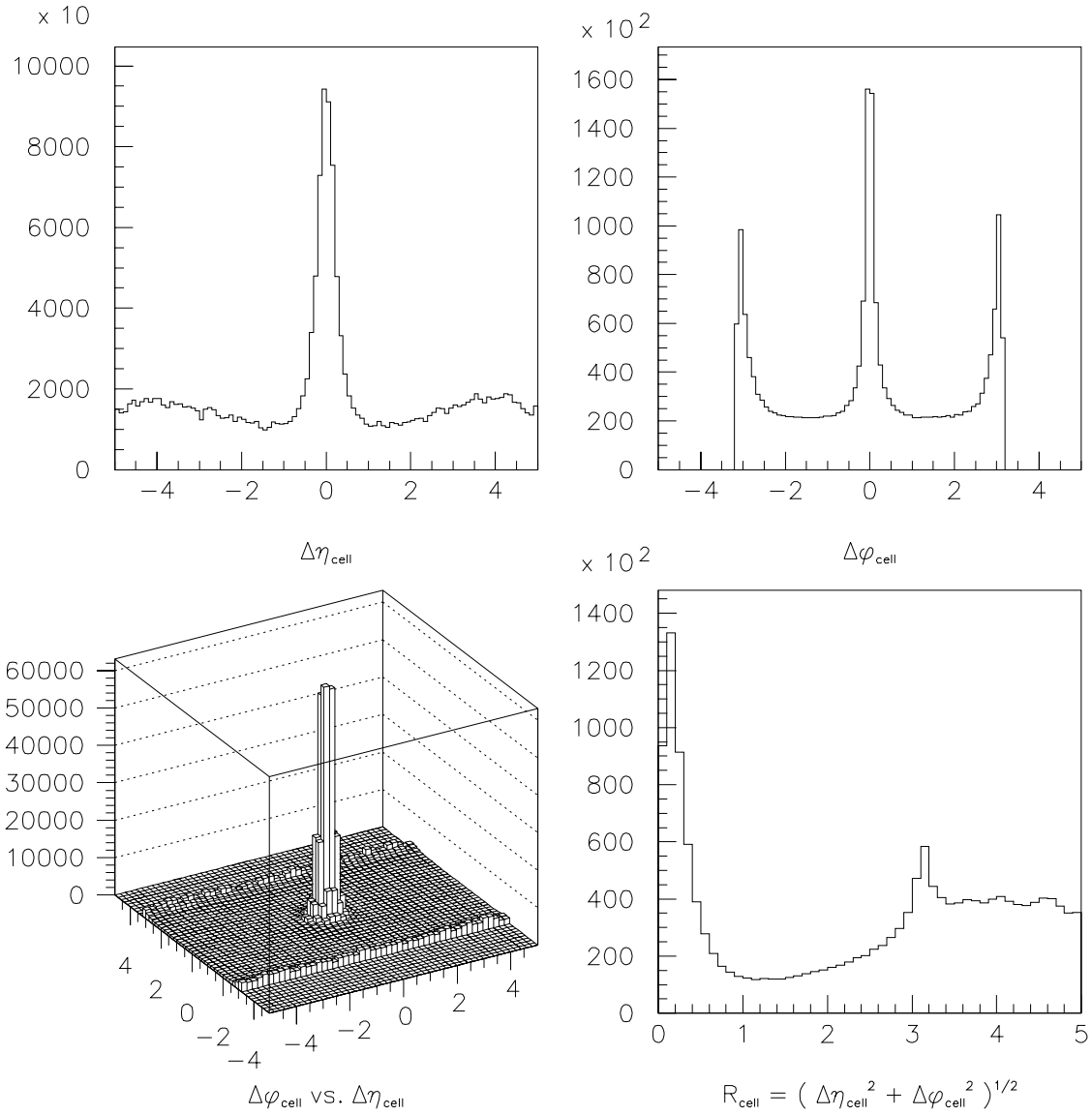

Figure 9: Distance in $\eta \times \phi$ space between a calorimeter cell and a calorimeter–level jet. All histograms have been weighted by the cell energy.

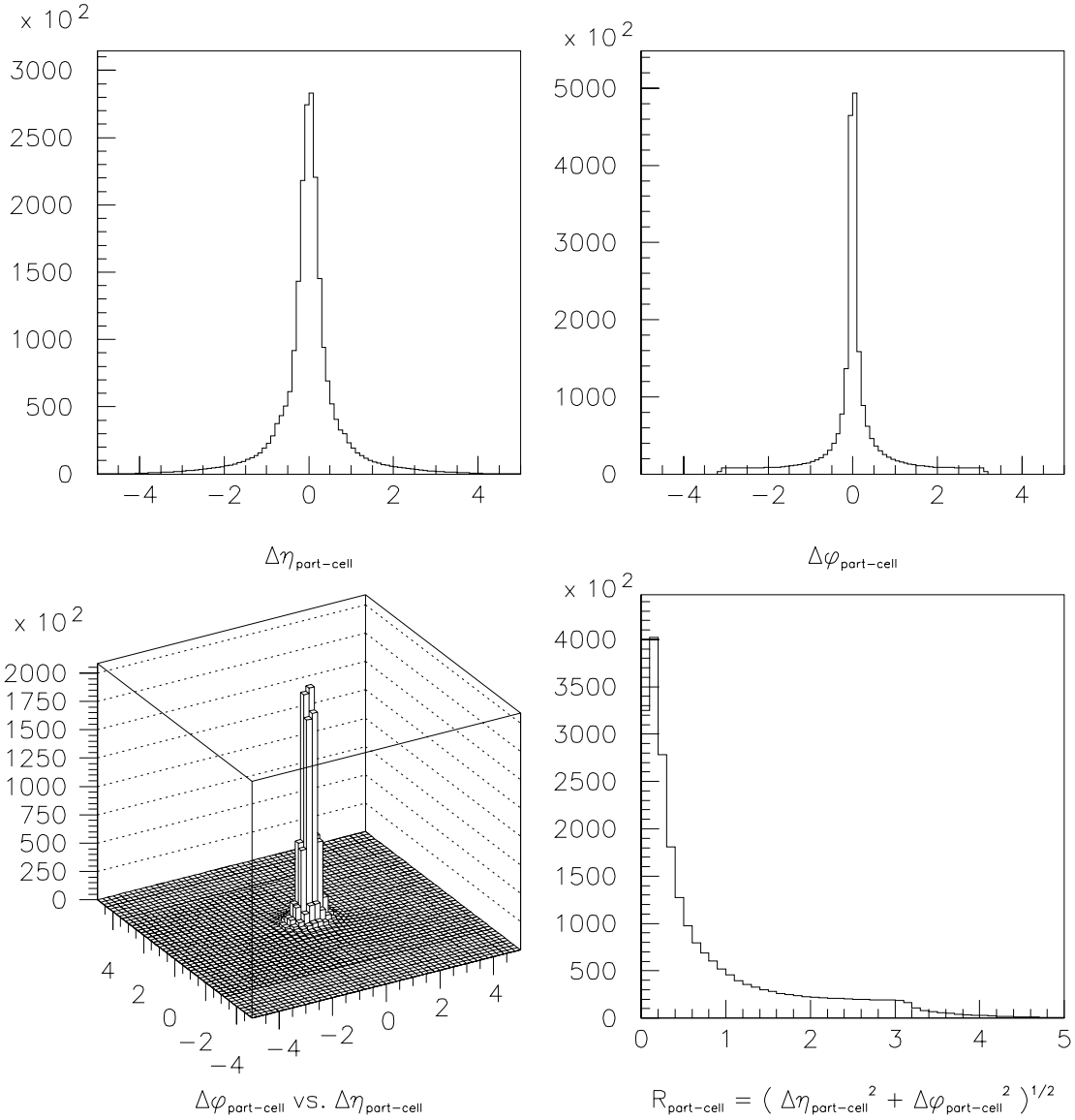

Figure 10: Distance in $\eta \times \phi$ space between a calorimeter cell and a calorimeter–level jet. All histograms have been weighted by the cell energy.

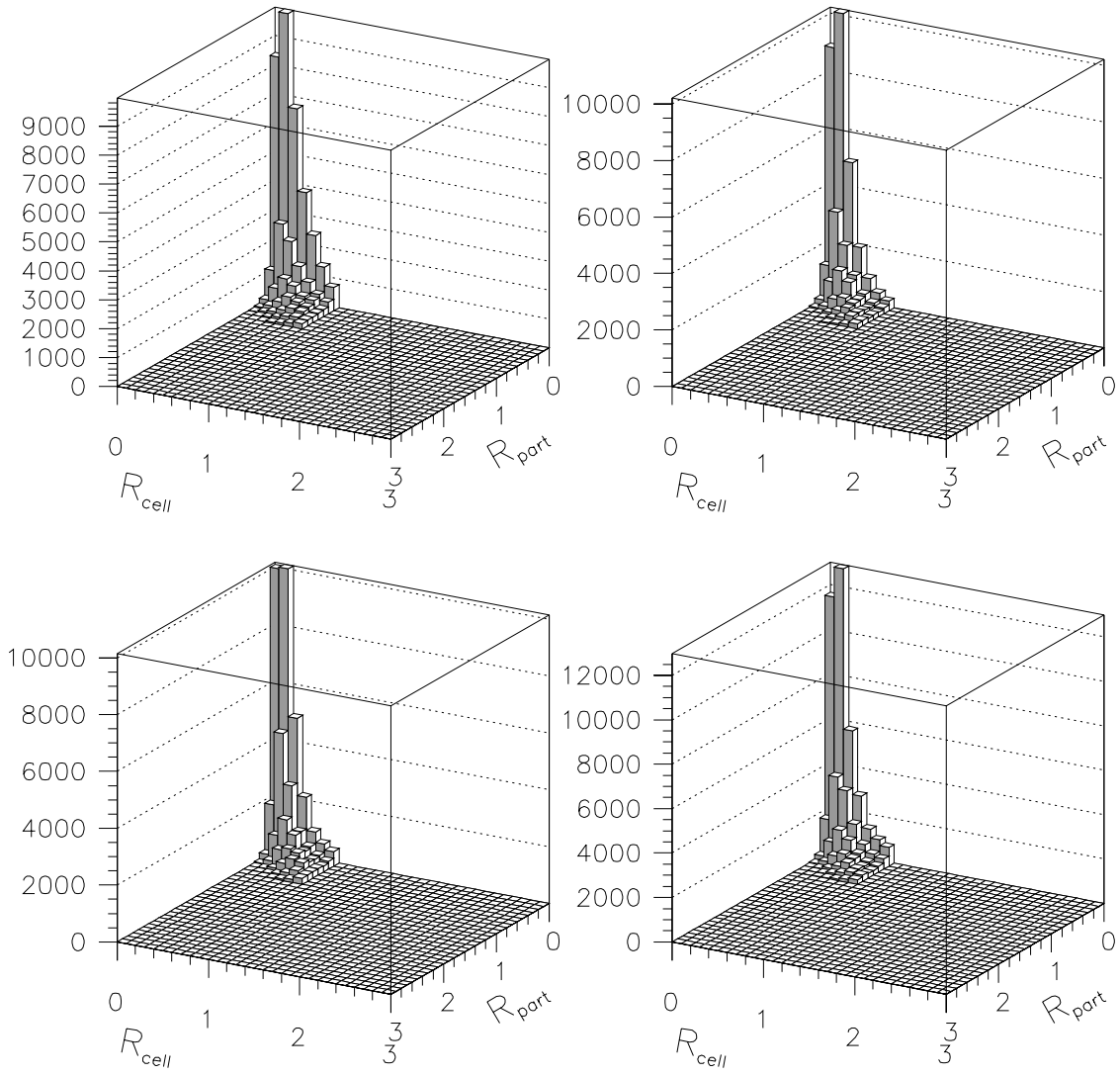

Figure 11: R_{cell} versus R_{part} for particles emitted and showering inside the 0.7 cone. The plots correspond to the following (absolute) pseudorapidity regions (from left to right and top to bottom): 0.0–0.4, 0.8–1.2, 1.6–2.0, 2.5–3.0 . All histograms have been weighted by the cell energy.

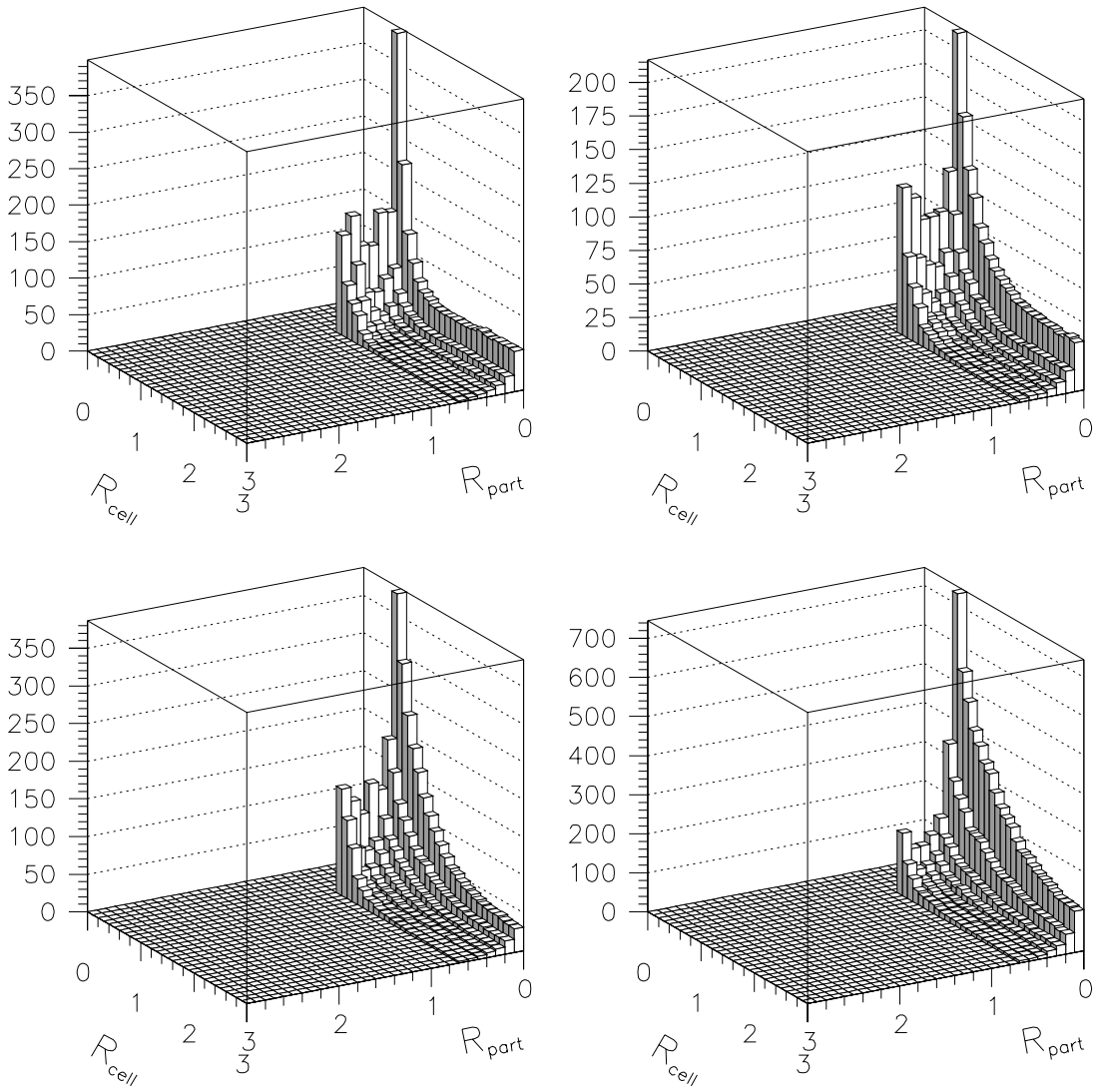

Figure 12: R_{cell} versus R_{part} for particles emitted inside the 0.7 cone but showering outside. The plots correspond to the following (absolute) pseudorapidity regions (from left to right and top to bottom): 0.0–0.4, 0.8–1.2, 1.6–2.0, 2.5–3.0 . All histograms have been weighted by the cell energy.

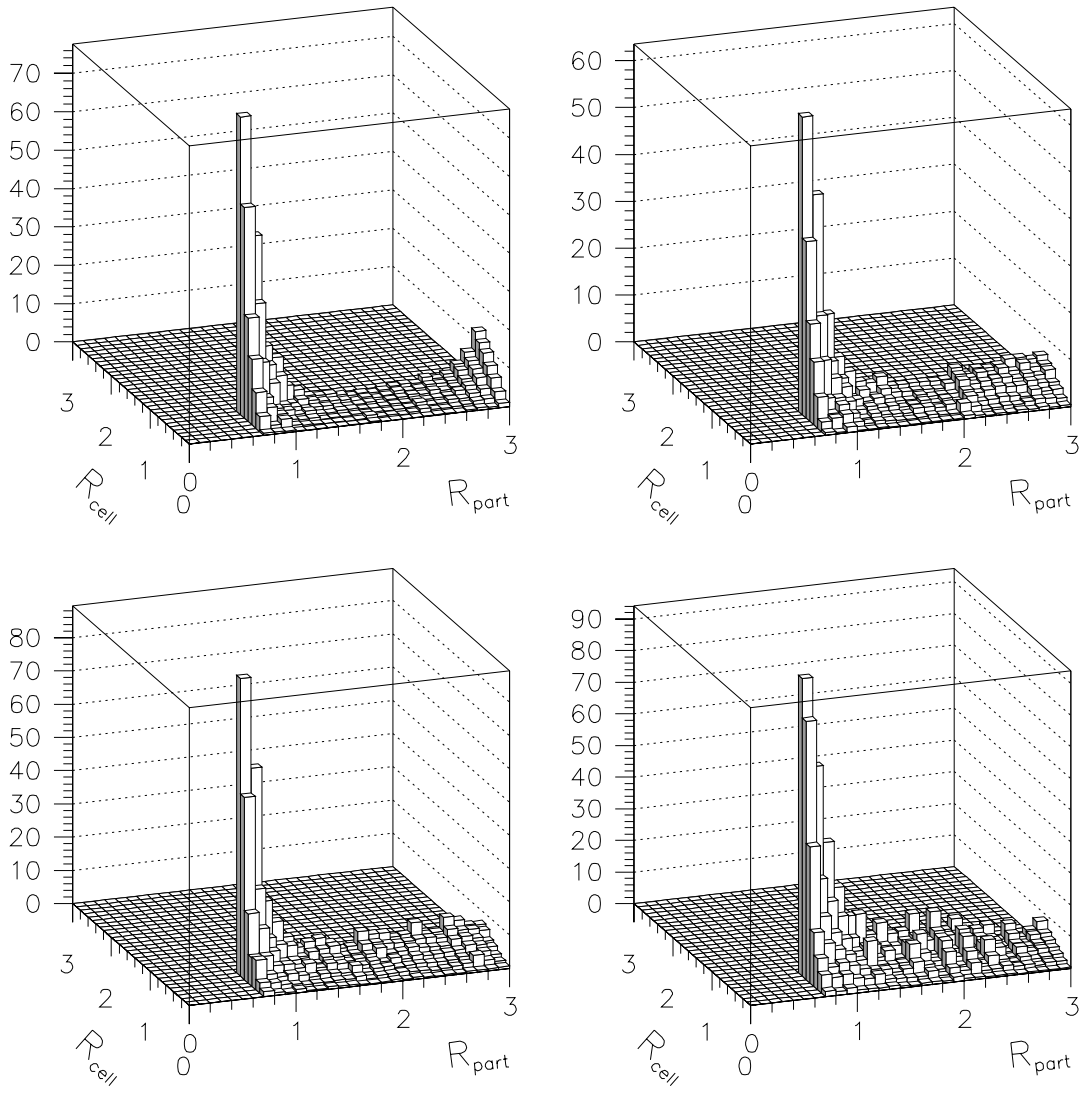

Figure 13: R_{cell} versus R_{part} for particles emitted outside the 0.7 cone that showered inside. The plots correspond to the following (absolute) pseudorapidity regions (from left to right and top to bottom): 0.0–0.4, 0.8–1.2, 1.6–2.0, 2.5–3.0 . All histograms have been weighted by the cell energy.

4.2 The Particle Energy Response

As explained in paragraph 4.1, we can measure the energy response in the calorimeter of each individual particle by comparing its energy to the sum of the energy deposits in the calorimeter cells that originated from that particle. The inverse of the particle energy response, i.e. the response correction used as a weight when summing the cell energies, is shown in Fig. 14.

As a closure test of the particle energy response correction, we sum the energies of all calorimeter cells in the event, each one of them weighted by the response correction corresponding to the particle(s) that deposited energy in that cell. This sum is exactly equal to the sum of the energies of all particles of the event, as can be seen in Fig. 15.

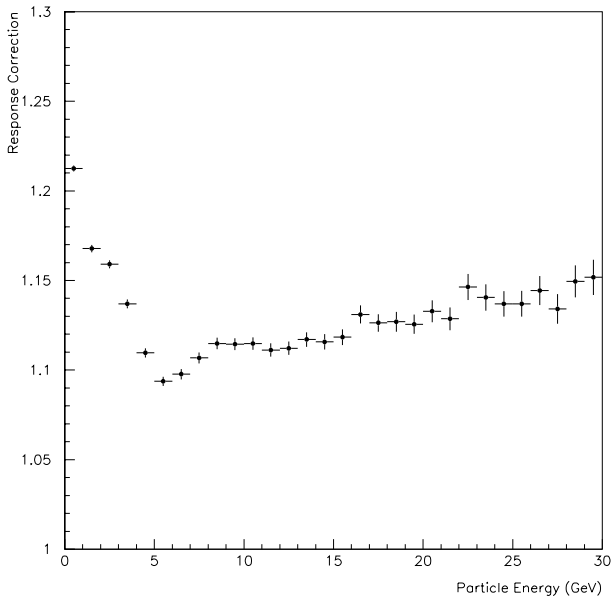

Figure 14: The particle energy response correction, for all particles of the event.

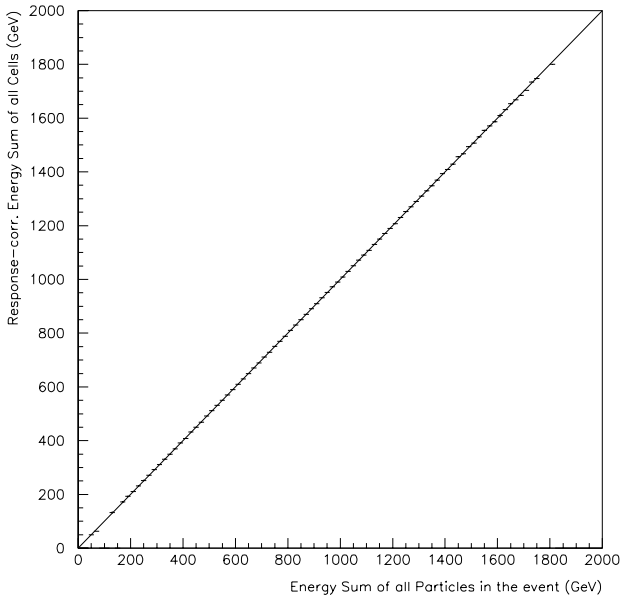

Figure 15: Closure test of the particle energy response correction.

4.3 MPF Bias and the Jet Limit

The true showering correction is given by Eq. (3). We need to consider, however, that the showering correction is applied to the data after the jet energy has been corrected for response using the Missing E_T Projection Fraction (MPF) method [2].

In the MPF method, we consider photon–jet events, with the two objects back–to–back in azimuth, and with the photon energy already corrected for losses in the electromagnetic calorimeter. The E_T of all cells in the calorimeter is then projected on the direction of the photon. Any $\not\!\!E_T$ in the direction of the jet is assumed to be due to the imperfect response of the hadronic calorimeter. It can easily be shown that the latter is equal to:

$$R_{had} \equiv 1 + MPF = 1 + \frac{\vec{\not\!\!E}_T \cdot \hat{n}_T^\gamma}{E_T^\gamma}, \tag{4}$$

where $\vec{\not\!\!E}_T$ is the missing transerse energy of the event as measured in the calorimeter, E_T^γ and $\hat{n}_T^\gamma$ are the transverse energy and the direction of the photon, respectively, and MPF is the fraction of the missing transverse energy in the direction of the photon.

The assumption that $\vec{\not\!\!E}_T \cdot \hat{n}_T^\gamma$ is due only (or mostly) to the hadronic response, would be true only if the energy opposite of the photon were deposited very close to the direction of the jet (which, in first order, is the same with the direction of the photon) in the transverse plane. In reality, however, the showering of the particles in the calorimeter creates additional $\not\!\!E_T$ on the photon direction. This is explained in the following. Consider an event with only one particle and one photon, with the two objects back–to–back in azimuth, i.e. balanced in E_T at the particle level. If it were possible to measure the particle energy in the calorimeter as a point–like object, the difference between the E_T of the particle and the E_T of the photon would be due only to the hadronic response of the calorimeter. Due to the showering effect, however, what we really measure is the total particle energy inside a finite volume $(\Delta r, \Delta\theta, \Delta\phi)$. This translates into E_T as follows: the part of the particle energy which is measured at zero angles from the photon/particle axis contributes to $\vec{\not\!\!E}_T \cdot \hat{n}_T^\gamma$ because of its hadronic response; the part of the particle energy measured at some angle from the photon/particle axis contributes to $\vec{\not\!\!E}_T \cdot \hat{n}_T^\gamma$ because of its hadronic response *and* because of the difference between its scalar E_T and its E_T–projection on the photon–E_T axis. Therefore, the MPF method will correct the jet energy *not only* for pure calorimeter response, *but also* for the fraction of the hadronic transverse energy that is emitted orthogonal to the jet axis. In other words, the MPF bias already corrects for part of the showering effect.

One way to constrain the bias of the MPF method and avoid over–correcting the jet energy is to consider as true energy of the jet the energy that originated from particles emitted within $R_{part} < 0.7$ *and* was deposited in cells within $R_{cell} < jet\ limit$:

$$E_{jet}^{true\,\prime} = \sum^{(R_{part}<0.7)\ \&\ (R_{cell}<jet\ limit)} E_{cell} \tag{5}$$

The reason is simple: the farther away from the jet axis a cell is, the smaller its E_T–projection on the jet axis will be, which results in larger $\not\!\!E_T$ and smaller response (as measured by MPF). Thus, the farther away from the jet axis, the more of the energy loss due to showering is already corrected by the MPF bias.

In order to decide on the jet limit in each pseudorapidity region, we look at the calorimeter–level jet energy density profiles in the Monte Carlo, measured using the cell information in the GCAH banks after energy response correction. These are shown in Fig. 16, binned in terms of jet pseudorapidity and energy. The jet limit for the different η-bins is shown in Table 4. In each region, the jet limit we choose is smaller or equal to the jet limit used in the comparison between data and Monte Carlo energy density profiles (see section 3).

Jet Limit in Showering Correction					
	jet-η range	jet limit		jet-η range	jet limit
1	0.0 – 0.4	1.0	5	1.6 – 2.0	1.3
2	0.4 – 0.8	1.1	6	2.0 – 2.5	1.5
3	0.8 – 1.2	1.2	7	2.5 – 3.0	1.5
4	1.2 – 1.6	1.2	8	3.0 – 3.5	1.6

Table 4: Distance in $\eta \times \phi$ space from the jet centroid where the jet finishes, for calorimeter–level jets of various pseudorapidities.

To test the qualitative arguement on the MPF–bias compensation by the jet limit, we mimic the MPF method on a cell–by–cell basis, and then calculate the *residual* showering correction: in calculating the measured and true energy of the jet according to equations (1) and (2) (i.e. no jet limit), we scale the energy of each cell by the cell E_T projection fraction. The latter is equivalent to the cell response as measured by the MPF method.

$$E^{meas}_{jet,\,after\,MPF} = \sum^{R_{cell}<0.7} E_{cell} \cdot \frac{E^{cell}_{T\,proj}}{E^{cell}_{T}} \tag{6}$$

$$E^{true}_{jet,\,after\,MPF} = \sum^{R_{part}<0.7} E_{cell} \cdot \frac{E^{cell}_{T\,proj}}{E^{cell}_{T}} \tag{7}$$

where

$$E^{cell}_{T\,proj} = \frac{E^{cell}_{x} \cdot E^{jet}_{x} + E^{cell}_{y} \cdot E^{jet}_{y}}{E^{jet}_{T}} \tag{8}$$

The residual showering correction is then:

$$corr_{after\,MPF} = E^{true}_{jet,\,after\,MPF} / E^{meas}_{jet,\,after\,MPF}. \tag{9}$$

The results are shown in Fig. 17. The showering correction is plotted in the eight pseudorapidity bins versus jet energy for three cases:

1. the true ("raw") correction from the Monte Carlo, as given by Eq.(3) (open crosses),
2. the showering correction when the particles are followed outside the jet up to the "jet limit" (full circles),

3. the residual showering correction, after the jet energy has been corrected by the MPF method (open stars).

Two interesting conclusions can be drawn from the plots:

- the MPF bias absorbs a large part of the "raw" showering correction;
- the jet limit compensates for the MPF bias in a very successful way.

Therefore, we use the jet limit in order to constrain the effect of the MPF bias when calculating the showering correction.

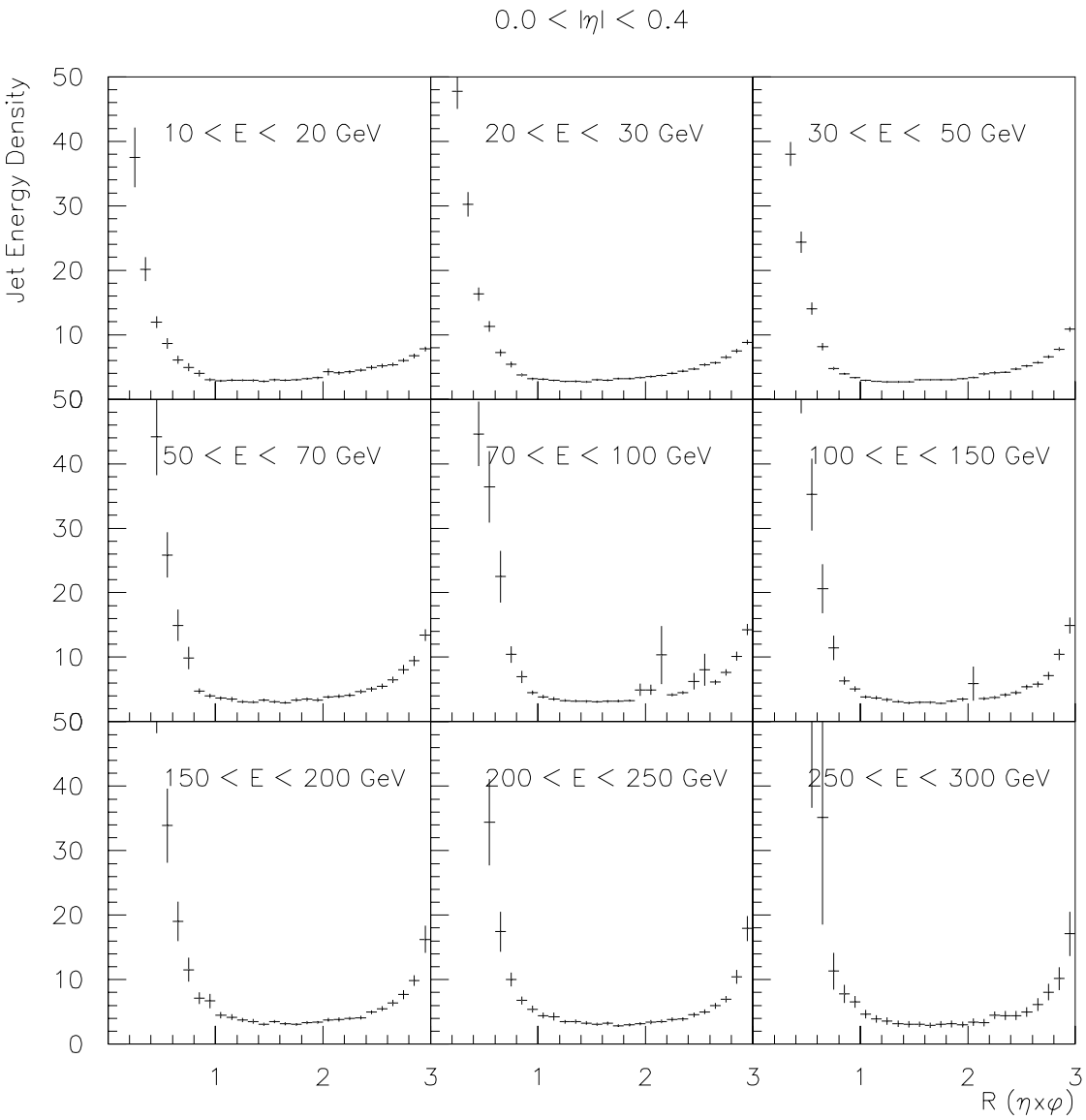

Figure 16: Energy density profiles for calorimeter–level jets in the Monte Carlo sample, as derived from the GCAH banks. The energy in each calorimeter cell has been corrected for response.

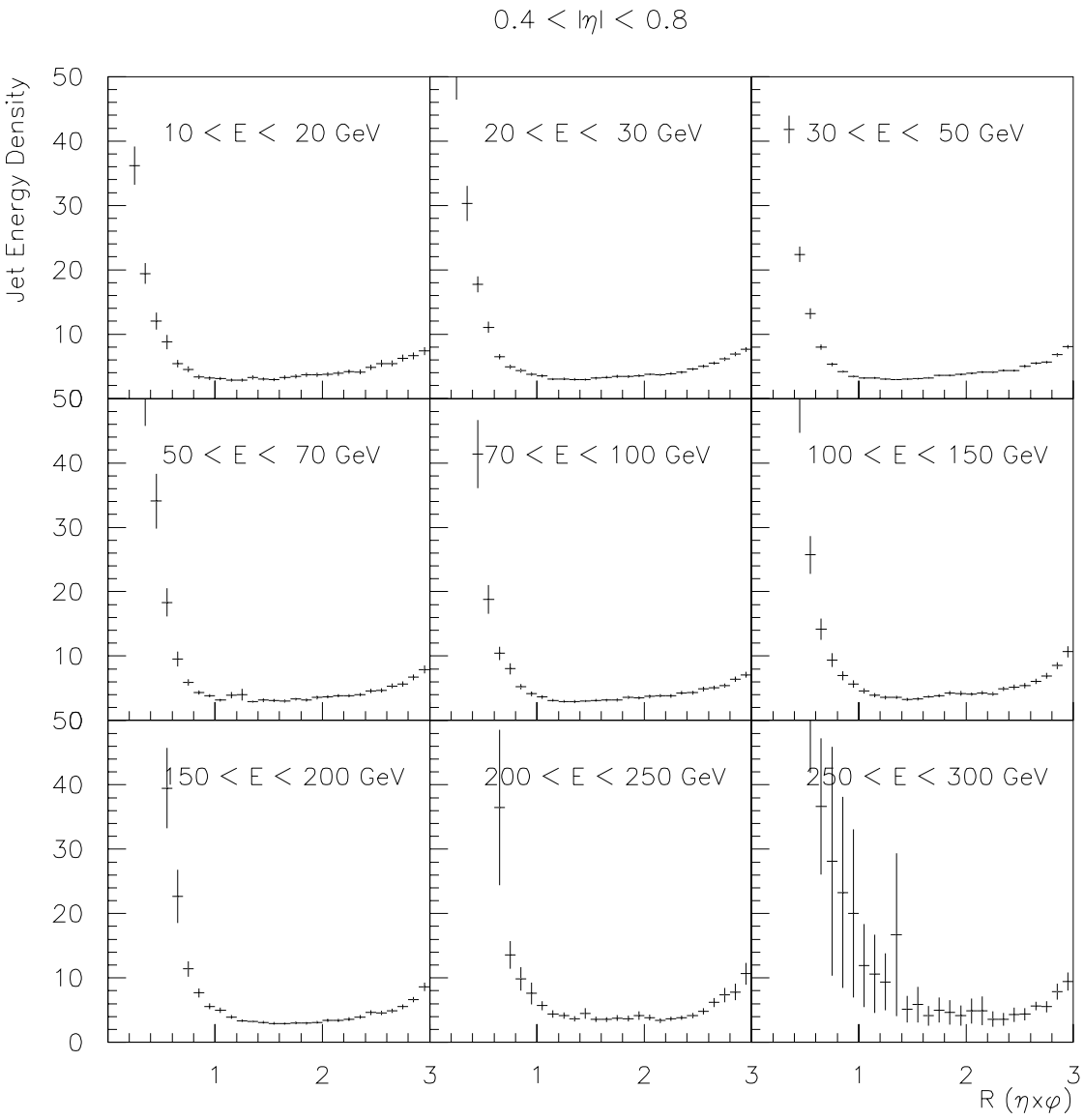

Figure 16: Energy density profiles for calorimeter–level jets in the Monte Carlo sample, as derived from the GCAH banks. The energy in each calorimeter cell has been corrected for response.

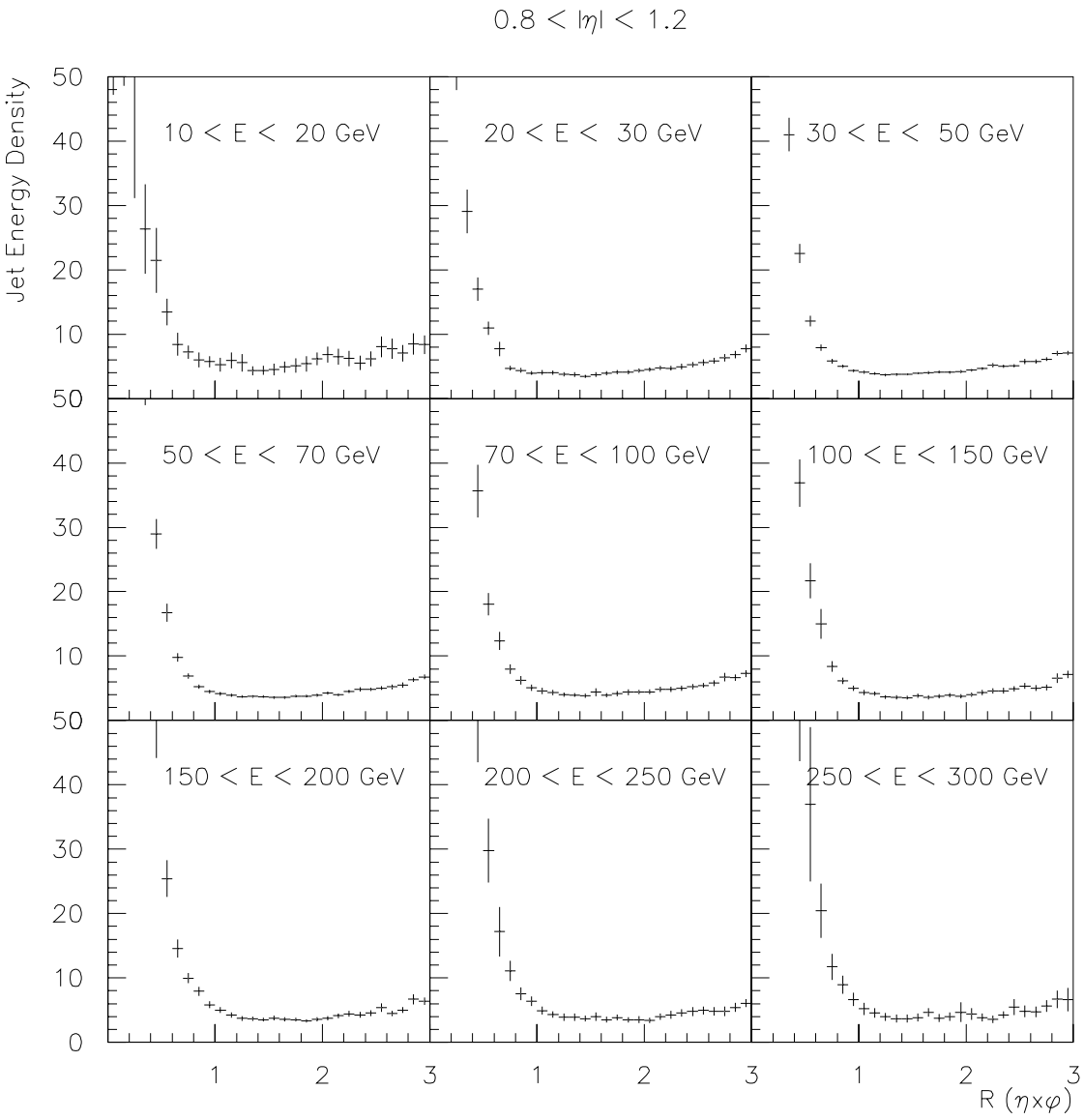

Figure 16: Energy density profiles for calorimeter–level jets in the Monte Carlo sample, as derived from the GCAH banks. The energy in each calorimeter cell has been corrected for response.

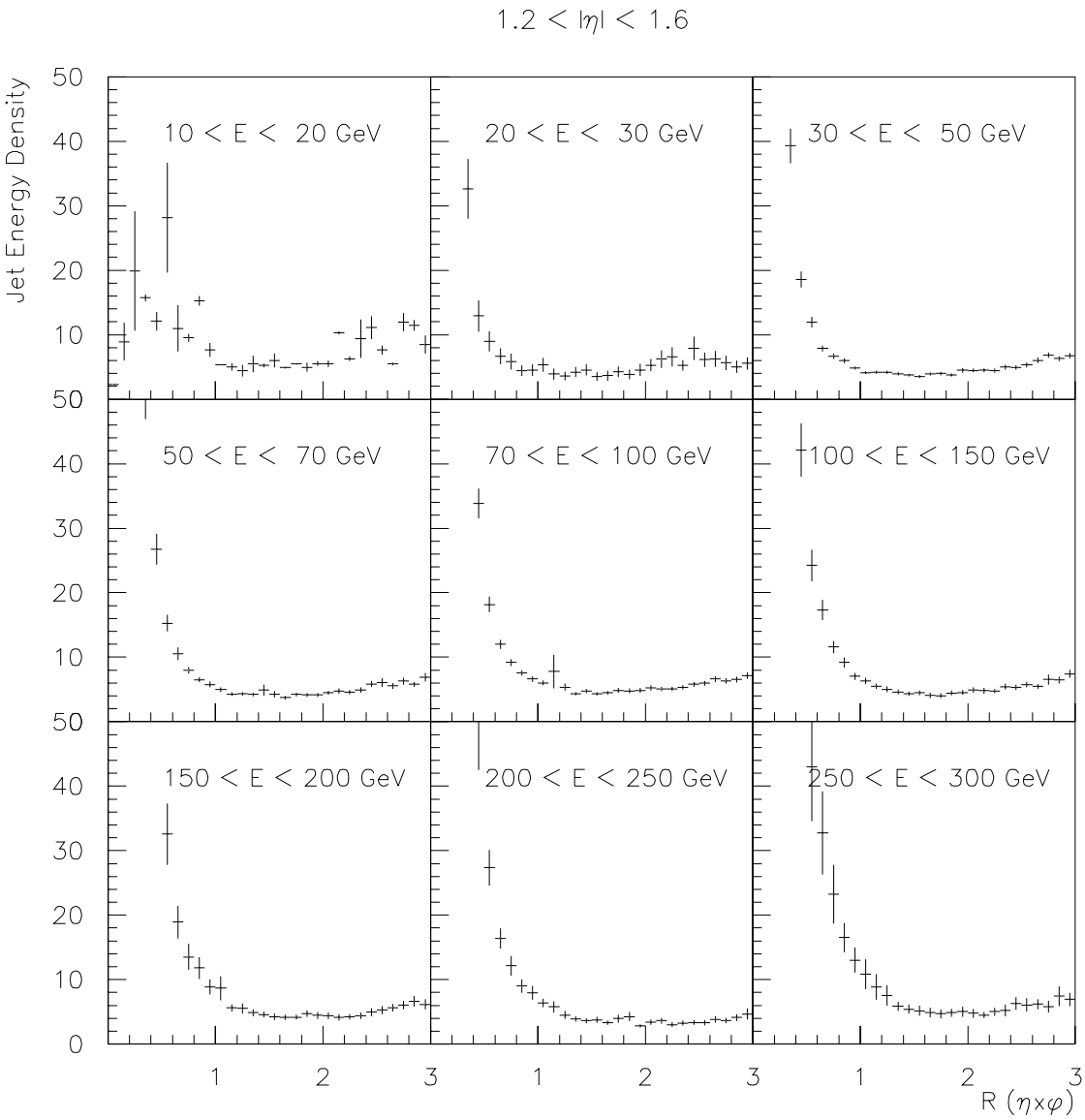

Figure 16: Energy density profiles for calorimeter–level jets in the Monte Carlo sample, as derived from the GCAH banks. The energy in each calorimeter cell has been corrected for response.

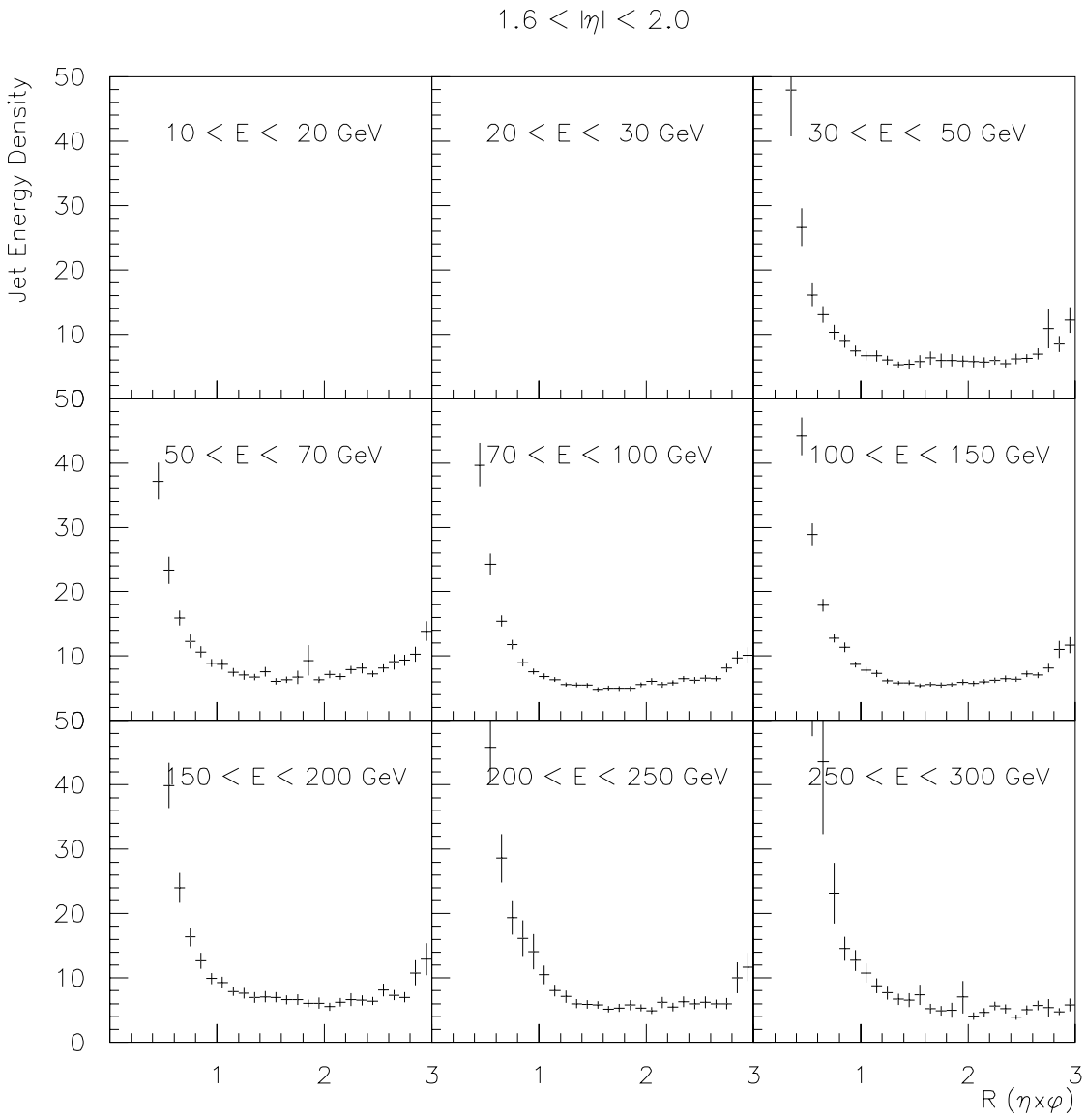

Figure 16: Energy density profiles for calorimeter–level jets in the Monte Carlo sample, as derived from the GCAH banks. The energy in each calorimeter cell has been corrected for response.

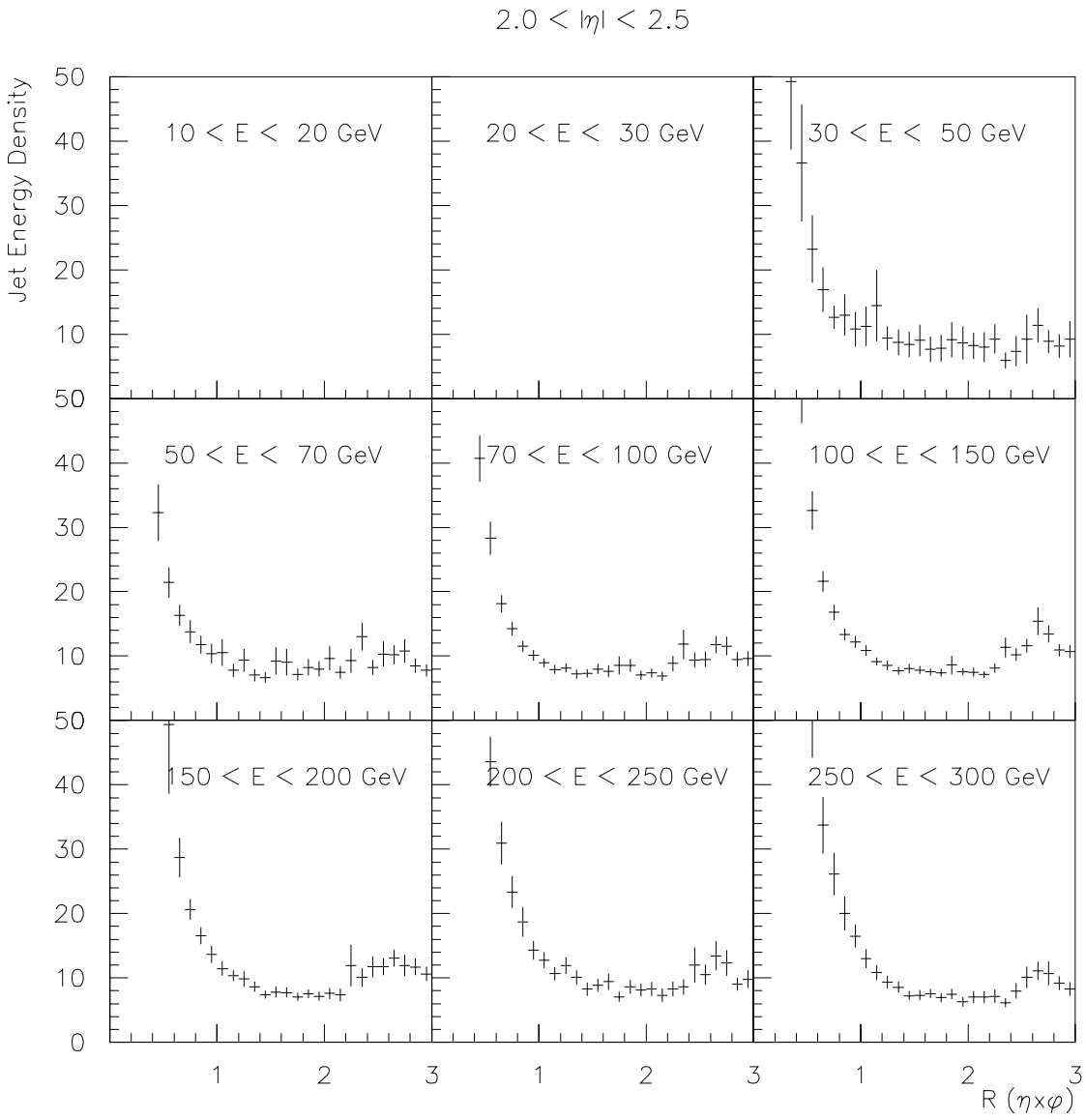

Figure 16: Energy density profiles for calorimeter–level jets in the Monte Carlo sample, as derived from the GCAH banks. The energy in each calorimeter cell has been corrected for response.

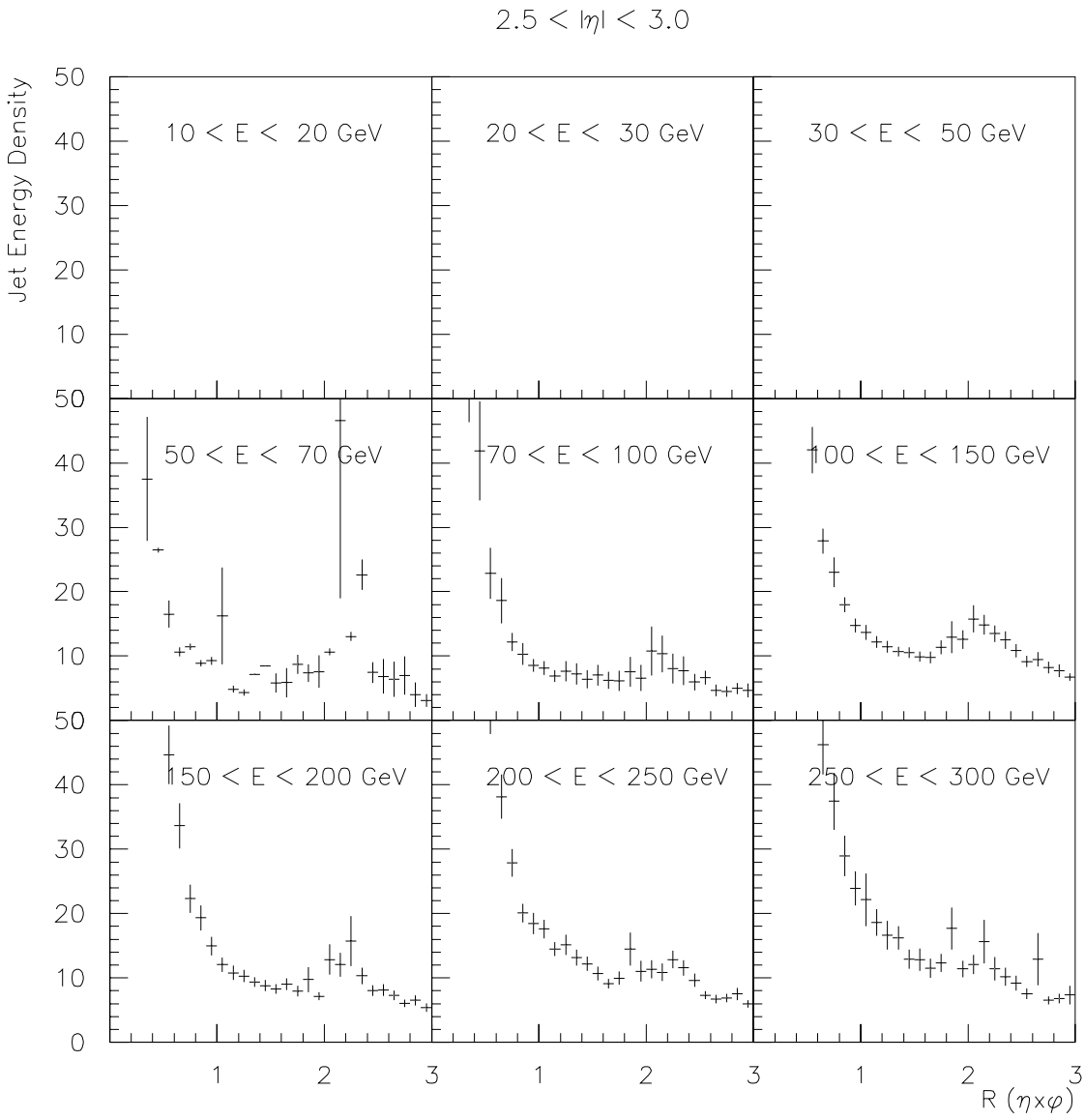

Figure 16: Energy density profiles for calorimeter–level jets in the Monte Carlo sample, as derived from the GCAH banks. The energy in each calorimeter cell has been corrected for response.

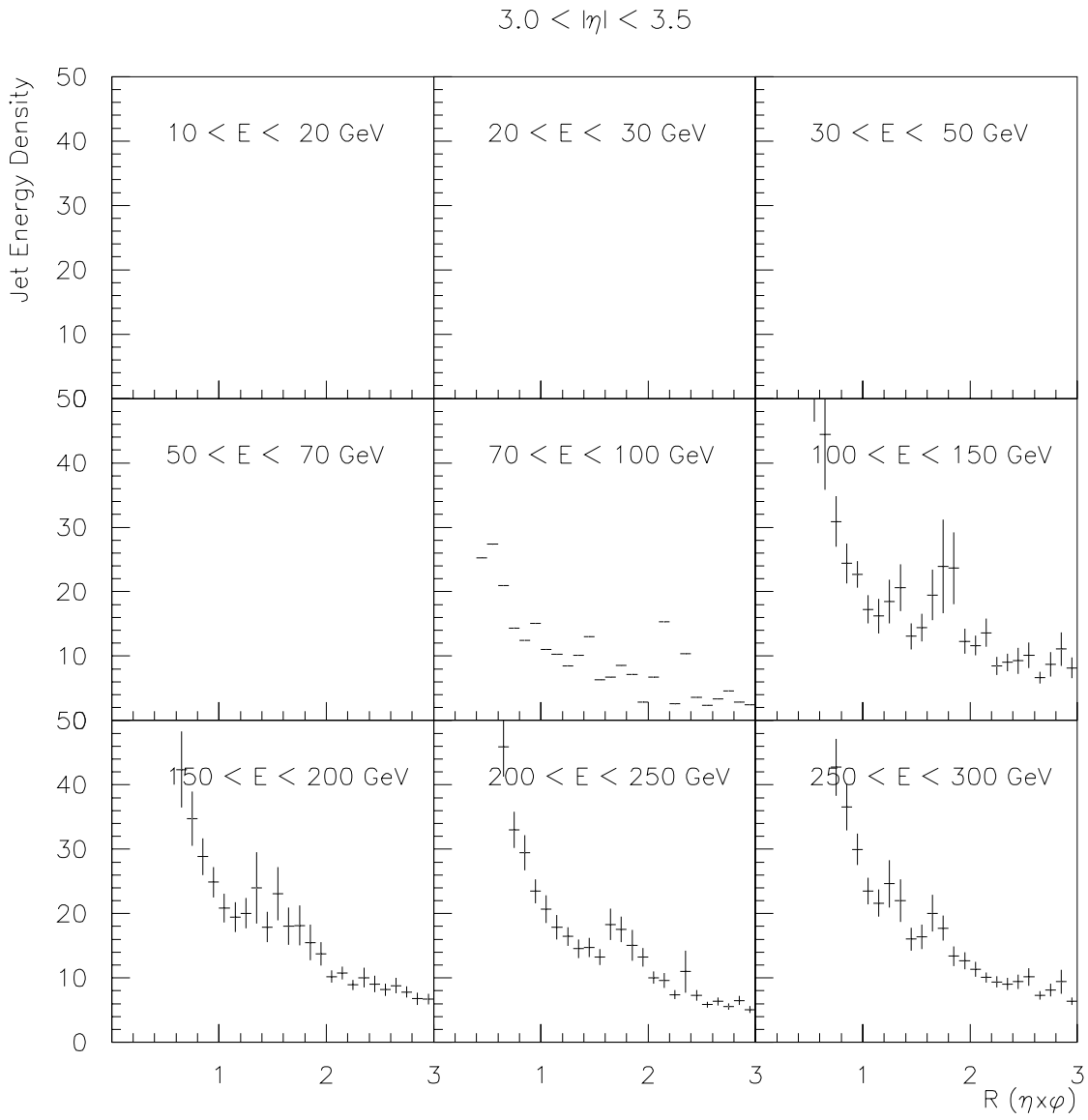

Figure 16: Energy density profiles for calorimeter–level jets in the Monte Carlo sample, as derived from the GCAH banks. The energy in each calorimeter cell has been corrected for response.

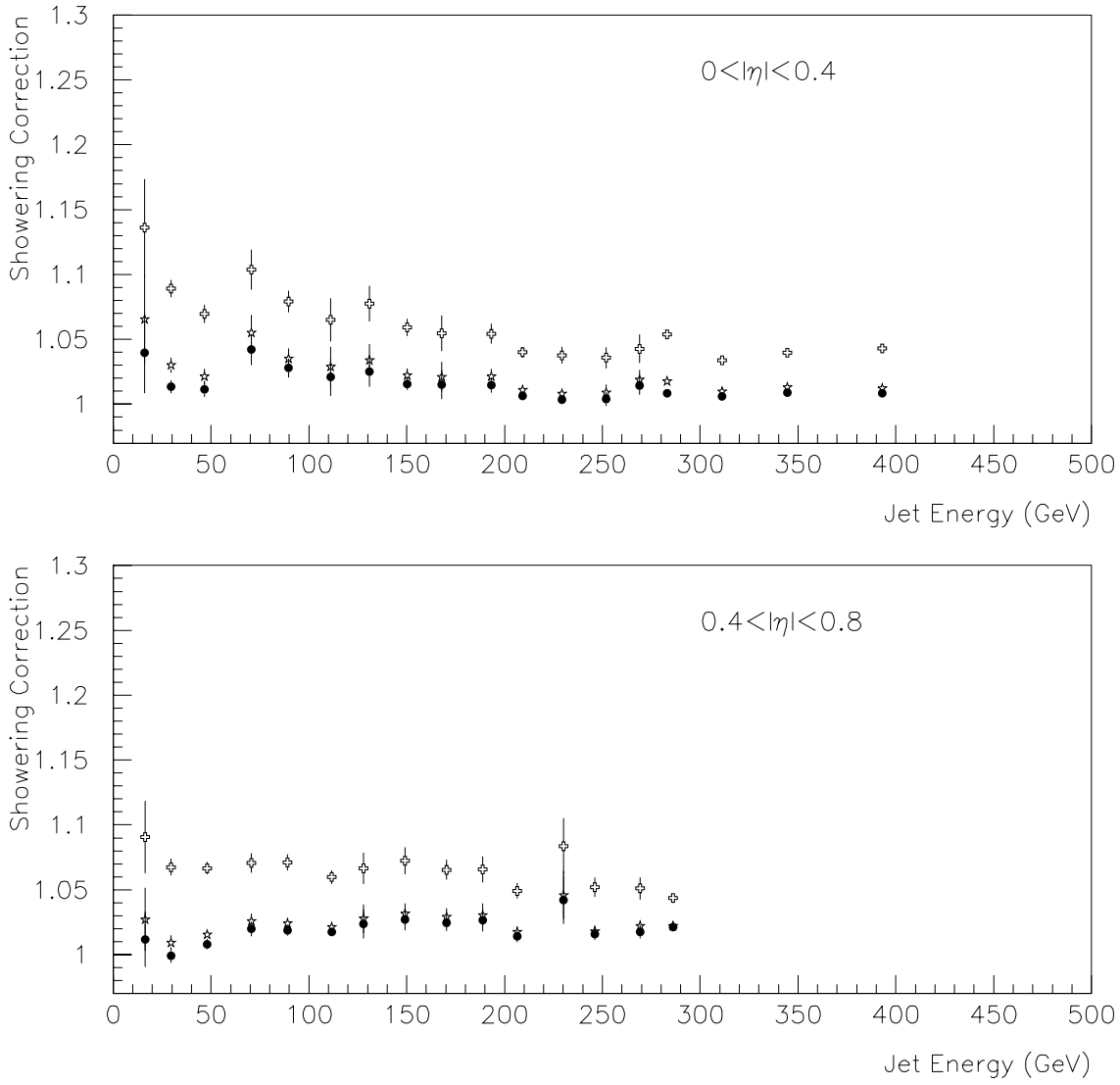

Figure 17: The showering correction in terms of response–corrected jet energy: without jet limit (open crosses), with jet limit (full circles), without jet limit but after MPF–bias (open stars).

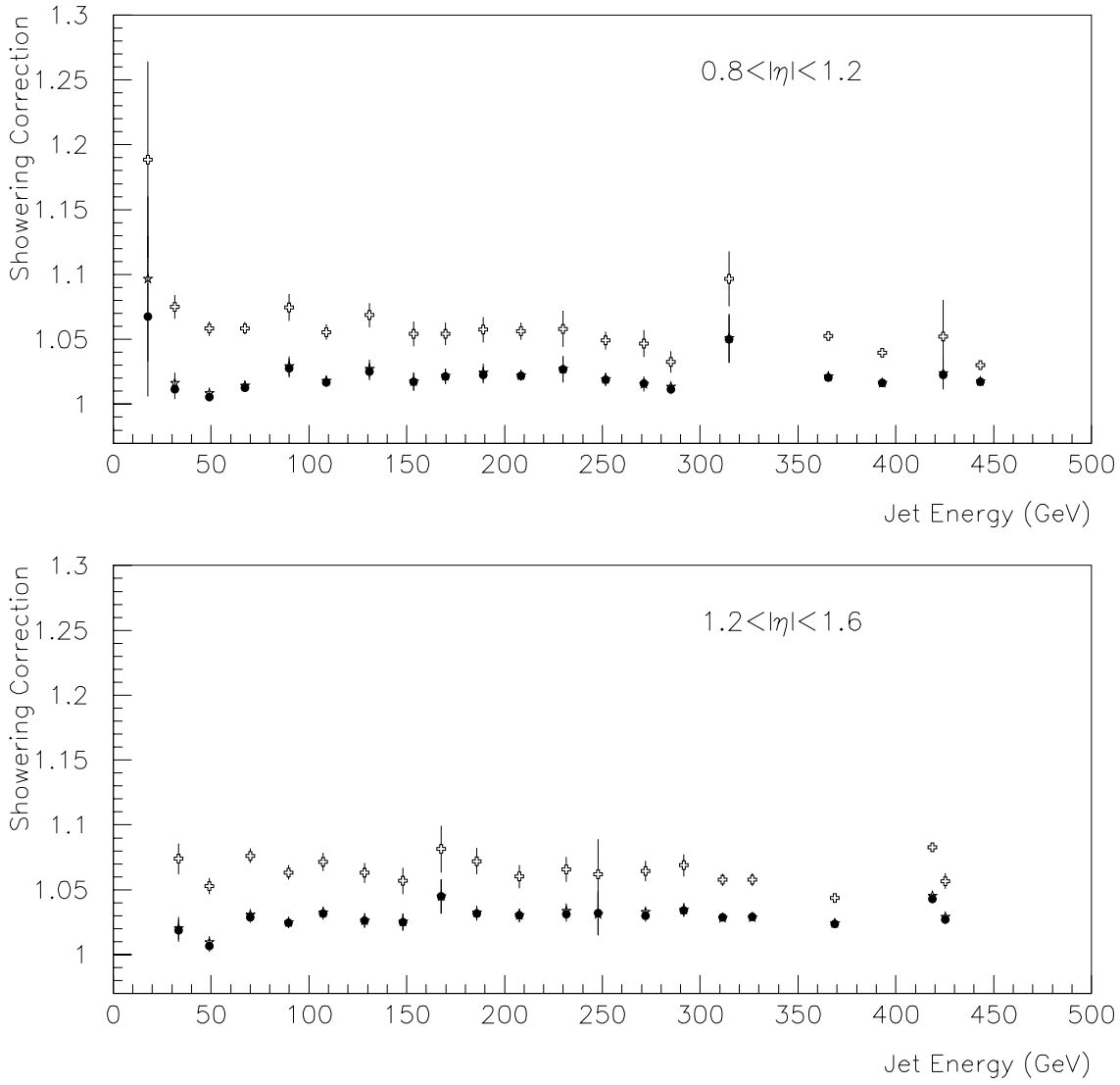

Figure 17: The showering correction in terms of response–corrected jet energy: without jet limit (open crosses), with jet limit (full circles), without jet limit but after MPF–bias (open stars).

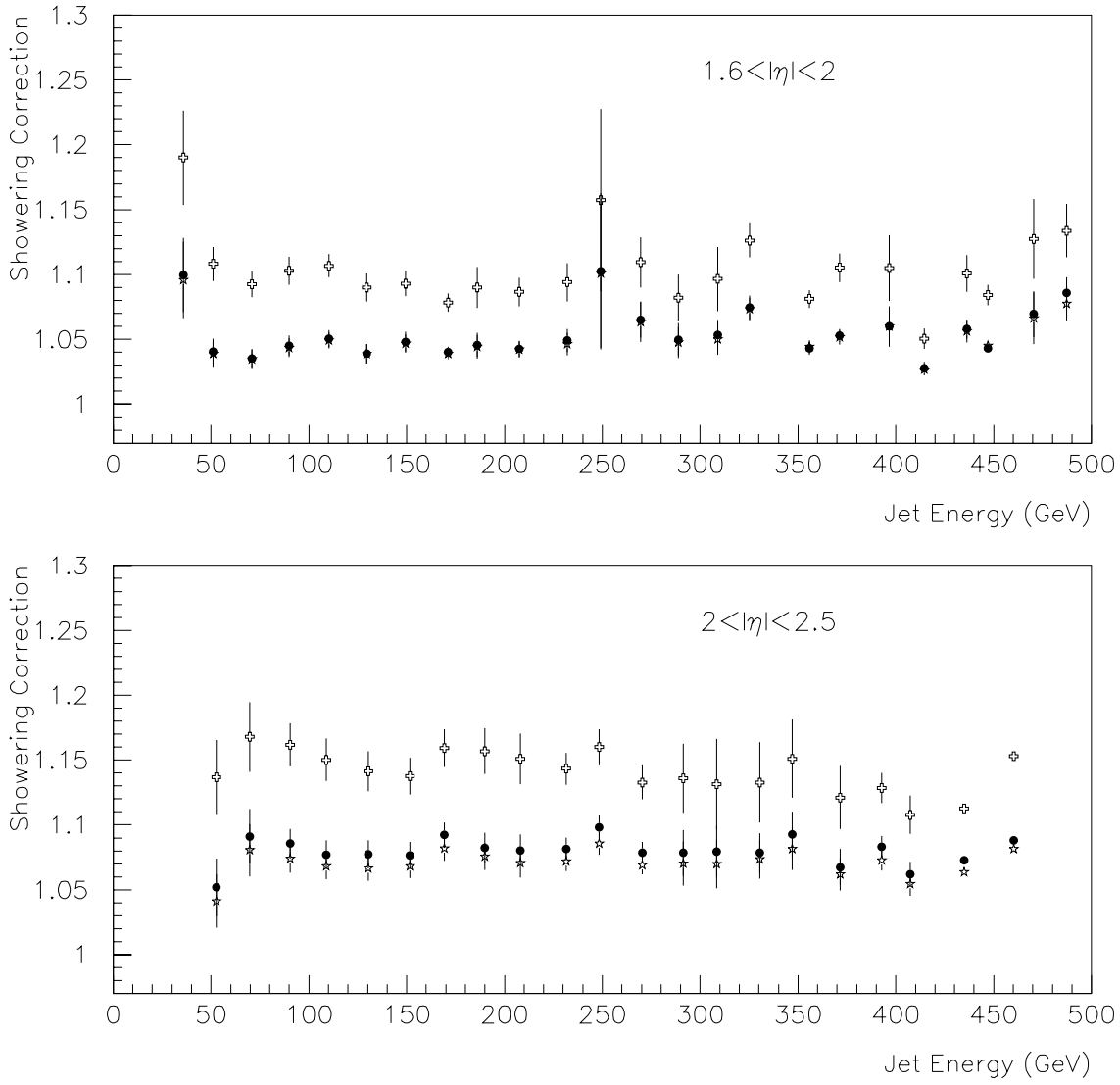

Figure 17: The showering correction in terms of response–corrected jet energy: without jet limit (open crosses), with jet limit (full circles), without jet limit but after MPF–bias (open stars).

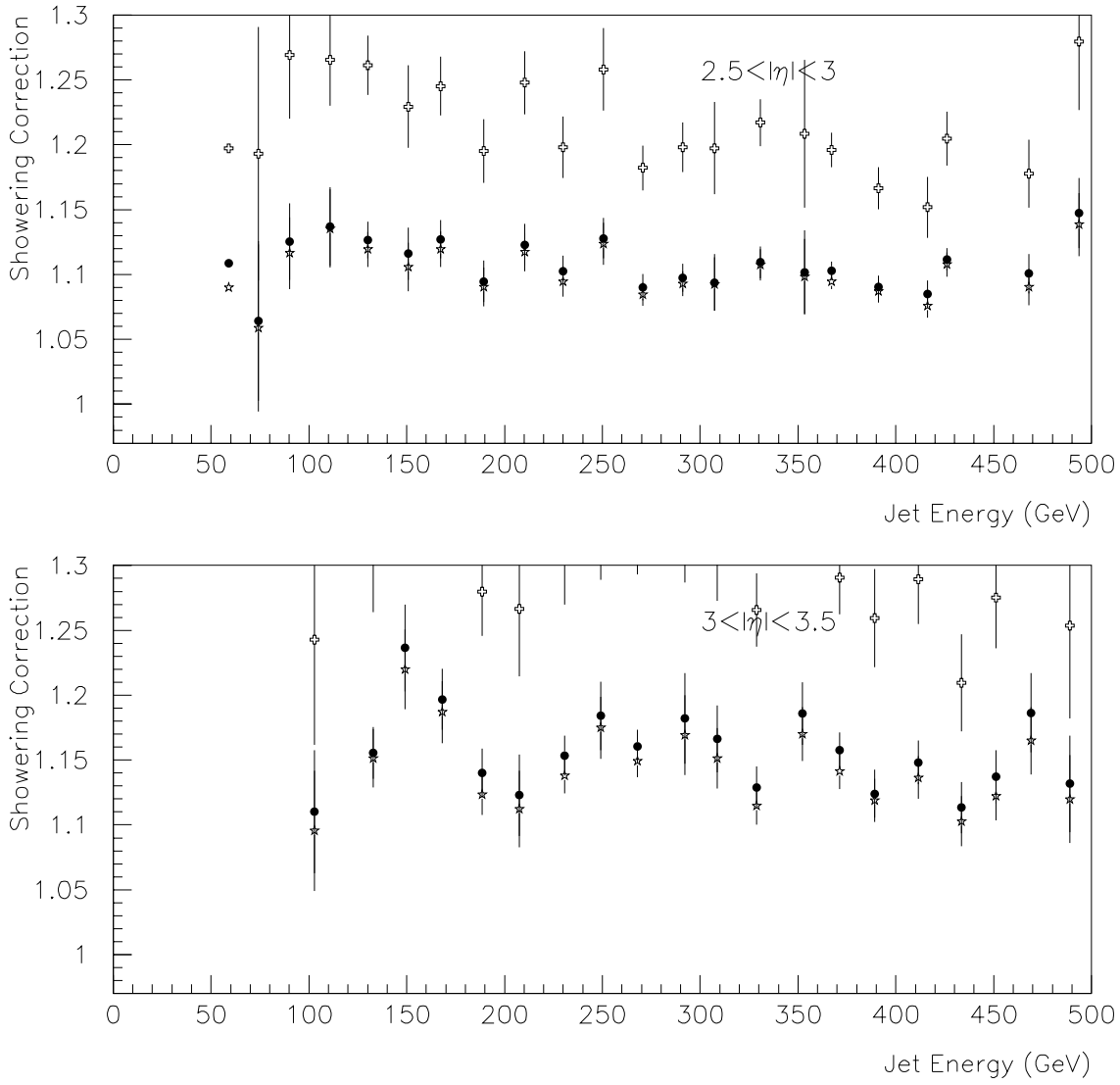

Figure 17: The showering correction in terms of response–corrected jet energy: without jet limit (open crosses), with jet limit (full circles), without jet limit but after MPF–bias (open stars).

4.4 Results on the Showering Correction

The showering correction is presented in terms of calorimeter–level response–corrected jet energy, for jets in eight pseudorapidity bins (from zero to 3.5 units in pseudorapidity), in Fig. 18. In the first six η-bins ($0.0 < |\eta| < 2.5$) the correction shows no significant dependence on the jet energy (any energy dependence of the "raw" correction is absorbed by the MPF bias), and is therefore fitted with a flat line:

$$corr = a \tag{10}$$

In the last two η-bins ($2.5 < |\eta| < 3.5$) a soft dependence on the jet energy is exhibited; in those bins, the correction is fitted with the functional form:

$$corr = a/E^{jet} + b \tag{11}$$

The fitting parameters and their uncertainties are given in Table 5. The error on the correction due to the uncertainties on the fitting parameters is calculated using standard error propagation:

$$fitting\ \ error = \sqrt{(\frac{1}{E} \cdot \Delta a)^2 + (\Delta b)^2 + 2 \cdot \frac{1}{E} \cdot covariance^2} \quad . \tag{12}$$

It is shown in Fig. 18 in the form of the dashed lines.

Fitting Parameters						
	jet-η range	a	b	Δa	Δb	$covariance^2$
1	0.0 – 0.4	1.0088		0.0012		
2	0.4 – 0.8	1.0181		0.0011		
3	0.8 – 1.2	1.0177		0.0014		
4	1.2 – 1.6	1.0275		0.0013		
5	1.6 – 2.0	1.0439		0.0011		
6	2.0 – 2.5	1.0811		0.0026		
7	2.5 – 3.0	6.4215	1.0786	2.1074	0.0085	-0.01670
8	3.0 – 3.5	6.2384	1.1301	3.2103	0.0126	-0.03757

Table 5: Fitting pameters and their errors for the functional form of the showering correction, as given by equations (10) and (11).

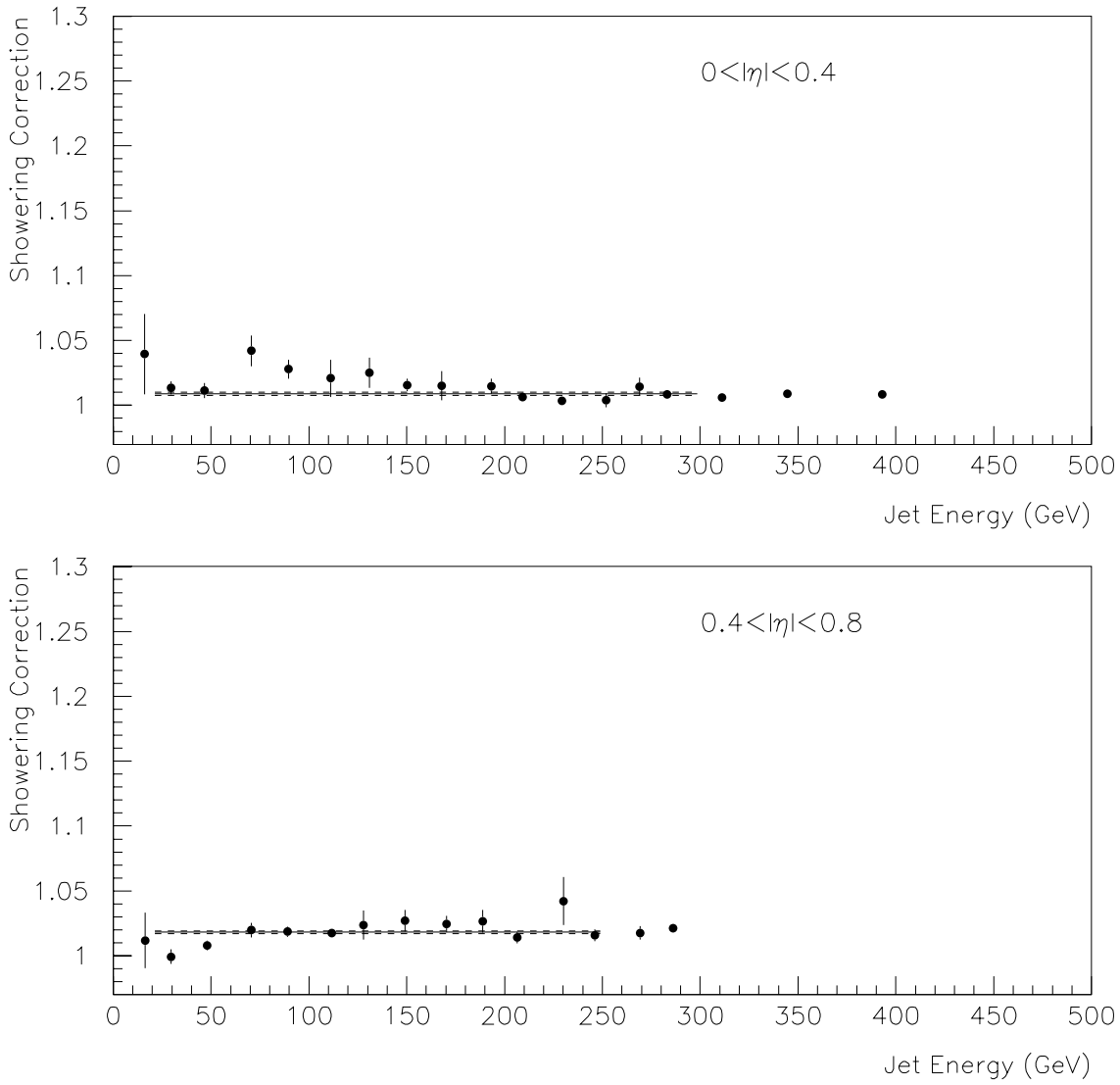

Figure 18: The showering correction in terms of response–corrected jet energy. The dashed lines show the uncertainty in the correction due to the fitting error.

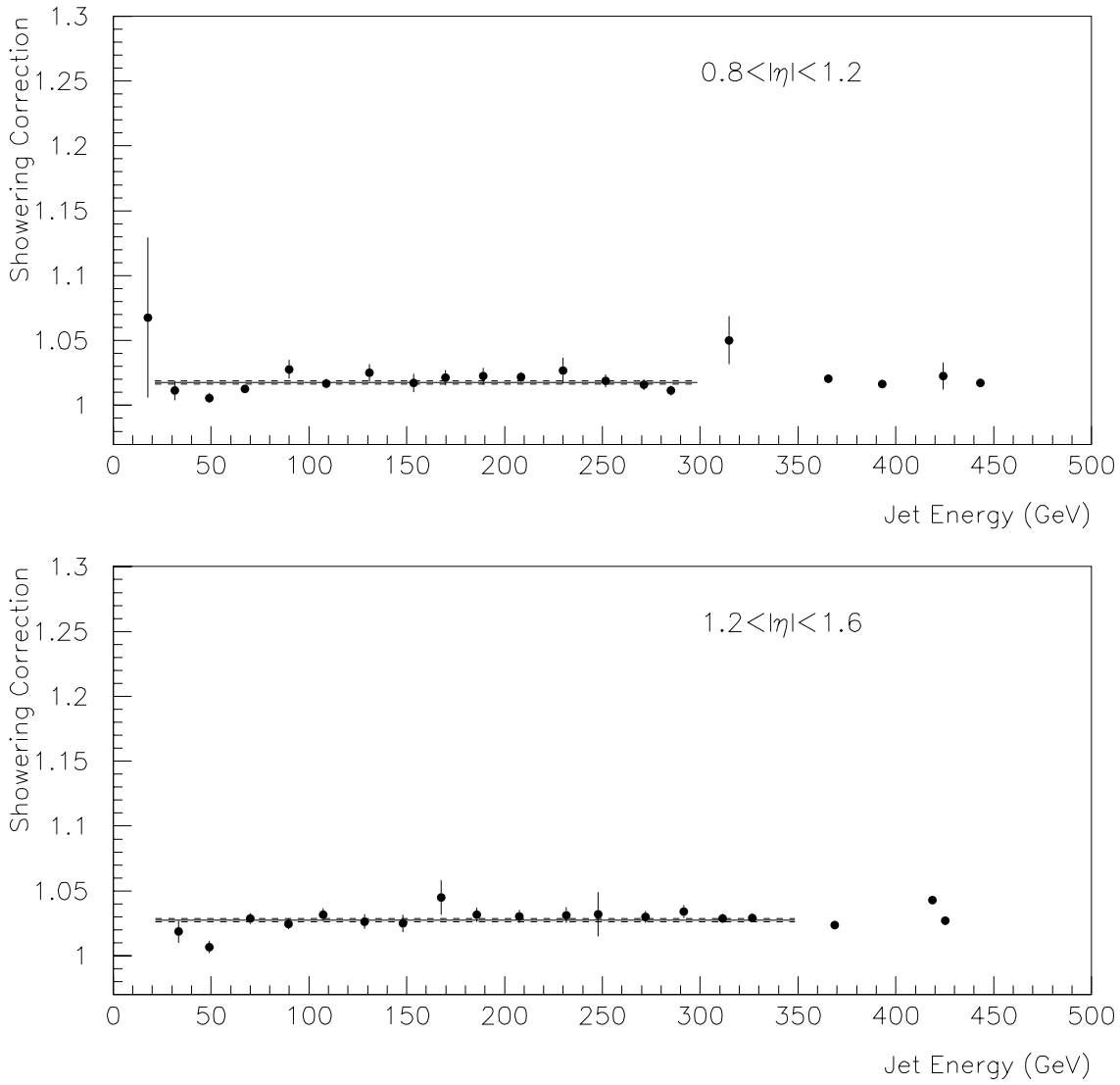

Figure 18: The showering correction in terms of response–corrected jet energy. The dashed lines show the uncertainty in the correction due to the fitting error.

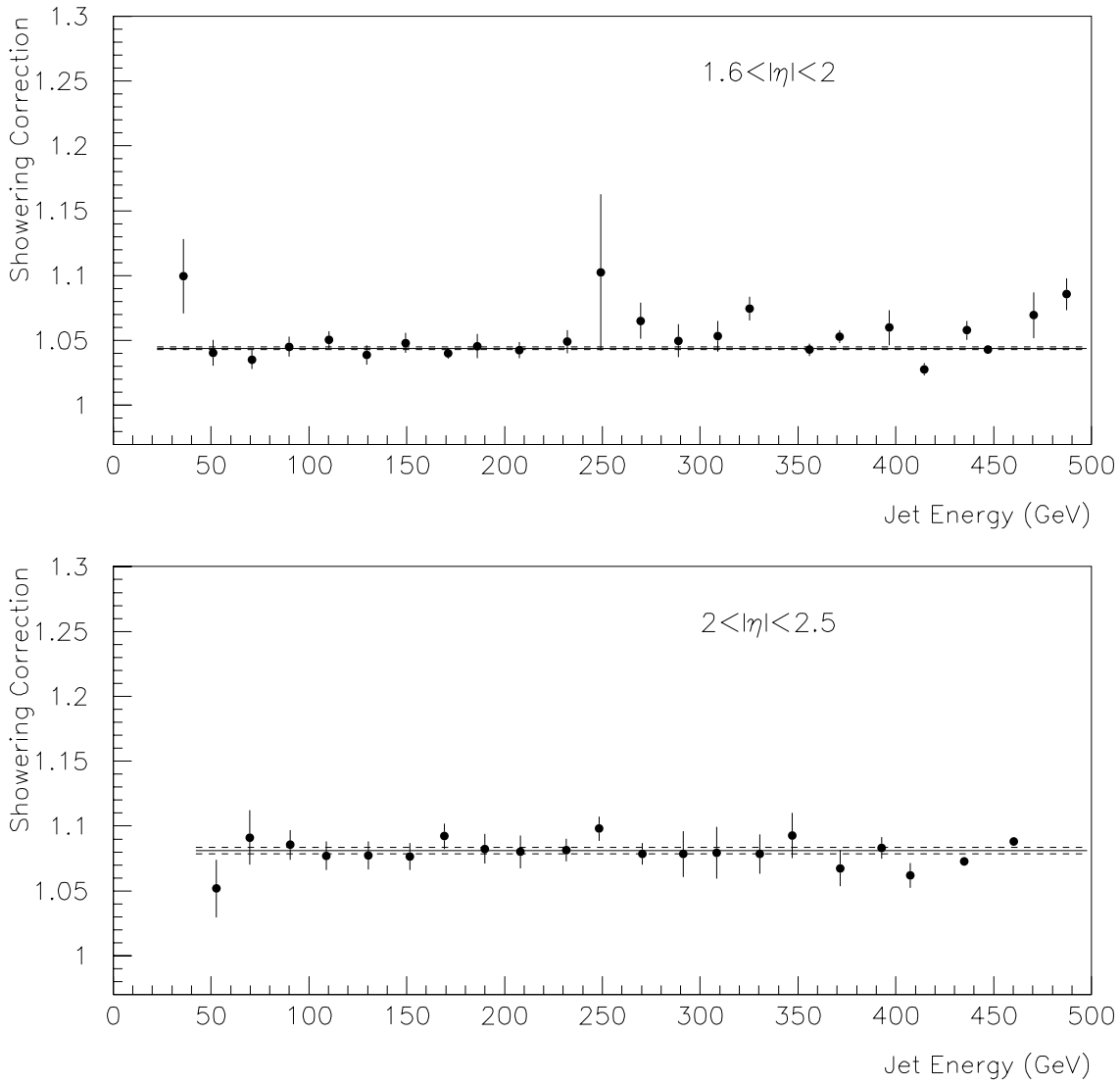

Figure 18: The showering correction in terms of response–corrected jet energy. The dashed lines show the uncertainty in the correction due to the fitting error.

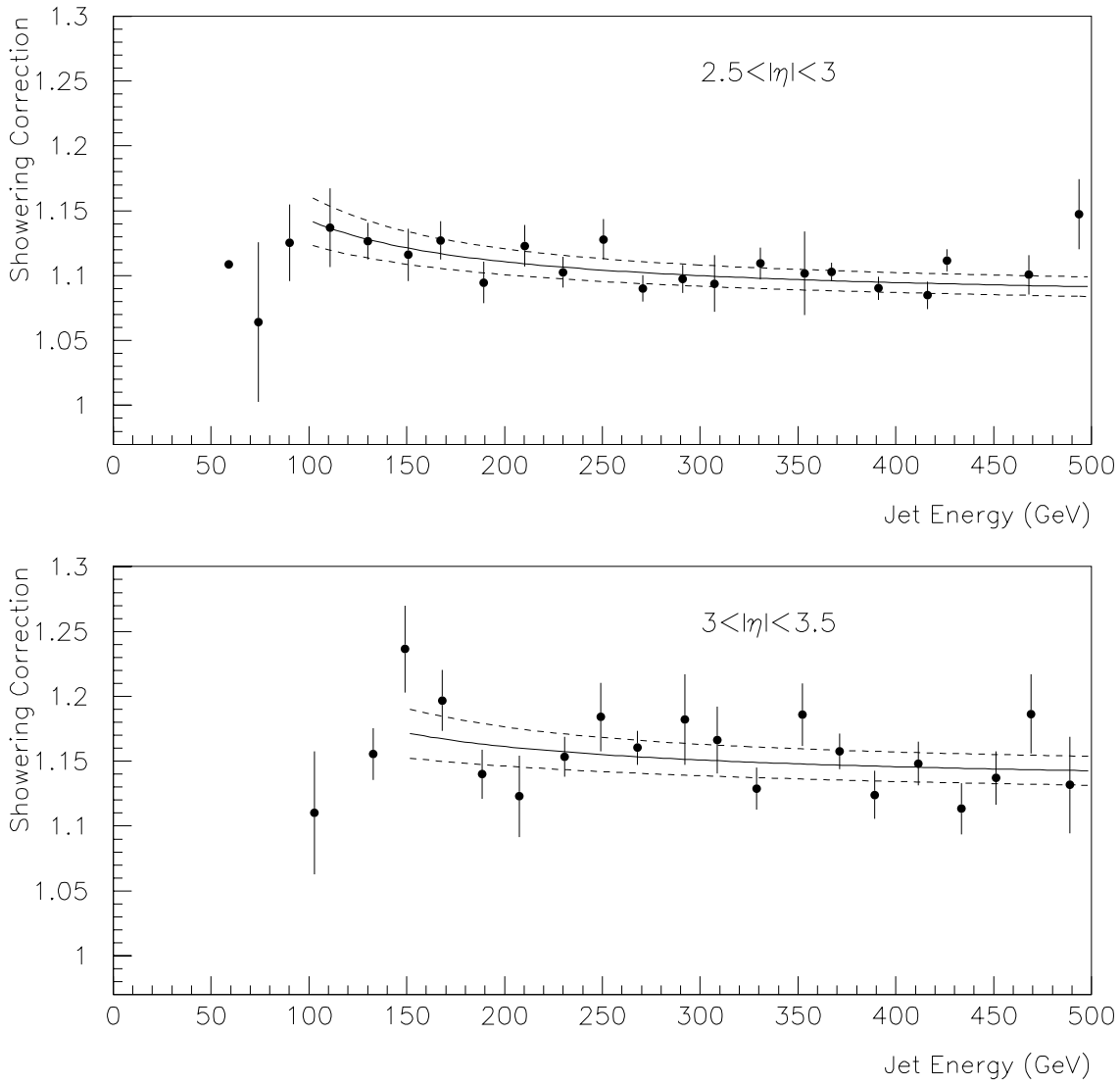

Figure 18: The showering correction in terms of response–corrected jet energy. The dashed lines show the uncertainty in the correction due to the fitting error.

4.5 Varying the Jet Limit

The *jet limit*, i.e. the distance (in $\eta \times \phi$ space) from the calorimeter–jet centroid up to which particles are followed, has been chosen according to the calorimeter–level jet energy density profiles, as the point where the energy density reduces to a small, *constant* value (see section 4.3 and figure 16). Nevertheless, we allow for errors in the estimation of the jet limit by varying it above and below its nominal value, and measuring the corresponding showering correction in each case. We decide on reasonable variations by looking again at Fig.16. In doing so, we also consider the energy dependence of the jet limit: its low(high) value would be more appropriate for the lower(higher) energy bins in each pseudorapidity region. The nominal, low and high values for the jet limit in each pseudorapidity region are listed in Table 6. The variation on the showering correction due to the variation of the jet limit is shown in Fig. 19 and constitutes a systematic uncertainty on the correction (see paragraph 4.6). The fitting parameters of the functional form for the showering correction for the nominal, low and high values of the jet limit in each pseudorapidity region are listed in Table 7.

	Jet Limit			
	jet-η range	Nominal	Low	High
1	0.0 – 0.4	1.0	0.9	1.1
2	0.4 – 0.8	1.1	0.9	1.3
3	0.8 – 1.2	1.2	1.0	1.4
4	1.2 – 1.6	1.2	1.0	1.4
5	1.6 – 2.0	1.3	1.1	1.5
6	2.0 – 2.5	1.5	1.3	1.7
7	2.5 – 3.0	1.5	1.3	1.7
8	3.0 – 3.5	1.6	1.4	1.8

Table 6: Variations of the distance in $\eta \times \phi$ space from the jet centroid where the jet finishes, for calorimeter–level jets of various pseudorapidities.

Fitting Parameters Varying the Jet Limit							
		Nominal		Low		High	
	jet-η range	a	b	a	b	a	b
1	0.0 – 0.4	1.0088		1.0040		1.0122	
2	0.4 – 0.8	1.0181		1.0057		1.0235	
3	0.8 – 1.2	1.0177		1.0095		1.0234	
4	1.2 – 1.6	1.0275		1.0172		1.0347	
5	1.6 – 2.0	1.0439		1.0323		1.0526	
6	2.0 – 2.5	1.0811		1.0668		1.0922	
7	2.5 – 3.0	6.4215	1.0786	5.2037	1.0620	7.7888	1.0899
8	3.0 – 3.5	6.2384	1.1301	4.9117	1.1106	8.6469	1.1429

Table 7: Fitting pameters for the functional form of the showering correction, as given by equations (10) and (11), for the nominal, low and high values of the jet limit.

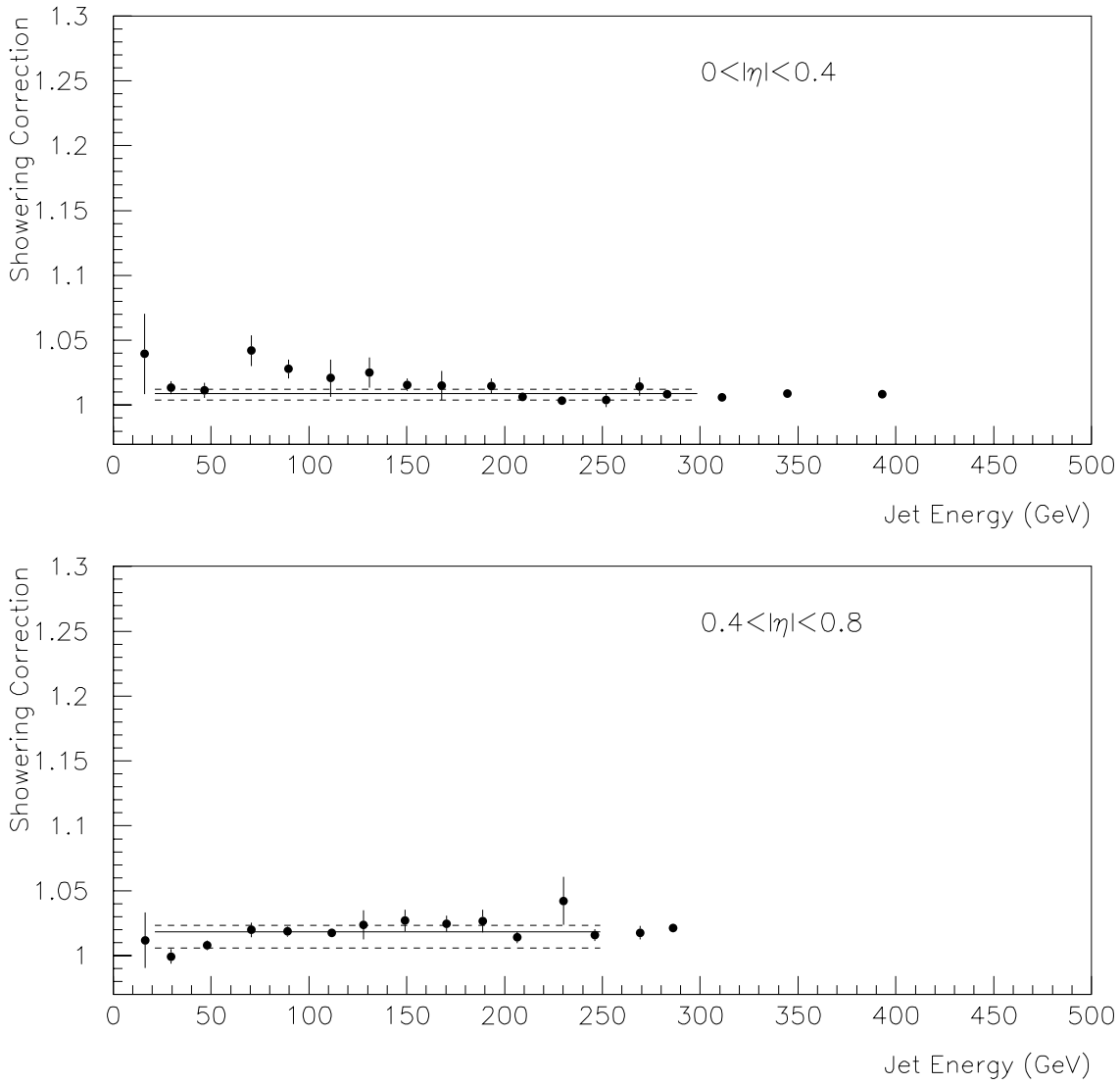

Figure 19: The showering correction in terms of response–corrected jet energy. The solid line shows the correction corresponding to the nominal jet limit. The dashed lines show the uncertainty in the correction due to the variation of the jet limit.

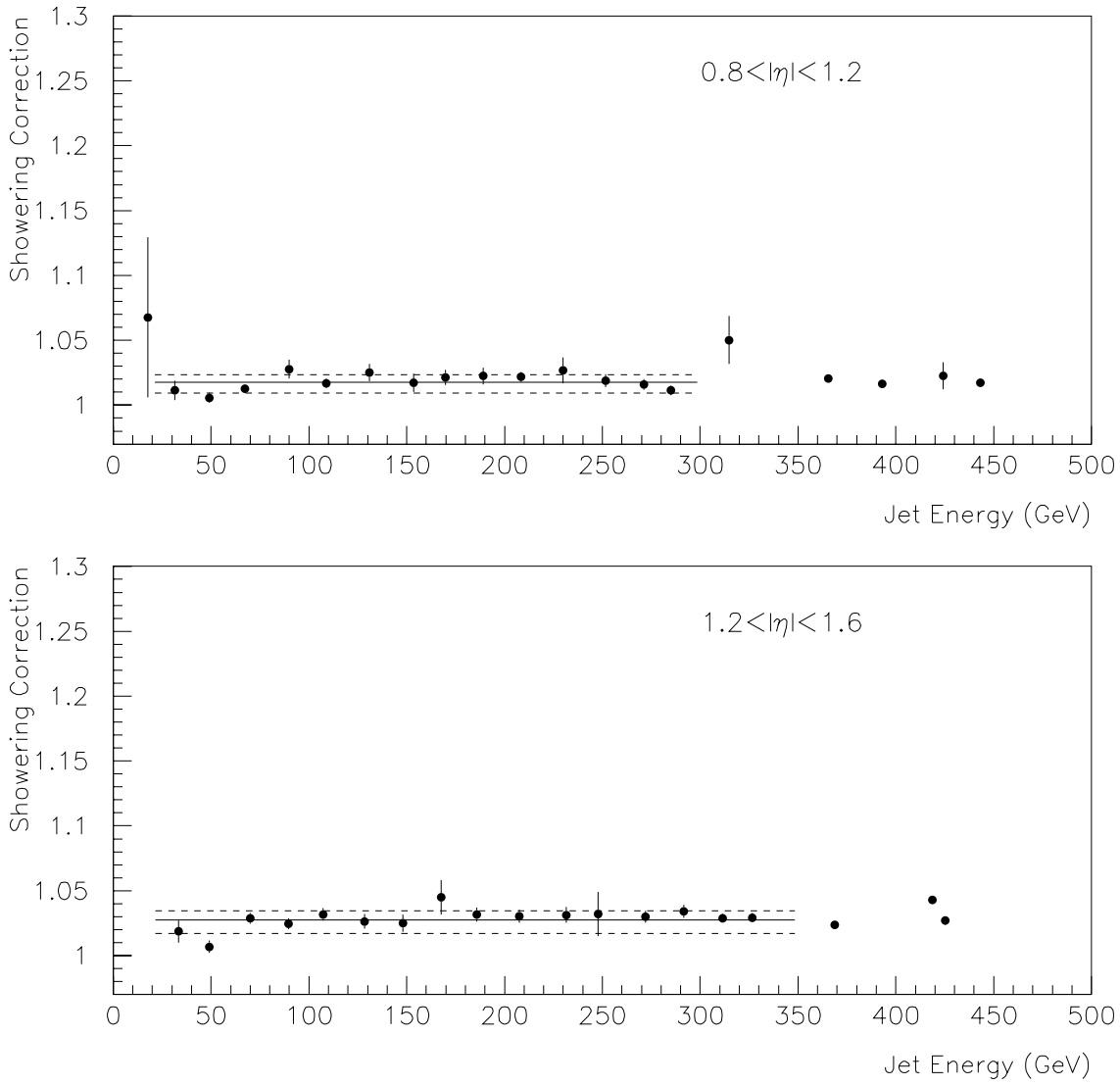

Figure 19: The showering correction in terms of response–corrected jet energy. The solid line shows the correction corresponding to the nominal jet limit. The dashed lines show the uncertainty in the correction due to the variation of the jet limit.

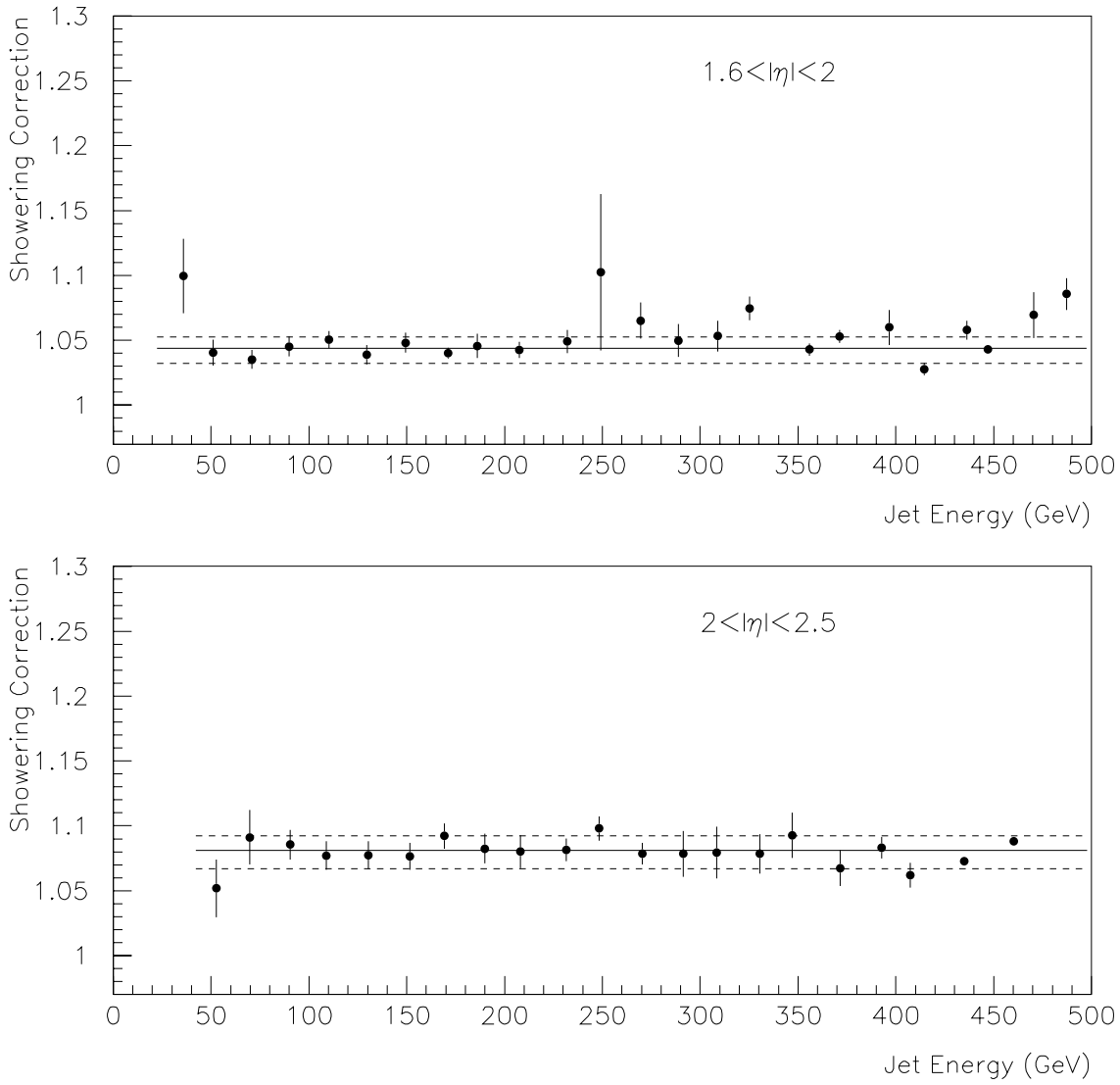

Figure 19: The showering correction in terms of response–corrected jet energy. The solid line shows the correction corresponding to the nominal jet limit. The dashed lines show the uncertainty in the correction due to the variation of the jet limit.

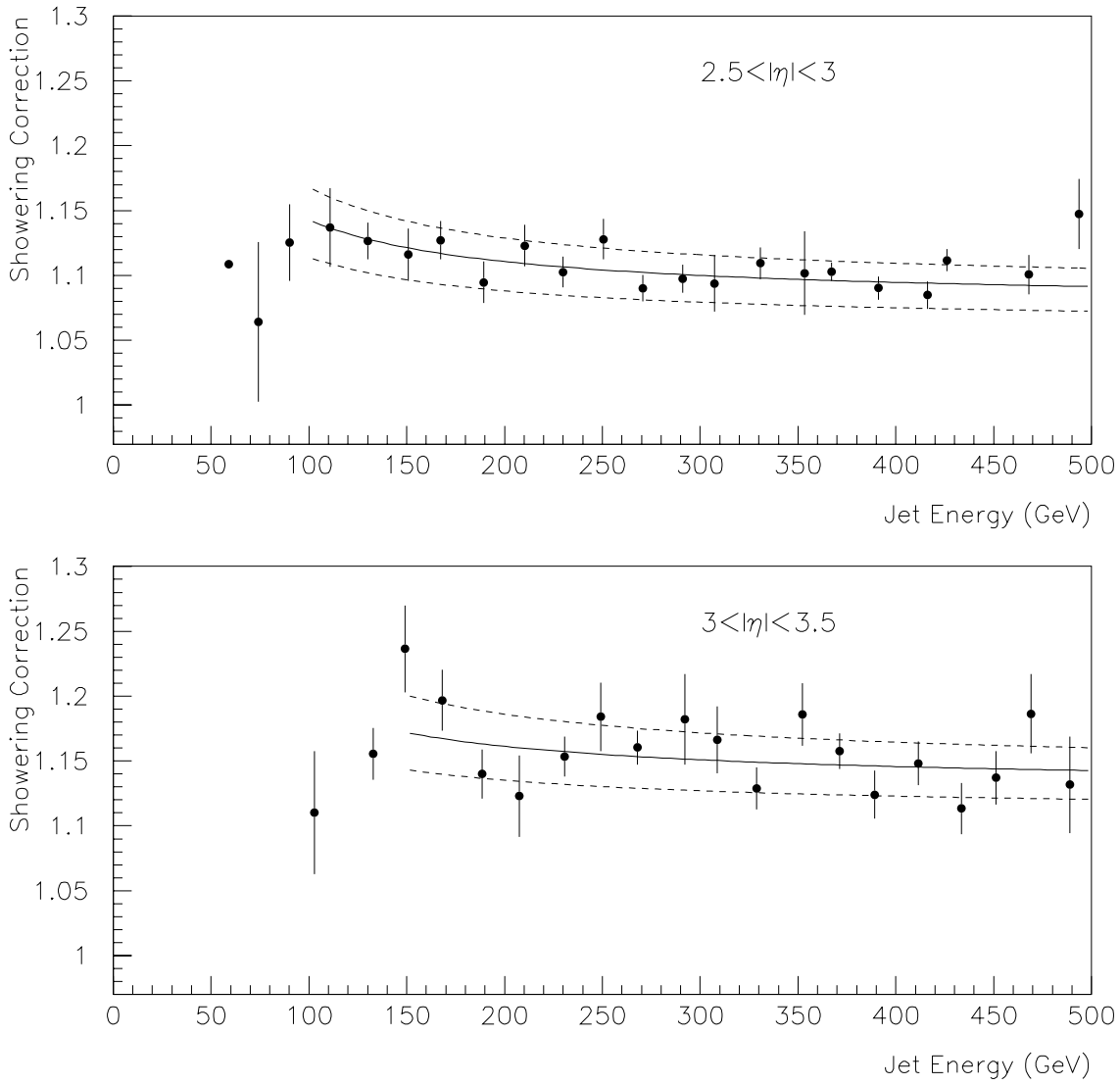

Figure 19: The showering correction in terms of response–corrected jet energy. The solid line shows the correction corresponding to the nominal jet limit. The dashed lines show the uncertainty in the correction due to the variation of the jet limit.

4.6 Uncertainty on the Showering Correction

Sources of uncertainties on the showering correction, as derived from the Monte Carlo sample, include the following:

- the error on the fitting parameters; this is translated into an uncertainty on the correction using the covariance matrix and standard error propagation (see paragraph 4.4). The fitting error is of statistical nature and should be treated as uncorrelated between different jet pseudorapidities and energies;

- the error due to the disagreement between the showering effect in the data and Monte Carlo samples. We use a 2% error for all jet pseudorapidities and energies (see section 3). As it is evident from Fig. 4, the MC showering profiles are wider than the data ones in some pseudorapidity bins, and narrower in others. Moreover, even in a given pseudorapidity bin, there are statistical fluctuations in the MC–data comparison between different energies. Therefore, the 2% error should rather be regarded as uncorrelated between different jet pseudorapidities and energies;

- the use of the *jet limit*. This is controlled by varying the jet limit above and below its nominal value, re–measure the showering correction in each case, and assign the difference as a systematic uncertainty to the nominal correction (see paragraph 4.5). The main function of the jet limit variation is to account for its enery dependence: its low(high) value is more appropriate for the lower(higher) energy bins in each pseudorapidity region. Thus, when comparing jets of different energies in the same pseudorapidity region, the error on the showering correction due to the jet limit should be consider as anti–correlated. On the other hand, when comparing jets of different rapidities but similar energies (i.e. either on the low or on the high end of the energy range), this error could be consider as correlated.

The total uncertainty on the showering correction is derived by adding in quadrature all the errors described above. It is shown in Fig. 20 in the form of the dashed lines.

In addition, we have perfomed the following tests:

- the particle energy response, by which each cell energy is weighted, has been varied from the value measured in the Monte Carlo (see Fig. 14) to unity, and to a function similar to the particle energy response measured in test–beam data [8]. There was no effect on the showering correction in both cases.

- to test for potential effects of large energy resolutions of the low energy particles, the showering correction has been measured by excluding particles with energies smaller than 0.5, 1, 1.5 and 2 GeV. No effect was observed; this is reasonable, given the fact that most of the energy showered outside the 0.7 cone originates from the high–energy particles at the "hard" core of the jet (see Fig. 12).

Uncontrolled sources of systematic uncertainties in the derivation of the showering correction in CAFIX 5.1, that are either eliminated or controlled in the current study, include the following:

- the MPF method has a large intrinsic bias due to showering, which was not accounted for in CAFIX 5.1;
- the correction depends on the jet limit, especially in the forward pseudorapidity regions. The uncertainty on the correction due to the choice of the jet limit, especially since the latter is not only a function of pseudorapidity but also of jet energy, was not accounted for in CAFIX 5.1;
- in deriving the showering correction from the jet energy profiles, there was a considerable uncertainty in estimating the baseline energy, especially since a single point after the jet limit was used. There is no need for estimating a baseline energy with the Monte Carlo method;
- in CAFIX 5.1, the physics out–of–cone energy (gluon emission or fragmentation at the particle level) had to be subtracted from the total measured out–of–cone energy. The assumption had been made that the physics out–of–cone energy present in the data can been taken equal to the physics out–of–cone energy in HERWIG. In the current study, no assumption needs to be made, since the comparison is done between particle– and calorimeter–levels of the same Monte Carlo;
- in deriving the showering correction from the data jet energy profiles in CAFIX 5.1, various selection criteria had to be applied, pertinent to the quality of the jets in the data, the luminosity dependence, the splitting and merging performed by the jet algorithm, etc. On the contrary, the only requirement applied to the Monte Carlo sample is the selection of dijet events, to ensure good isolation between jet cones;
- the cell energy in the Monte Carlo can be corrected for response. This was not possible in CAFIX 5.1, since we do not have a calorimeter–cell energy scale.

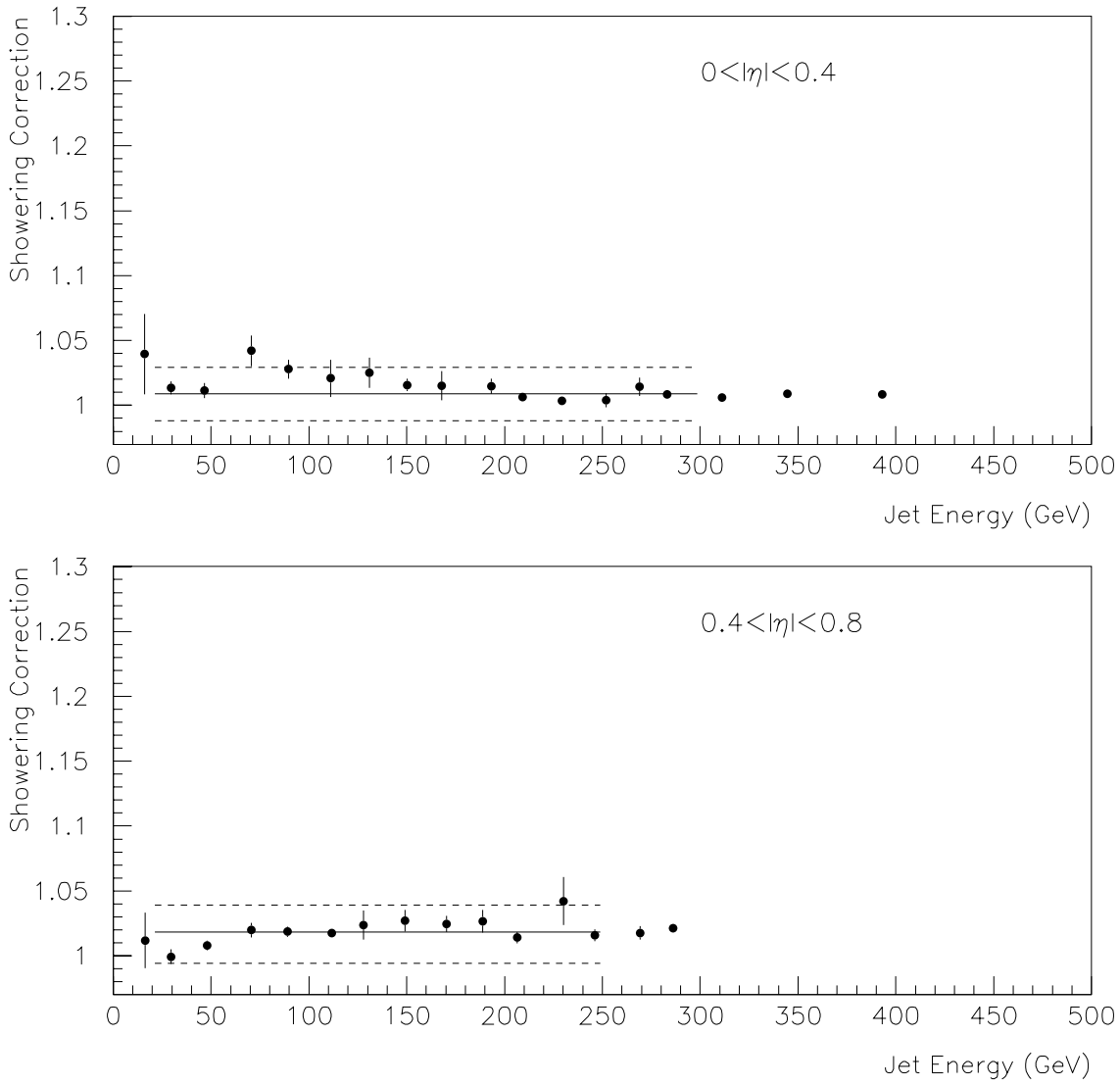

Figure 20: The showering correction in terms of response–corrected jet energy. The dashed lines show the total uncertainty on the correction.

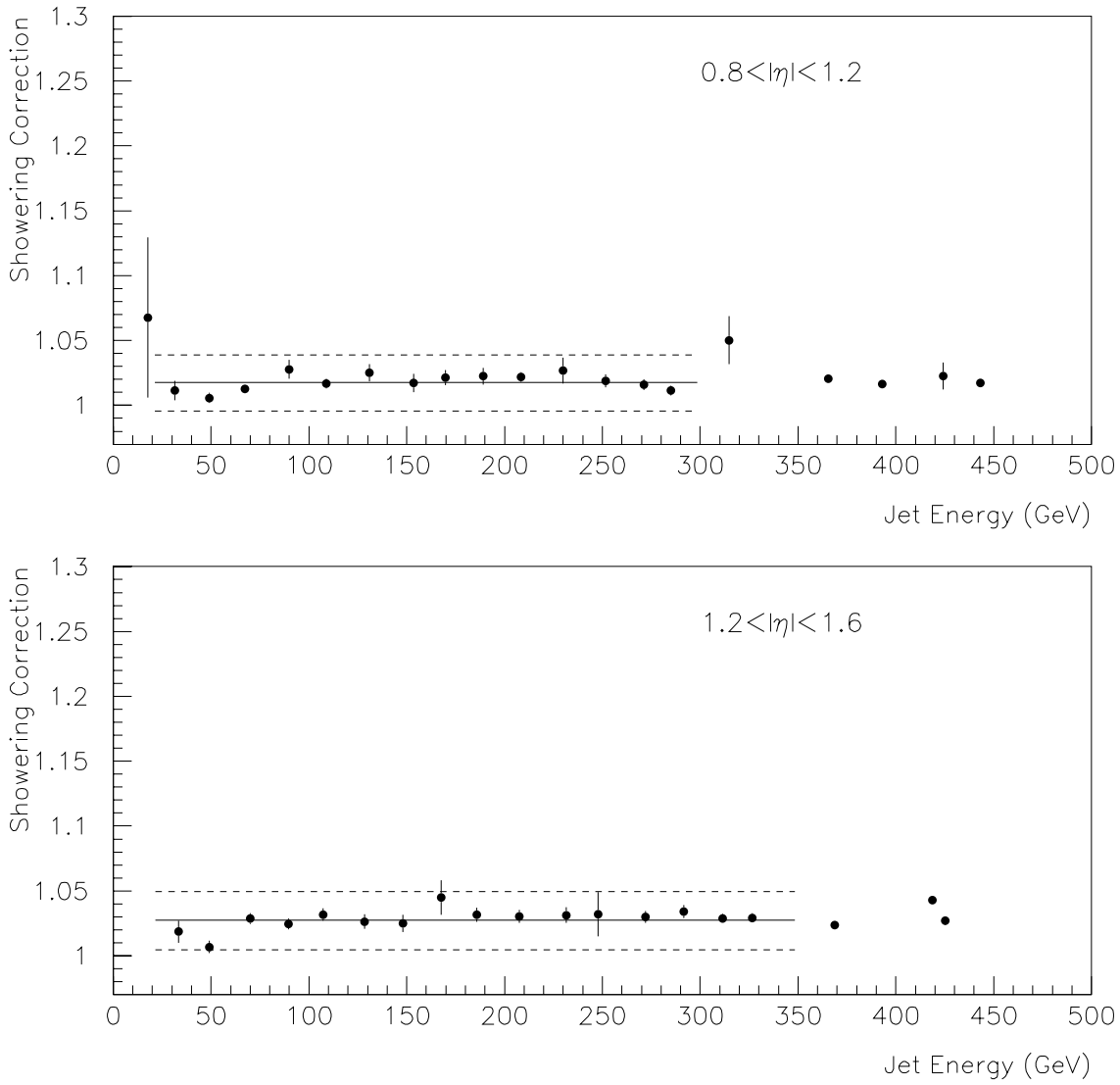

Figure 20: The showering correction in terms of response–corrected jet energy. The dashed lines show the total uncertainty on the correction.

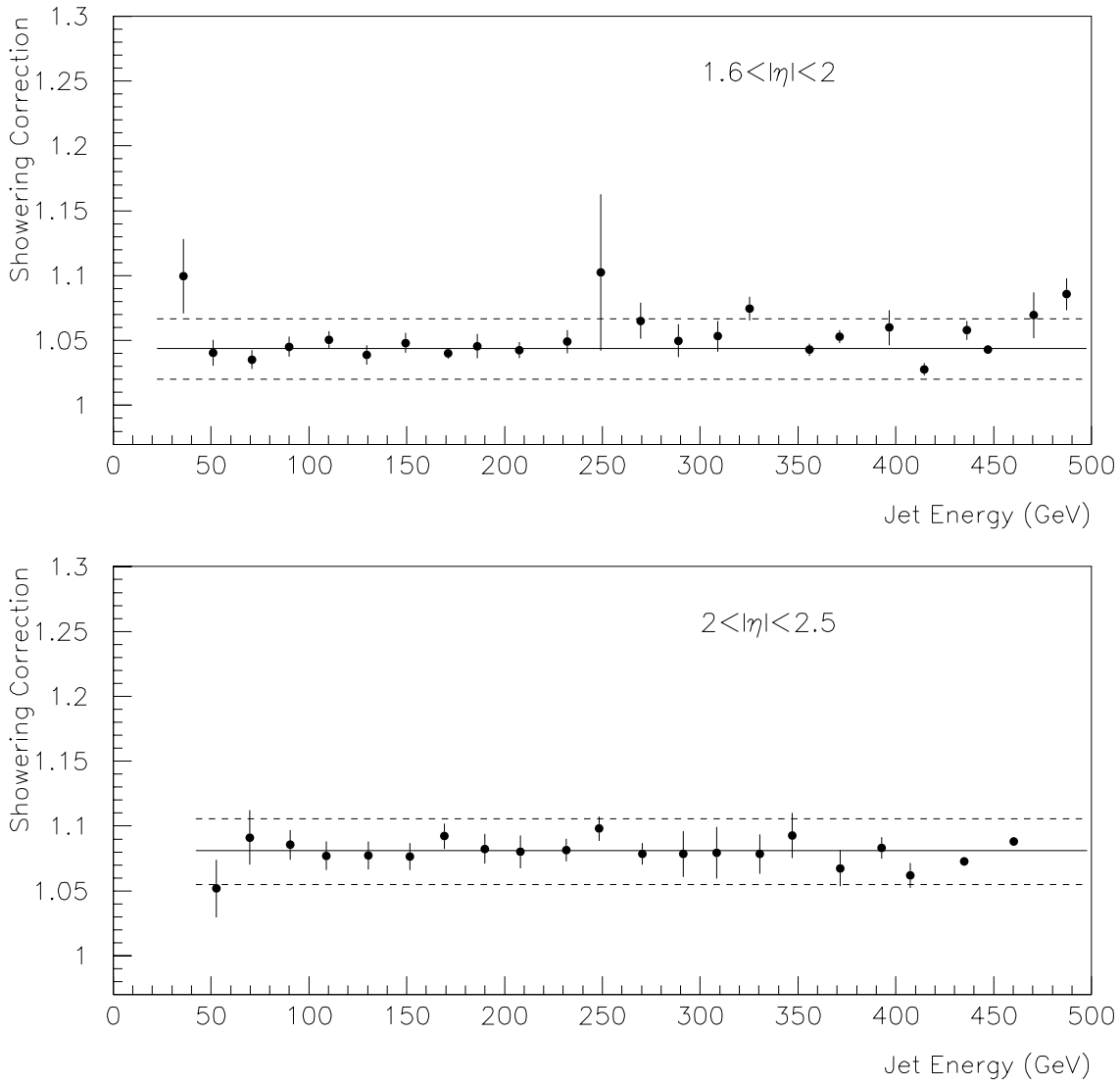

Figure 20: The showering correction in terms of response–corrected jet energy. The dashed lines show the total uncertainty on the correction.

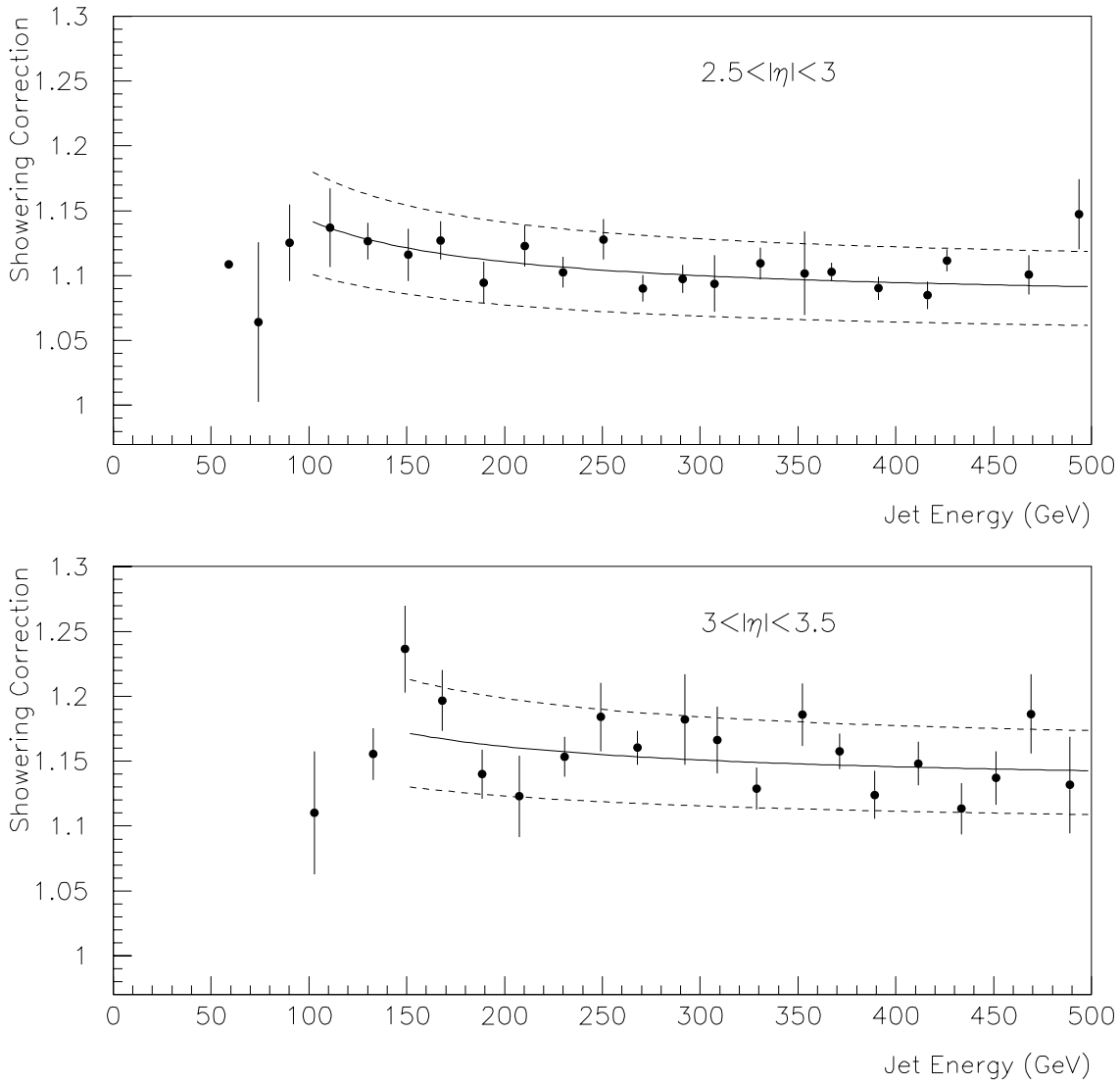

Figure 20: The showering correction in terms of response–corrected jet energy. The dashed lines show the total uncertainty on the correction.

5 Closure Test

The validity of the method for deriving the showering correction is tested by comparing the calorimeter–level jet energy after the correction is applied to the jet energy at the particle–level: in the limit of perfect calorimeter energy response, the first should be equal to the second. In reality, the jet energy measured at the calorimeter should first be corrected for imperfect response.

5.1 The Jet Energy Response

The jet energy response in the calorimeter is measured in a way similar to the particle energy response, as described in paragraph 4.2. We consider all particles that belong to a particle–level jet (PJET). We follow each one of these particles to the calorimeter, and sum all the calorimeter–cell energy deposits that originated from them. The ratio of the above energy sum to the sum of the energies of the particles of the PJET provides the calorimeter jet energy response in the Monte Carlo. The inverse of the jet energy response, i.e. the response correction necessary for the closure test (see next paragraph), is shown in Fig. 21.

It should be noted here that the jet energy response in the Monte Carlo should *not* be compared with the response measured in the data using the MPF method [2] for two reasons:

- the jet energy response in the Monte Carlo is due solely to the imperfection of the calorimeter (material response, gaps, etc.). On the contrary, the "response" in the data using the MPF method is the combined effect of the calorimeter imperfection and the bias of the method due to the showering of the particles. The latter is a large effect;

- the GCAH banks, where the MC jet energy response is derived from, contain cell energies as measured in the liquid Argon and Uranium parts of the calorimeter. On the contrary, the CAEH banks (the standard calorimeter cell energy banks at the reconstruction level) contain only the energy in the liquid Argon, adjusted by sampling weights. Therefore, the particle/jet energy response as derived here, although perfectly valid to correct each cell energy in the derivation of the showering correction, or to correct the Monte Carlo jets for closure–test purposes, is not necessarily representative of the actual calorimeter energy response as measured in the data (the latter are available only in the form of the CAEH banks).

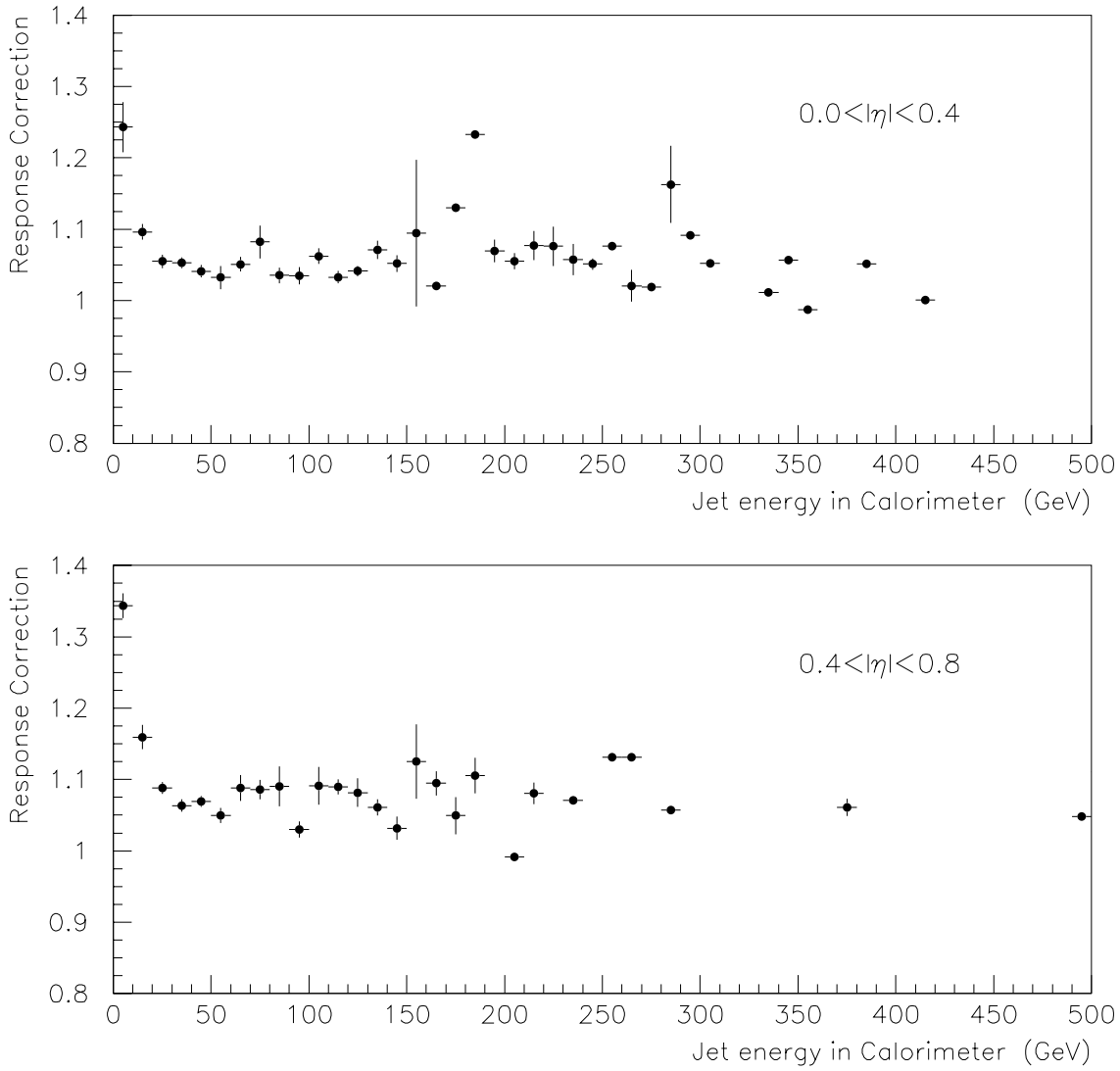

Figure 21: The jet energy response correction in terms of the jet energy in the calorimeter (all particles of the PJET considered).

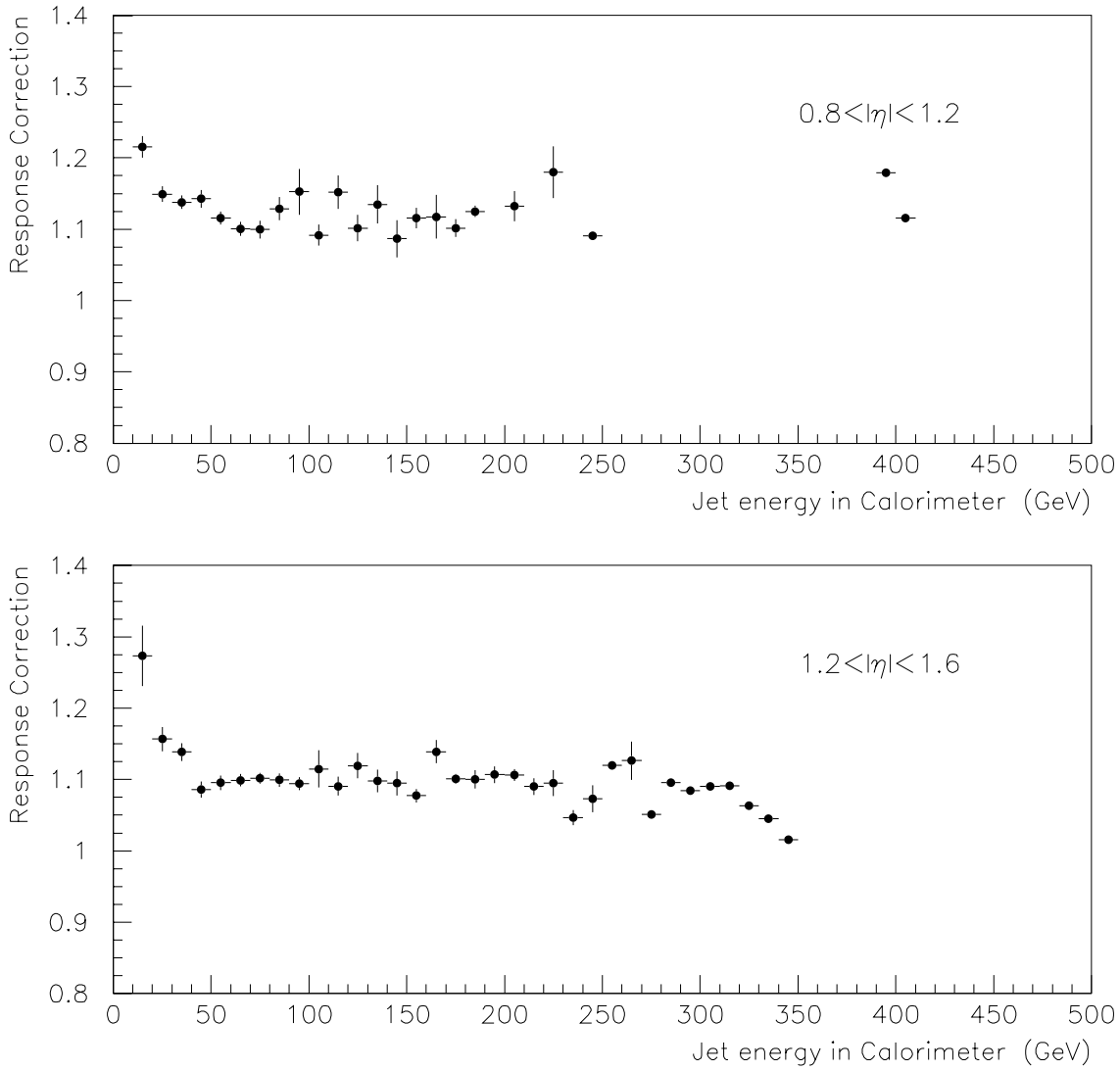

Figure 21: The jet energy response correction in terms of the jet energy in the calorimeter (all particles of the PJET considered).

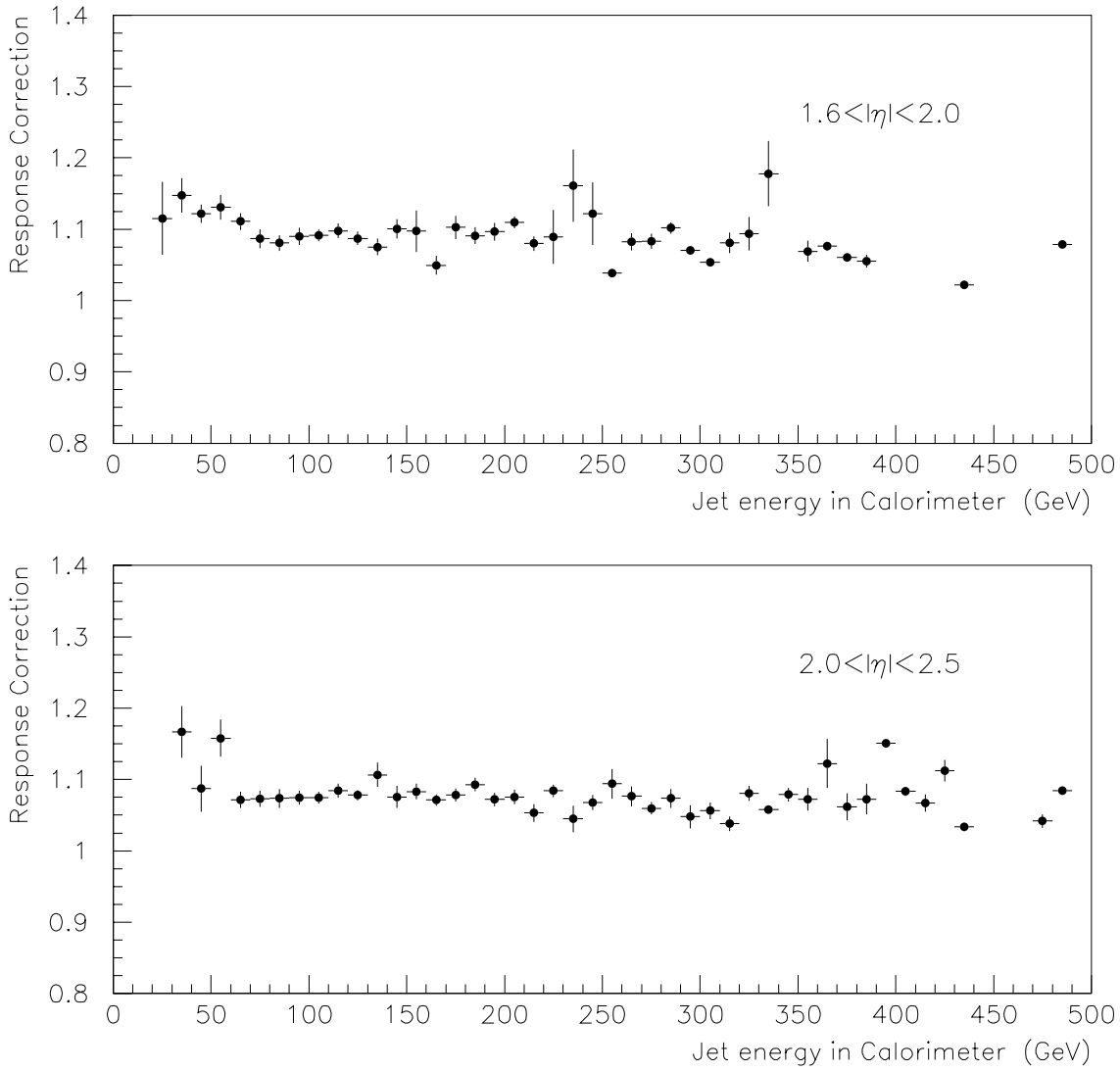

Figure 21: The jet energy response correction in terms of the jet energy in the calorimeter (all particles of the PJET considered).

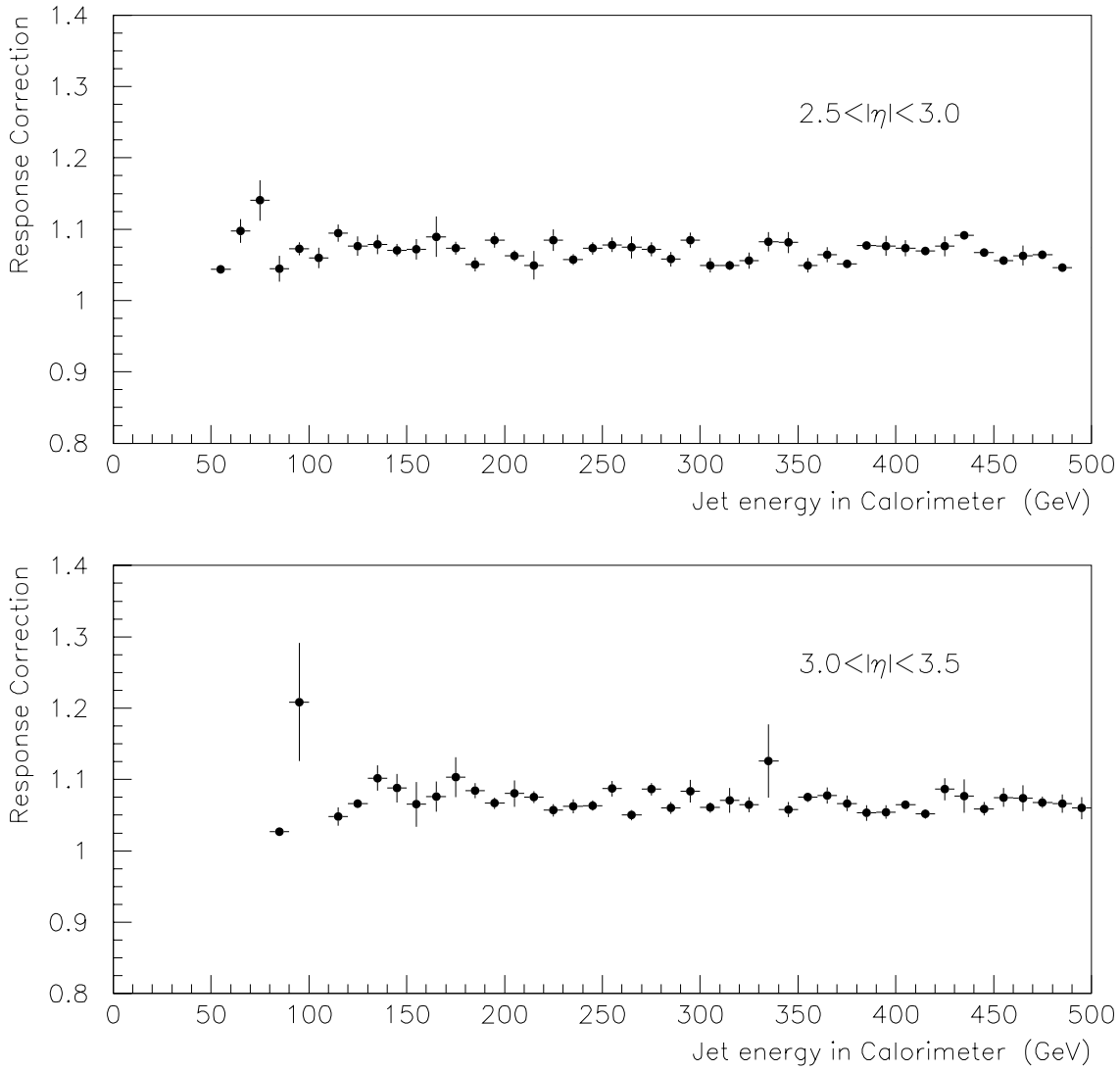

Figure 21: The jet energy response correction in terms of the jet energy in the calorimeter (all particles of the PJET considered).

5.2 Testing the Method

In order to test our method for deriving the showering correction, we compare the response–corrected calorimeter–level jets, before and after the showering correction, to the particle–level ones. As a reminder, it should be mentioned again (see section 2) that the Monte Carlo has been generated without underlying event, and no detector noise has been added, i.e. no offset–energy correction is needed.

The comparison is shown in Fig. 22. The ratio of the calorimeter–level to the particle–level jet energy is plotted versus the response–corrected calorimeter–measured energy, for different stages of the calorimeter–level energy:

- as measured in the calorimeter (open squares);
- after response correction (open triangles). In practice, instead of fitting the jet energy response correction of the previous paragraph and applying it on the average, we correct each calorimeter cell with its corresponding particle energy response, in exactly the same way it is done in the derivation of the showering correction;
- after showering correction, derived using the nominal jet limit (full triangles);
- after showering correction, derived without enforcing a jet limit (full circles).

In all pseudorapidity regions and for all jet energies, the "raw" showering correction (i.e. without the jet limit) corrects the calorimeter–level jet energy exactly back to the particle level, proving the validity of the method.

The showering correction with the jet limit appears to underestimate the correction needed for showering effects, especially in the forward regions. In reality, however, what appears to be missing from the showering correction is in fact the fraction of the jet energy that has already been restored in the data by the bias of the MPF method (see section 4.3). To show this in a more clear way, we plot again the ratio of the calorimeter–level to the particle–level jet energy in Fig. 23 (note the different scales in the plots for different pseudorapidity bins): after response correction (open triangles), after showering correction with the jet limit (full triangles), and after the MPF–residual showering correction (no jet limit), as derived from Eq. (9) (full squares). *The ratio of the residual–showering–corrected jet energy to the true energy shows the MPF bias.* Note that the latter is a *function of jet energy.*

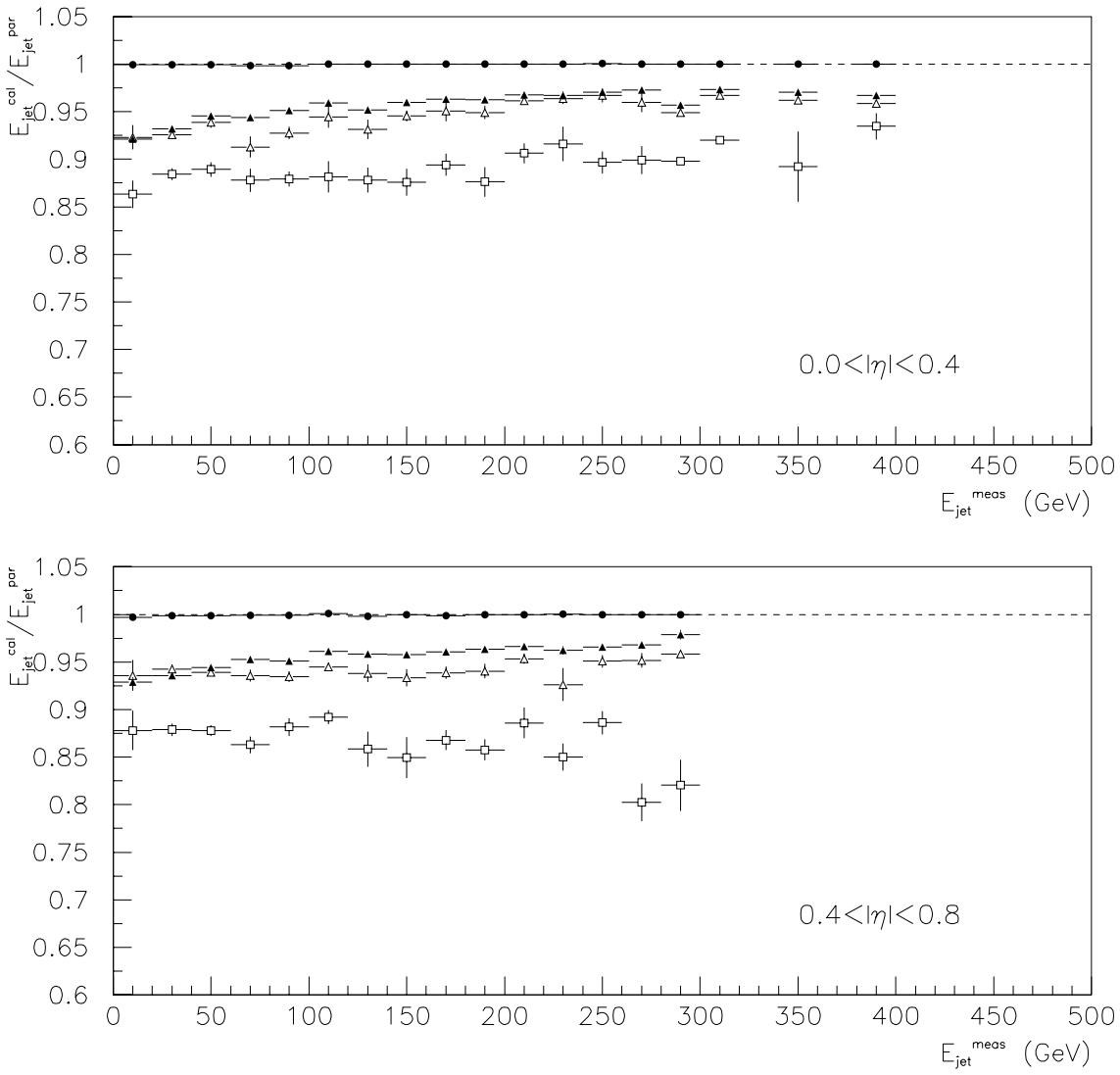

Figure 22: The ratio of calorimeter–level to particle–level jet energies in terms of the response–corrected calorimeter–measured jet energy. The ratio is shown for different stages of the calorimeter–level energy: as measured (open squares), after response correction (open triangles), after showering correction with the jet limit (full triangles), and after showering correction without jet limit (full circles).

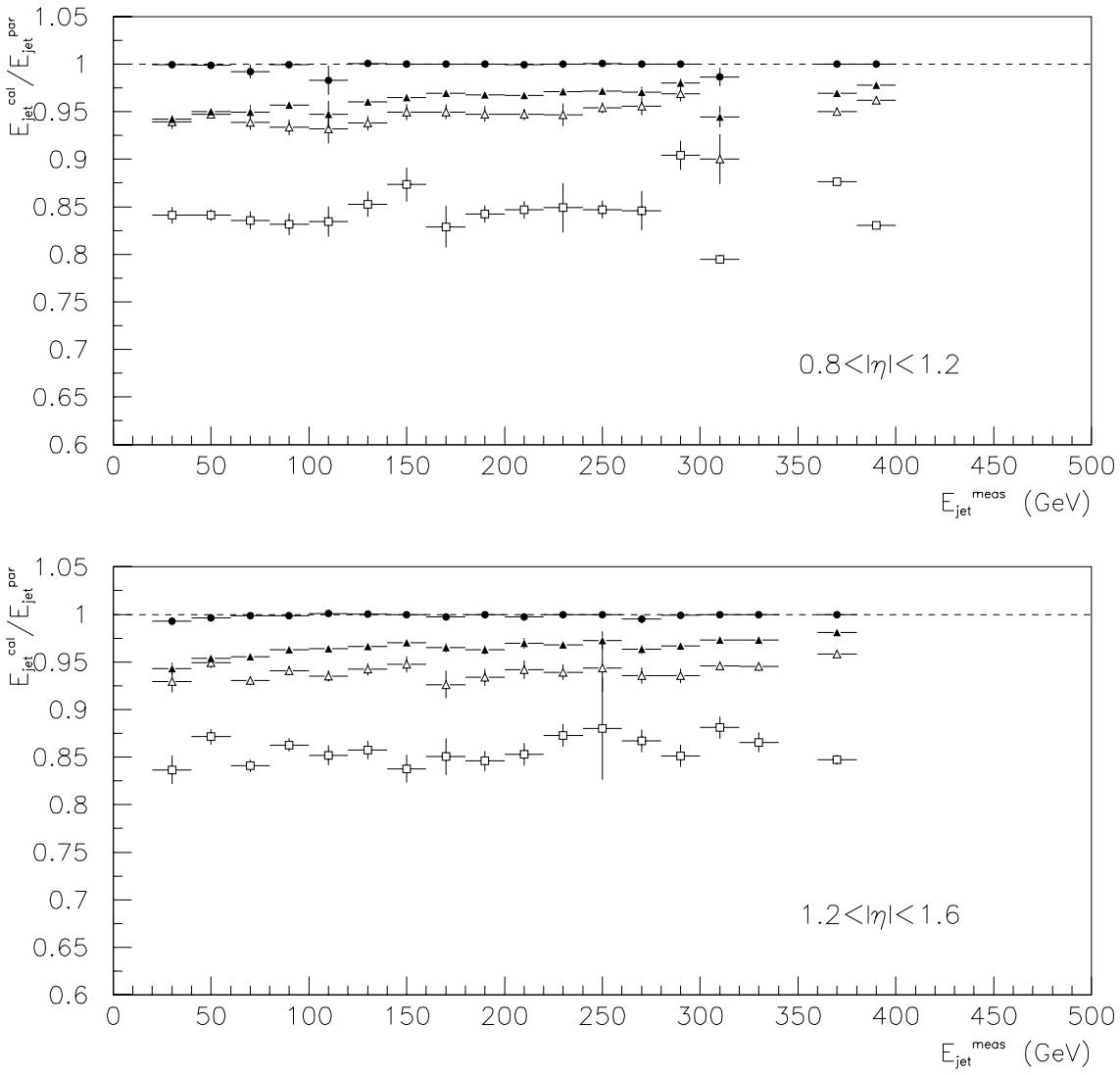

Figure 22: The ratio of calorimeter–level to particle–level jet energies in terms of the response–corrected calorimeter–measured jet energy. The ratio is shown for different stages of the calorimeter–level energy: as measured (open squares), after response correction (open triangles), after showering correction with the jet limit (full triangles), and after showering correction without jet limit (full circles).

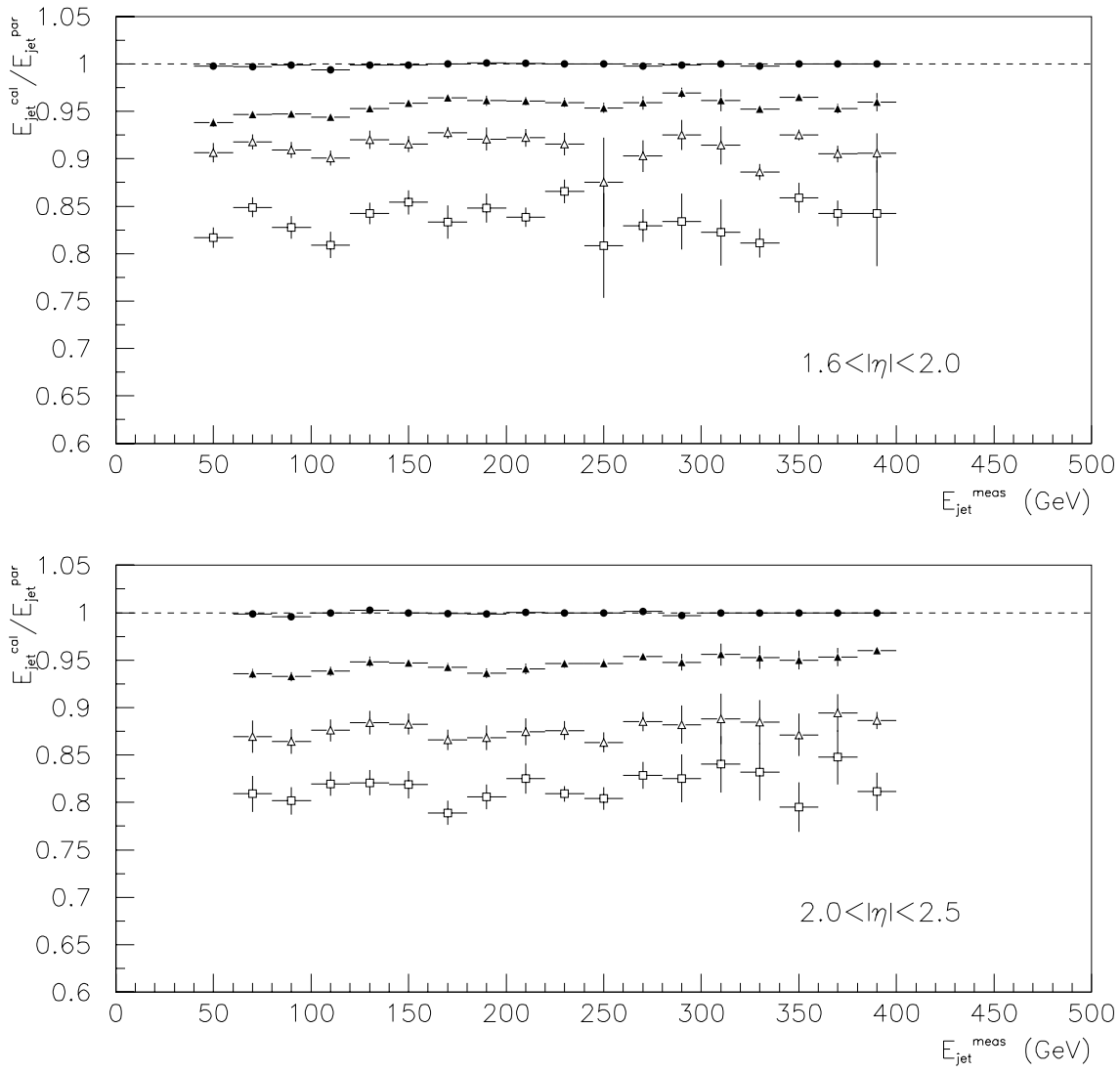

Figure 22: The ratio of calorimeter–level to particle–level jet energies in terms of the response–corrected calorimeter–measured jet energy. The ratio is shown for different stages of the calorimeter–level energy: as measured (open squares), after response correction (open triangles), after showering correction with the jet limit (full triangles), and after showering correction without jet limit (full circles).

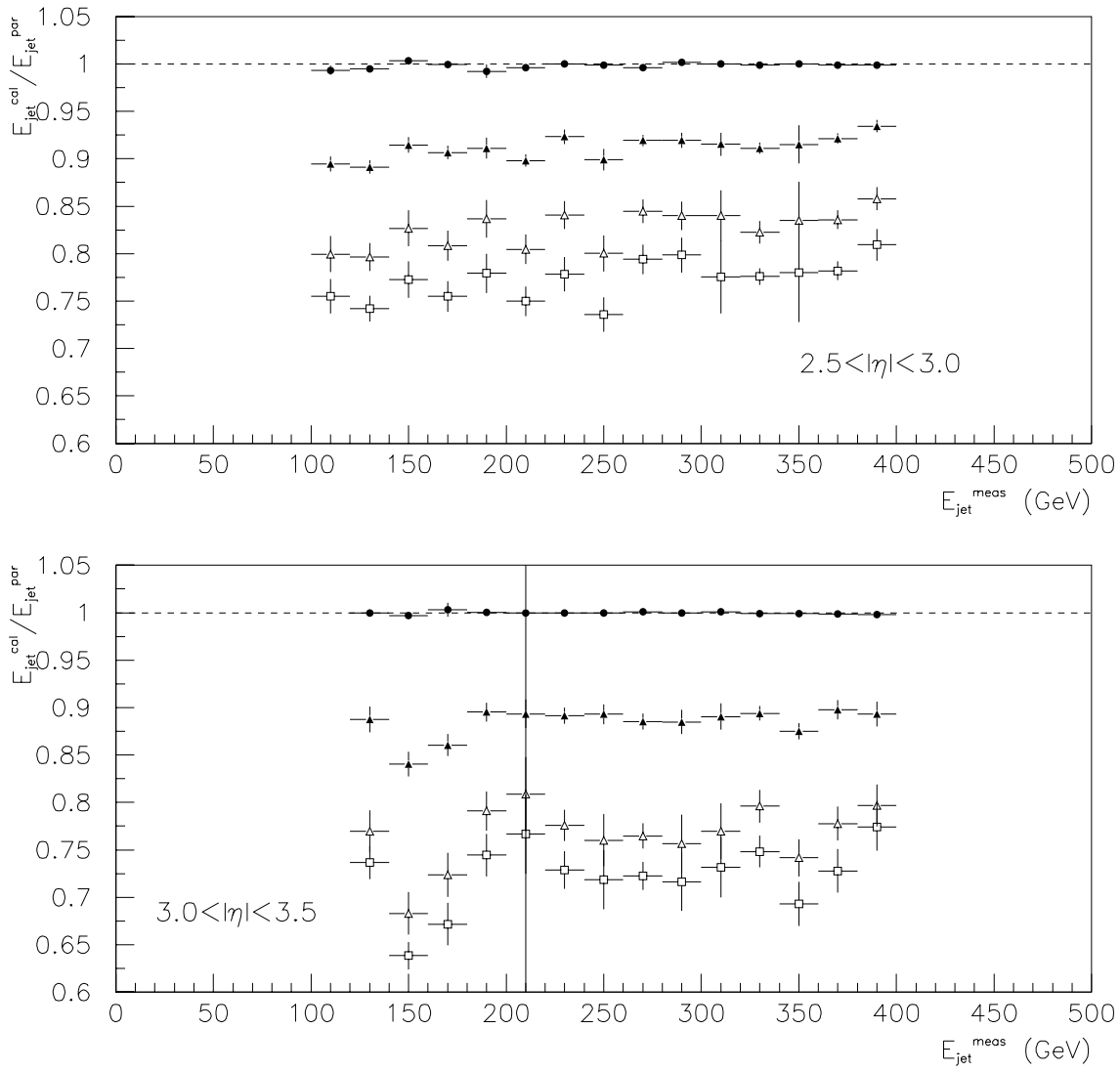

Figure 22: The ratio of calorimeter–level to particle–level jet energies in terms of the response–corrected calorimeter–measured jet energy. The ratio is shown for different stages of the calorimeter–level energy: as measured (open squares), after response correction (open triangles), after showering correction with the jet limit (full triangles), and after showering correction without jet limit (full circles).

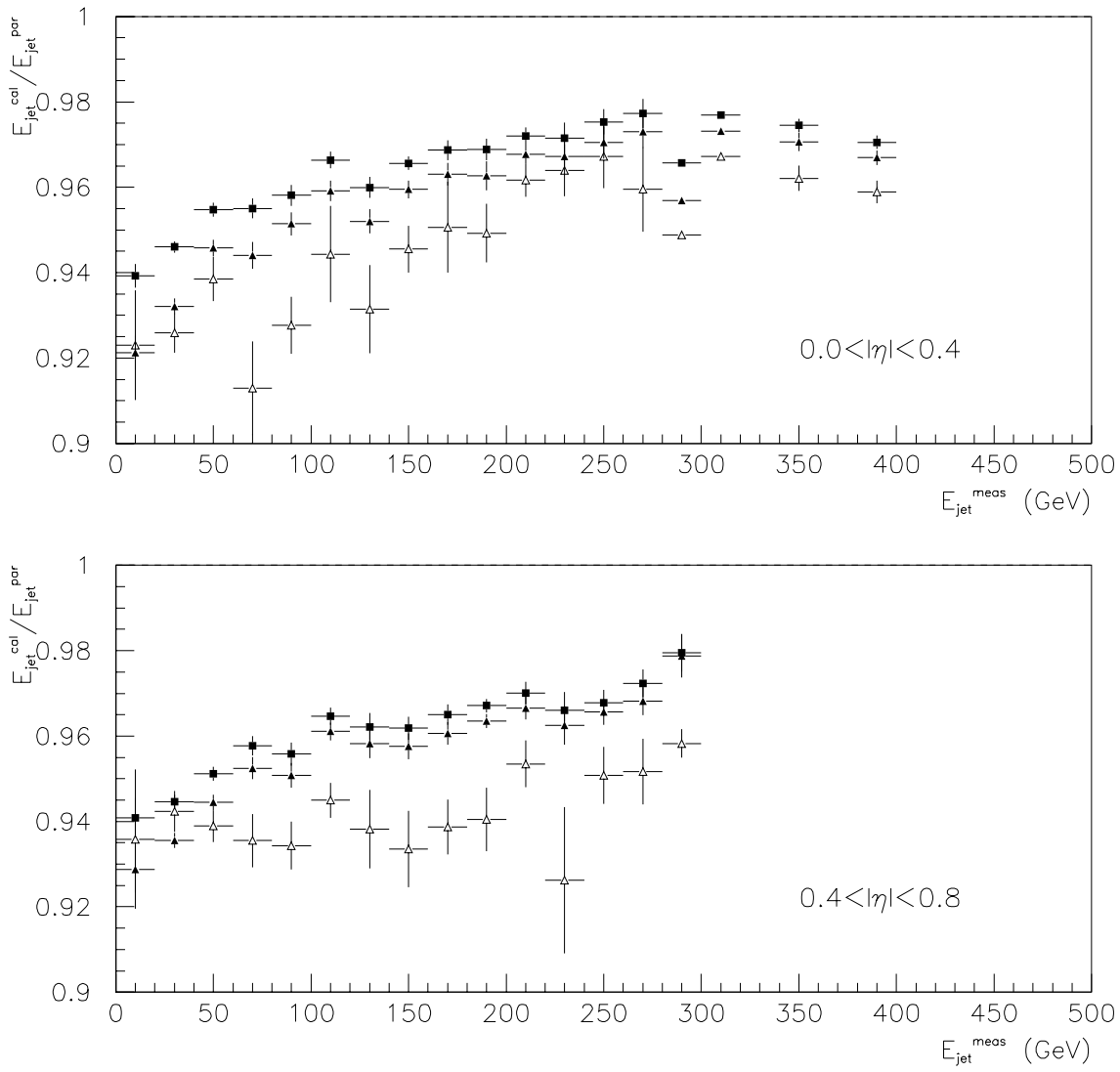

Figure 23: The ratio of calorimeter–level to particle–level jet energies in terms of the response–corrected calorimeter–measured jet energy. The ratio is shown for different stages of the calorimeter–level energy: after response correction (open triangles), after showering correction with the *jet limit* (full triangles), and after *MPF–residual* showering correction (full squares).

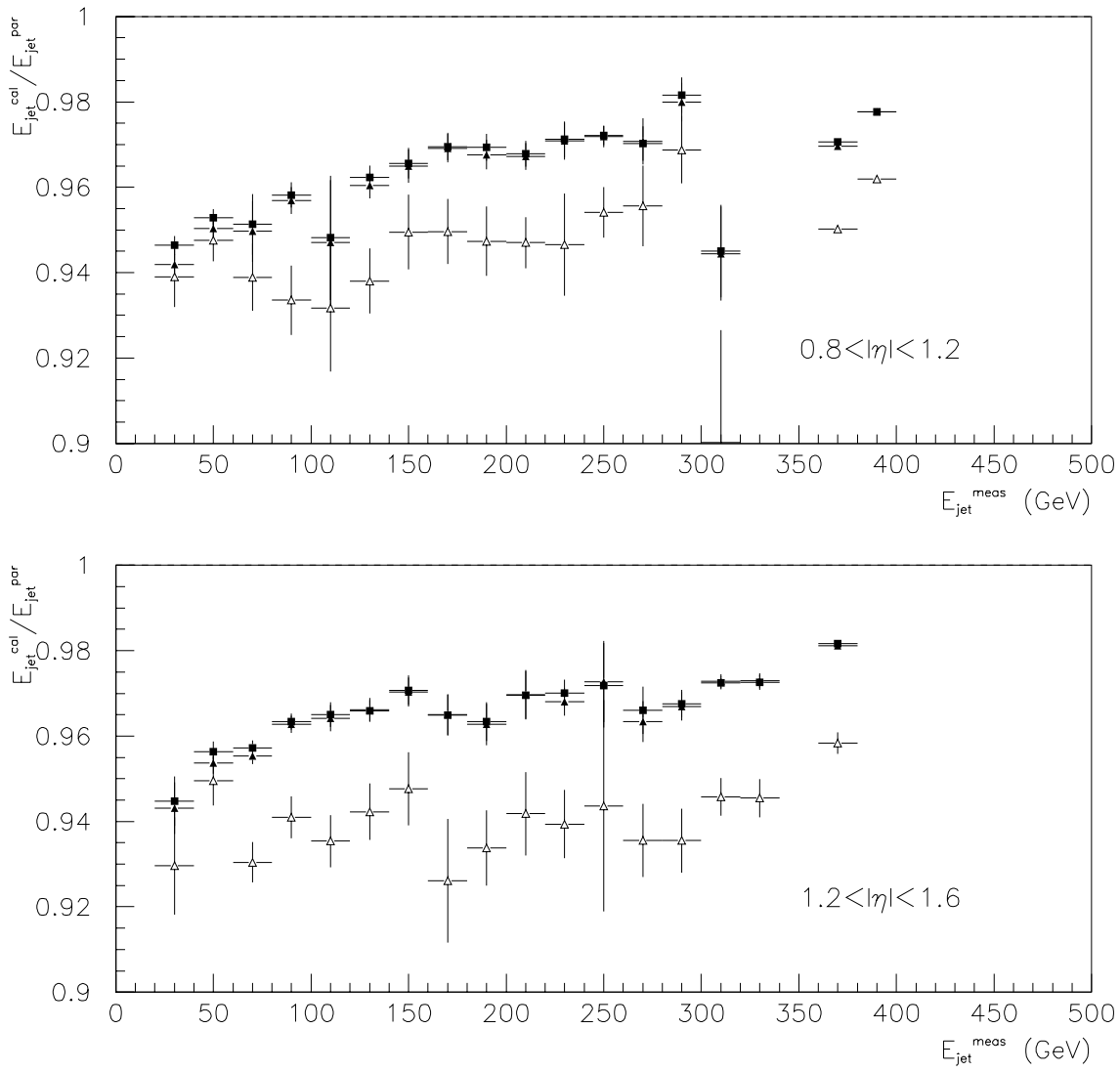

Figure 23: The ratio of calorimeter–level to particle–level jet energies in terms of the response–corrected calorimeter–measured jet energy. The ratio is shown for different stages of the calorimeter–level energy: after response correction (open triangles), after showering correction with the *jet limit* (full triangles), and after *MPF–residual* showering correction (full squares).

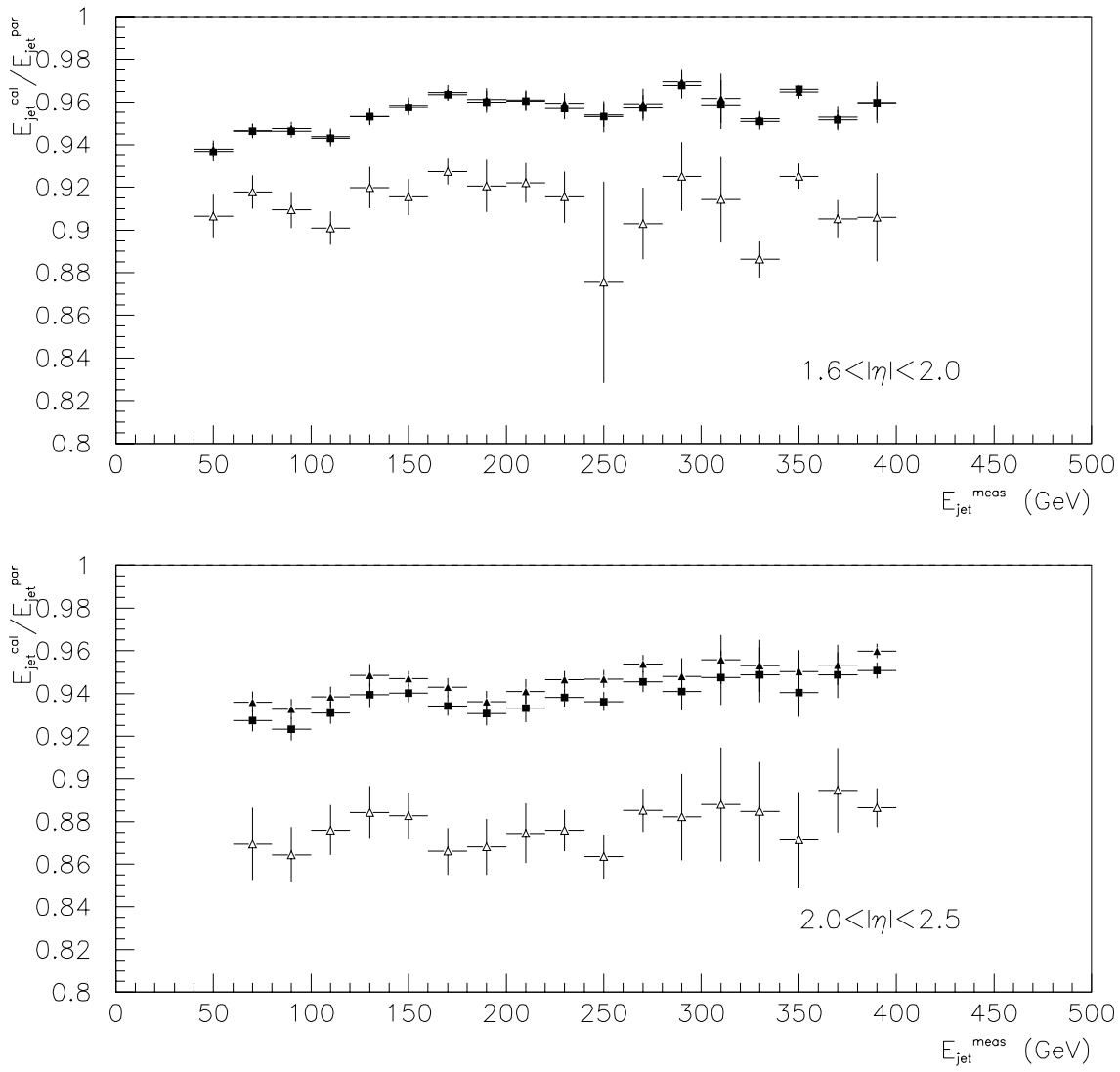

Figure 23: The ratio of calorimeter–level to particle–level jet energies in terms of the response–corrected calorimeter–measured jet energy. The ratio is shown for different stages of the calorimeter–level energy: after response correction (open triangles), after showering correction with the *jet limit* (full triangles), and after *MPF–residual* showering correction (full squares).

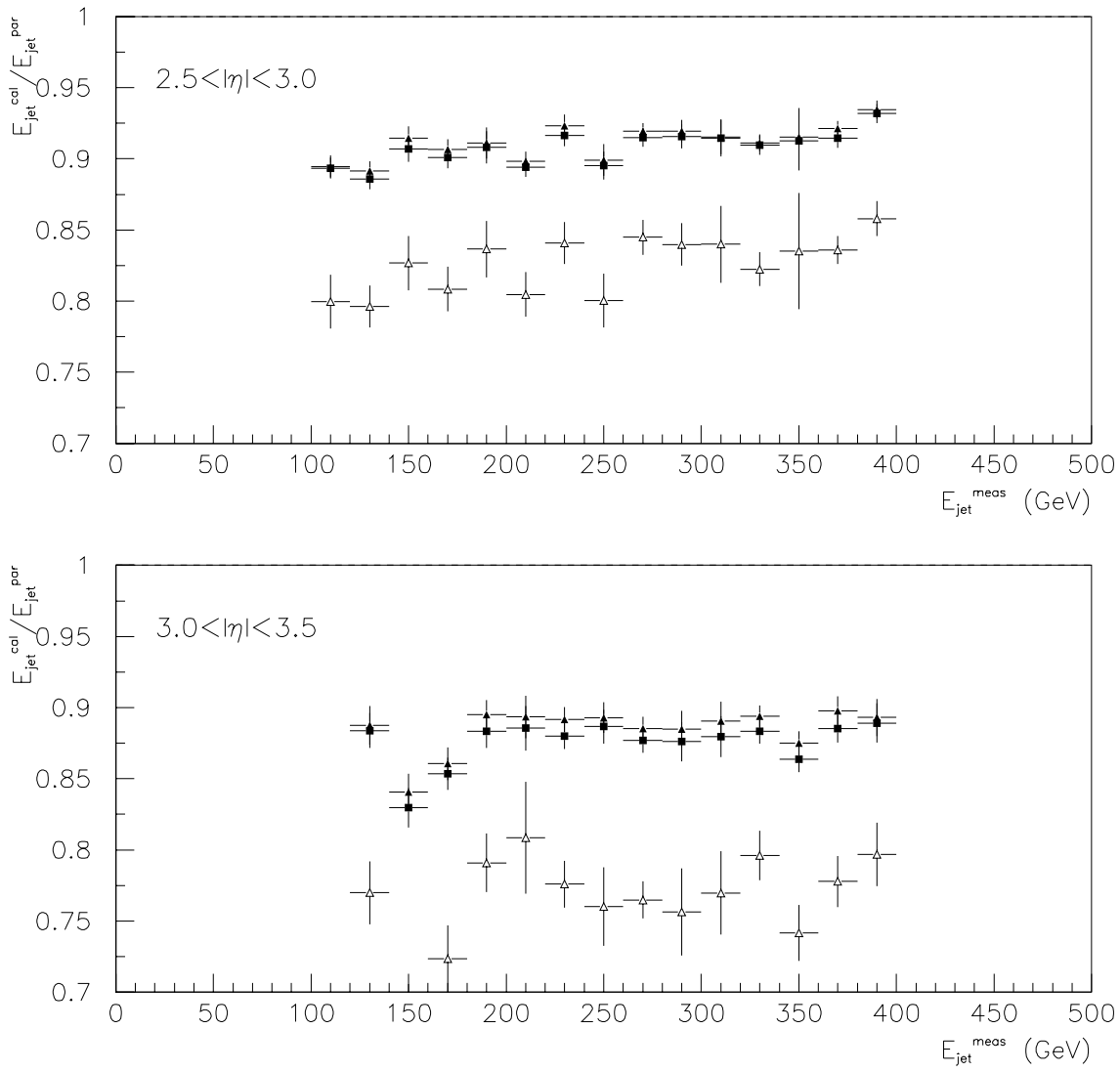

Figure 23: The ratio of calorimeter–level to particle–level jet energies in terms of the response–corrected calorimeter–measured jet energy. The ratio is shown for different stages of the calorimeter–level energy: after response correction (open triangles), after showering correction with the *jet limit* (full triangles), and after *MPF–residual* showering correction (full squares).

6 Comparison to CAFIX 5.1

The comparison between the showering correction derived from the Monte Carlo and the correction derived from the showering profiles in CAFIX 5.1 is shown in two sets of figures.

In Fig. 24 the new correction is shown in the form of solid lines (dashed lines for the uncertainty) and the old one in the form of dashed-dotted lines (dotted for the uncertainty). The points correspond to the new correction. In the Central Calorimeter, $0 < |\eta| < 0.8$, the new correction has a larger uncertainty than the error assigned to the old correction (the difference is at most 1%). In the ICR and forward region, $0.8 < |\eta| < 2$, the old and new errors are of about the same magnitude. In the very forward region, $|\eta| > 2$, the Monte Carlo derived showering correction reduces the uncertainty of the CAFIX 5.1 correction by a factor of 3 at lower energies (low and intermediate E_T's) and a factor of 2 at higher energies.

In Fig. 25 the difference between the two corrections is shown in the form of solid lines. The uncertainty on the difference (shown in the form of dashed lines) has been caclulated from the uncertainties on the two corrections with standard error propagation. In all pseudorapidity regions, the new correction shows much less dependence on the jet energy than the old one. In the central and IC regions, the difference between the two corrections is at the 1–2% level. In the forward regions, for energies between 200–300 GeV, the new correction is larger than the old by 2% at $1.6 < |\eta| < 2.0$, 3% at $2.0 < |\eta| < 2.5$, and 4% at $2.5 < |\eta| < 3.0$. The difference in each pseudorapidity region then grows with jet energy. This is not surprising, if we remember that the profile method starts having problems at large pseudorapidities and high energies, due to the uncertainty in the estimation of the baseline energy that needs to be subtracted from the jet showering profiles (see section 3).

As a general comment, when comparing the two corrections, one should keep in mind the following:

- the MPF method corrects the jet energies not only for calorimeter response but also for part of the showering;
- the profile method for the extraction of the showering correction is very approximate; it includes a large number of systematic effects, whose magnitude we do not know;
- CAFIX 5.1 as a whole has been tested with SHOWERLIB Monte Carlo. In the latter, the development of the particle shower in the calorimeter is not accurate enough.

Convoluting the above three factors in CAFIX 5.1, in an effort to understand what part of the showering effect was corrected for by MPF, what part was recovered by the profile method, and what part was tested by SHOWERLIB, is rather difficult.

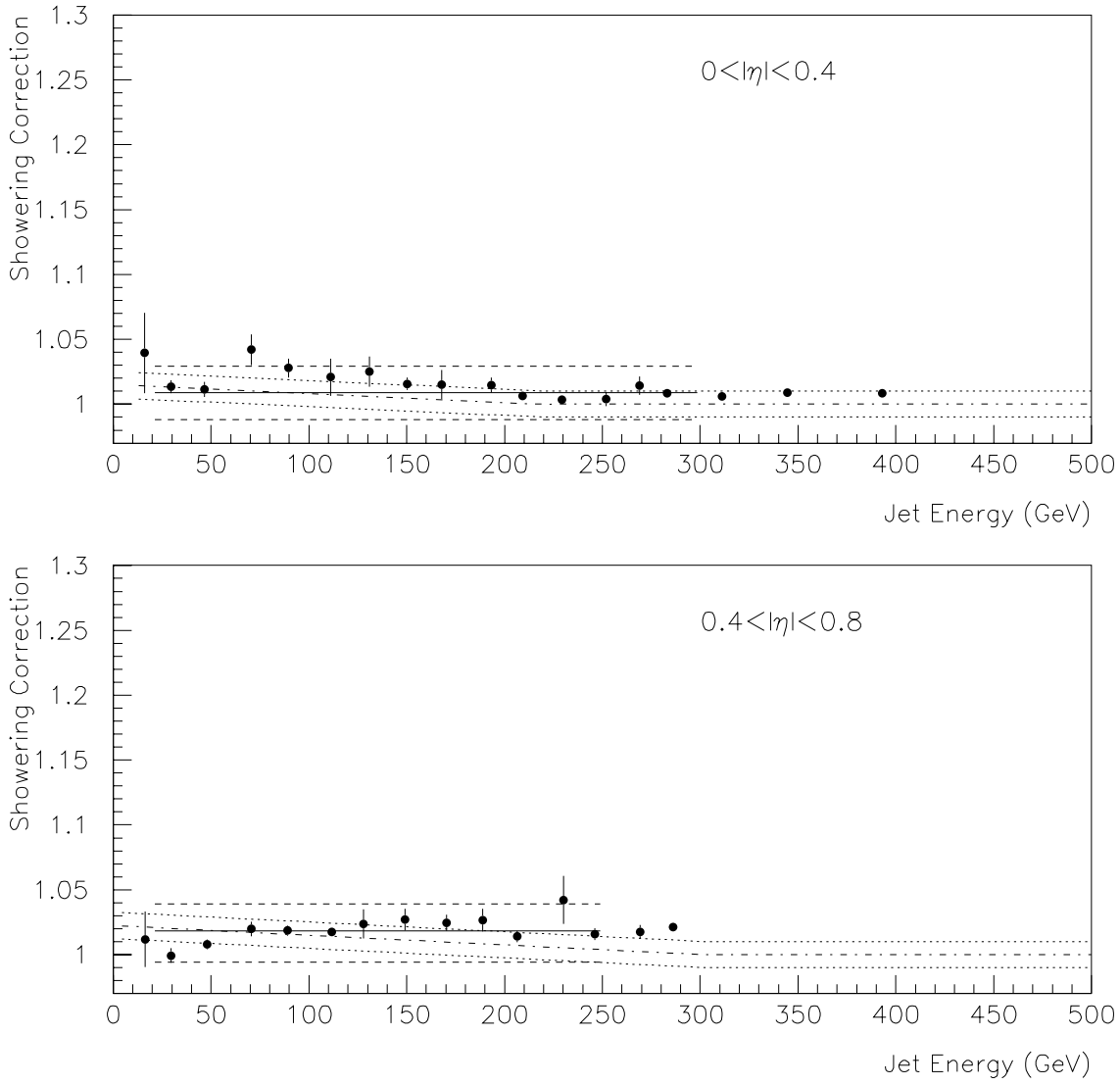

Figure 24: The showering correction in terms of response–corrected jet energy. The dashed lines show the total uncertainty on the correction. Also shown is the showering correction in CAFIX 5.1 (dashed–dotted lines) and its uncertainty (dotted lines).

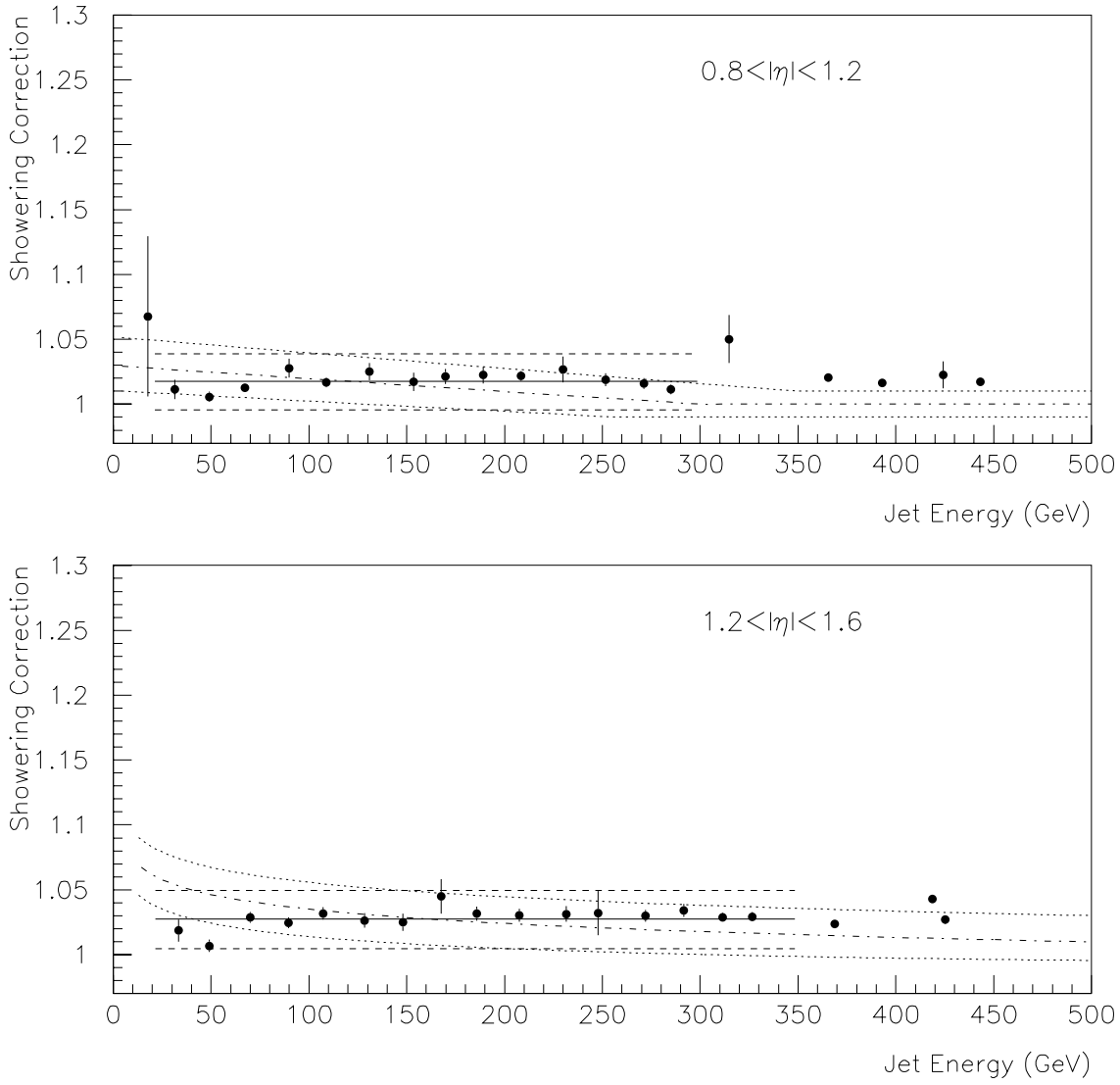

Figure 24: The showering correction in terms of response–corrected jet energy. The dashed lines show the total uncertainty on the correction. Also shown is the showering correction in CAFIX 5.1 (dashed–dotted lines) and its uncertainty (dotted lines).

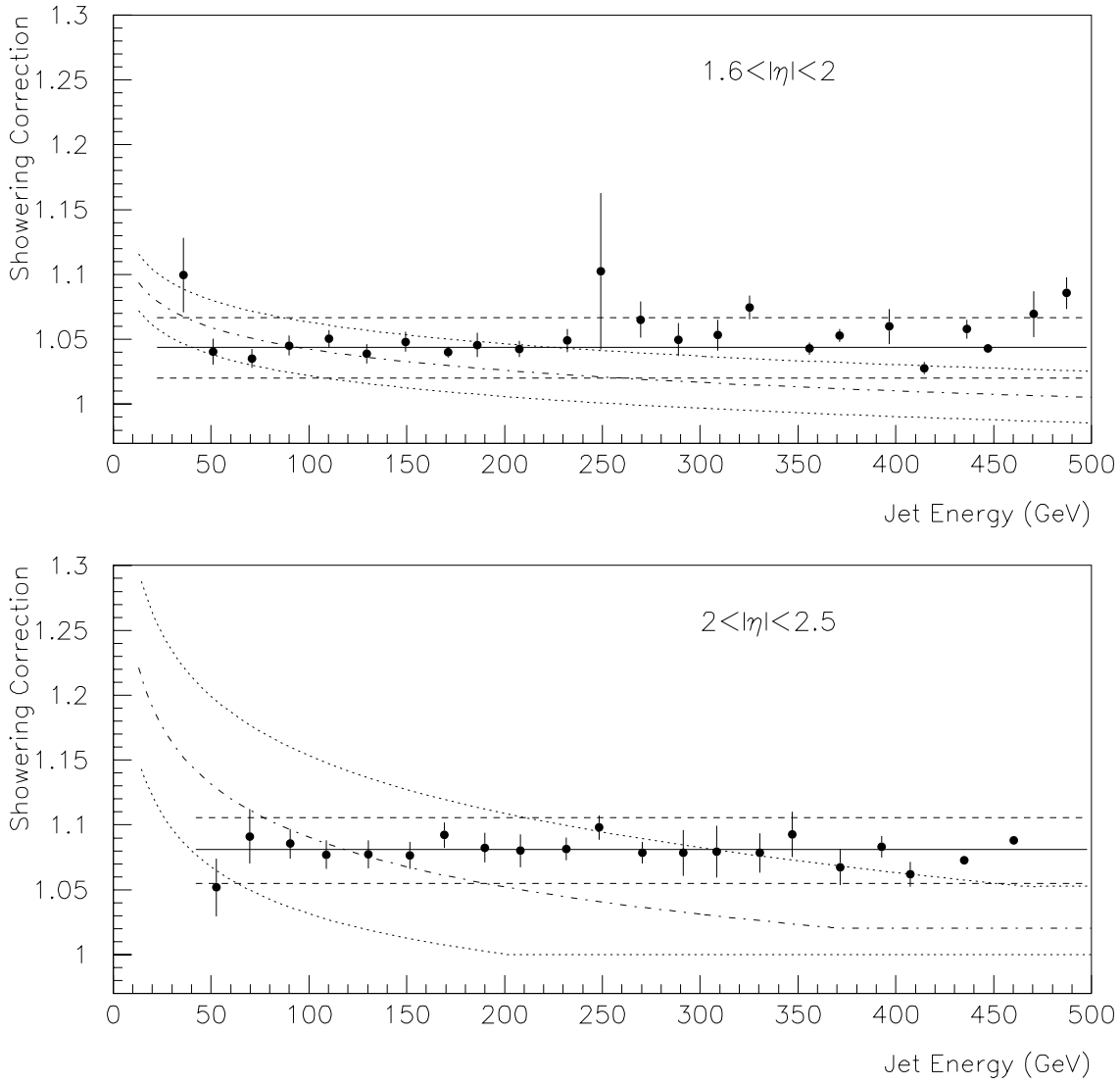

Figure 24: The showering correction in terms of response–corrected jet energy. The dashed lines show the total uncertainty on the correction. Also shown is the showering correction in CAFIX 5.1 (dashed–dotted lines) and its uncertainty (dotted lines).

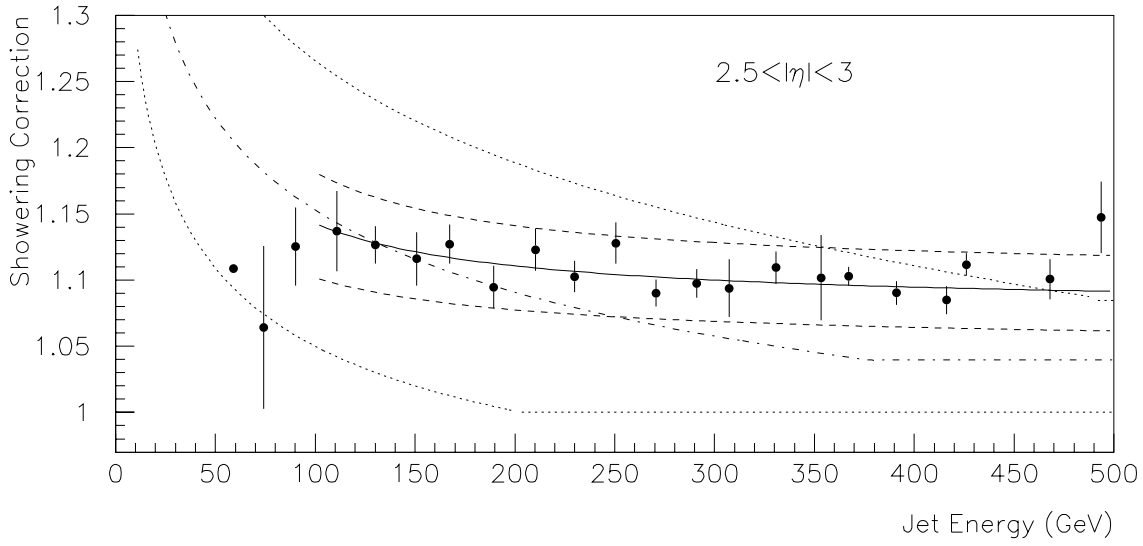

Figure 24: The showering correction in terms of response–corrected jet energy. The dashed lines show the total uncertainty on the correction. Also shown is the showering correction in CAFIX 5.1 (dashed–dotted lines) and its uncertainty (dotted lines).

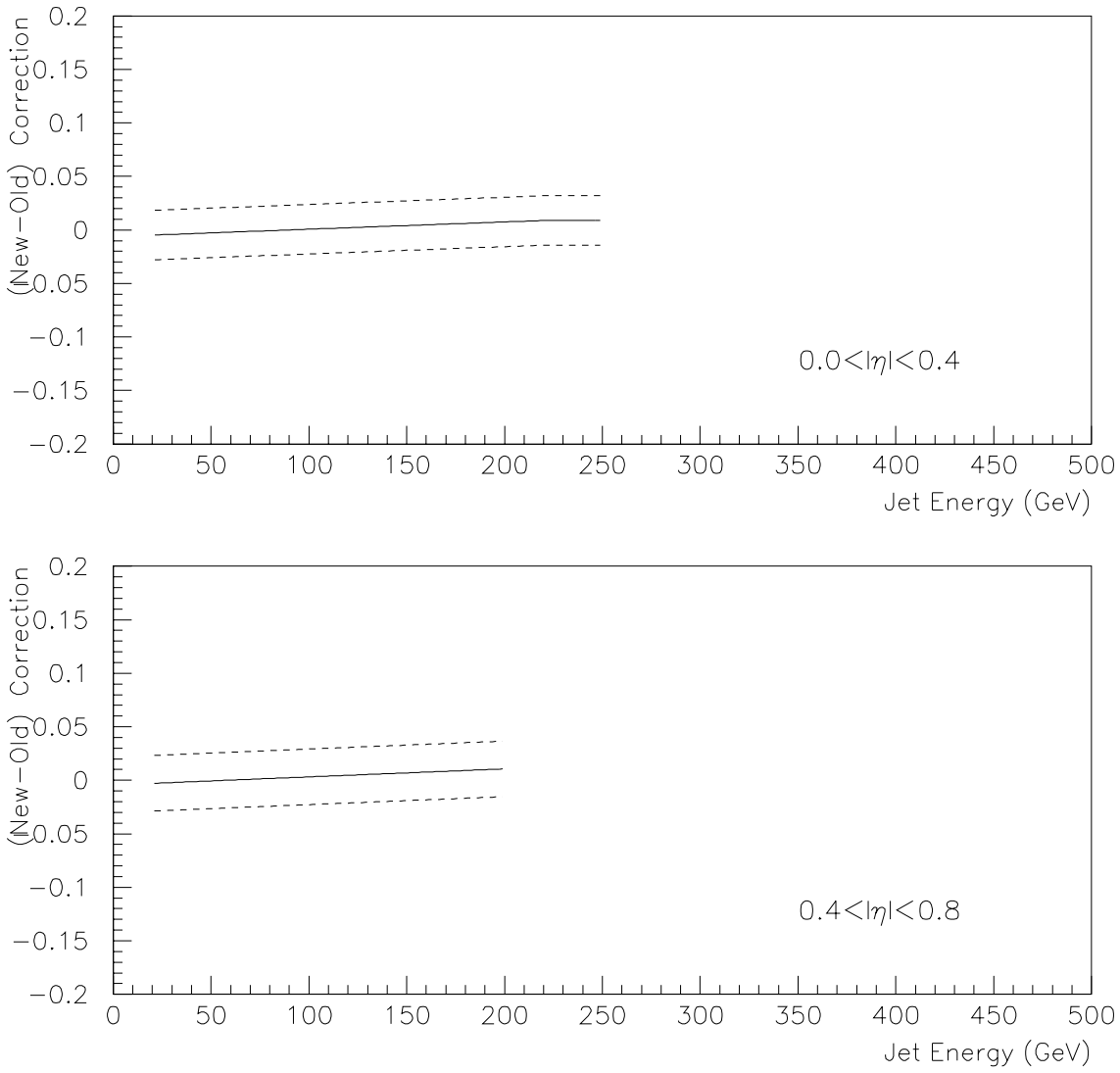

Figure 25: The difference between the new showering correction and in the one in CAFIX 5.1, in terms of response–corrected jet energy. The dashed lines represent the errors of the two corrections, added in quadrature.

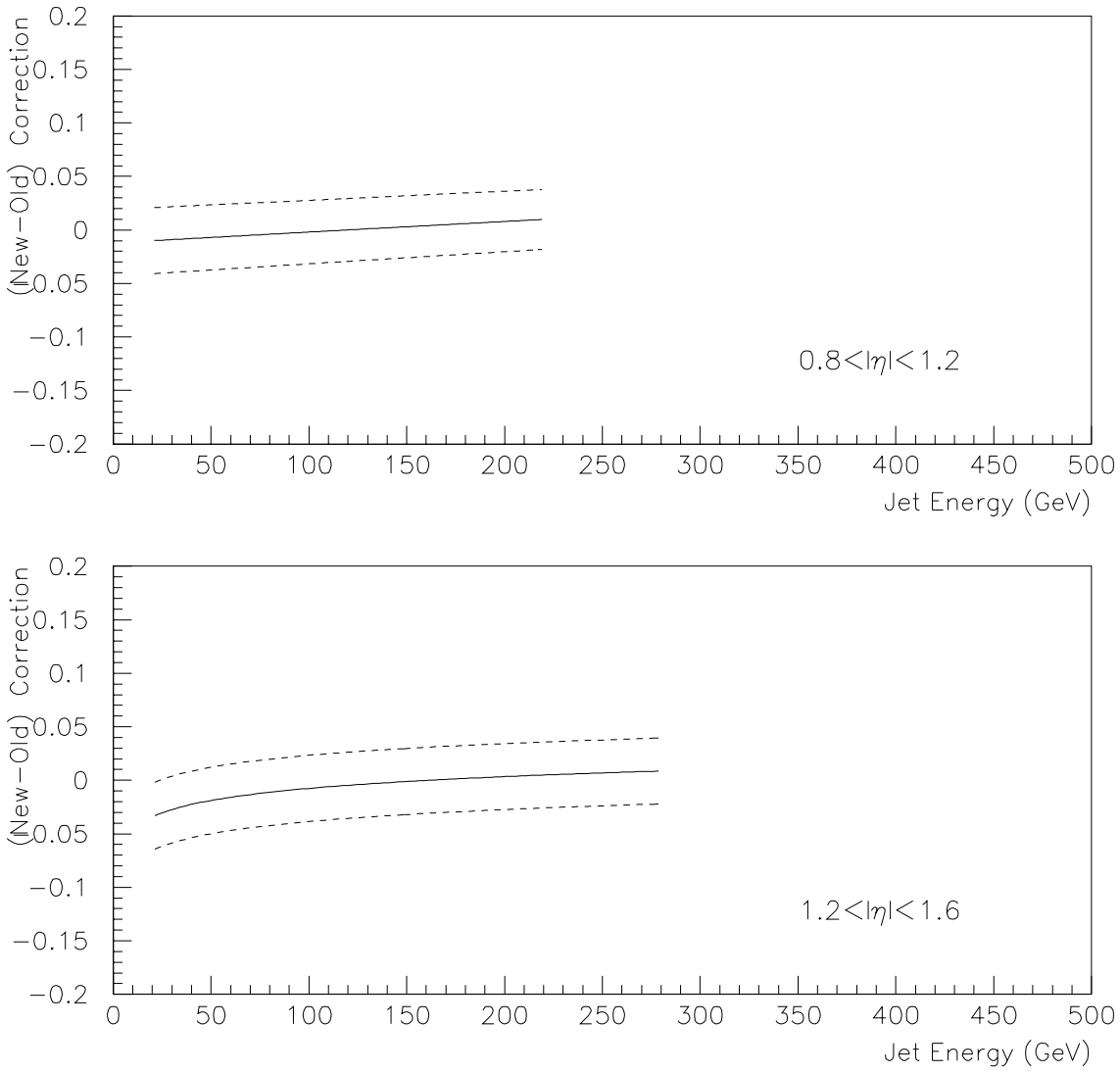

Figure 25: The difference between the new showering correction and in the one in CAFIX 5.1, in terms of response–corrected jet energy. The dashed lines represent the errors of the two corrections, added in quadrature.

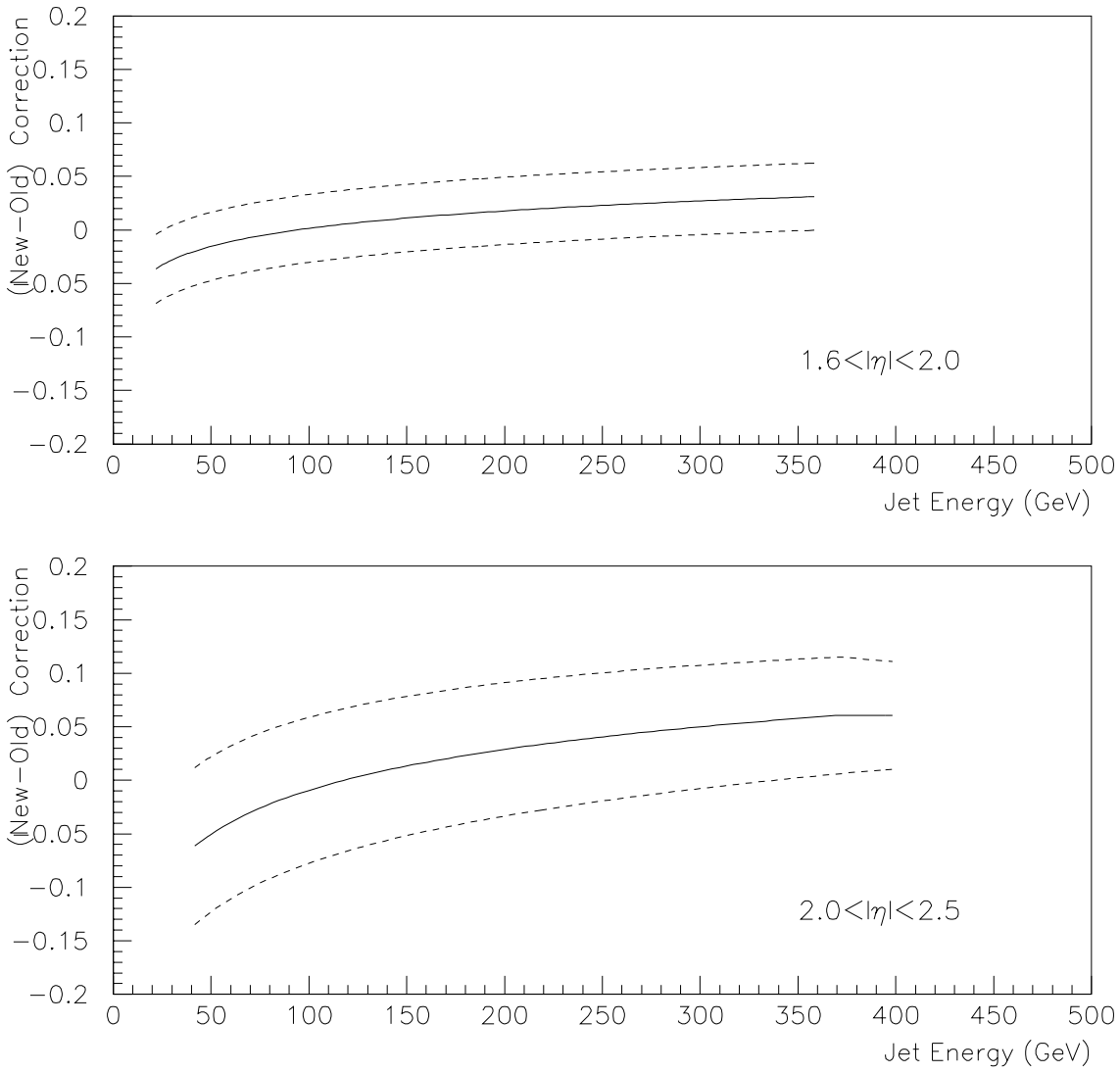

Figure 25: The difference between the new showering correction and in the one in CAFIX 5.1, in terms of response–corrected jet energy. The dashed lines represent the errors of the two corrections, added in quadrature.

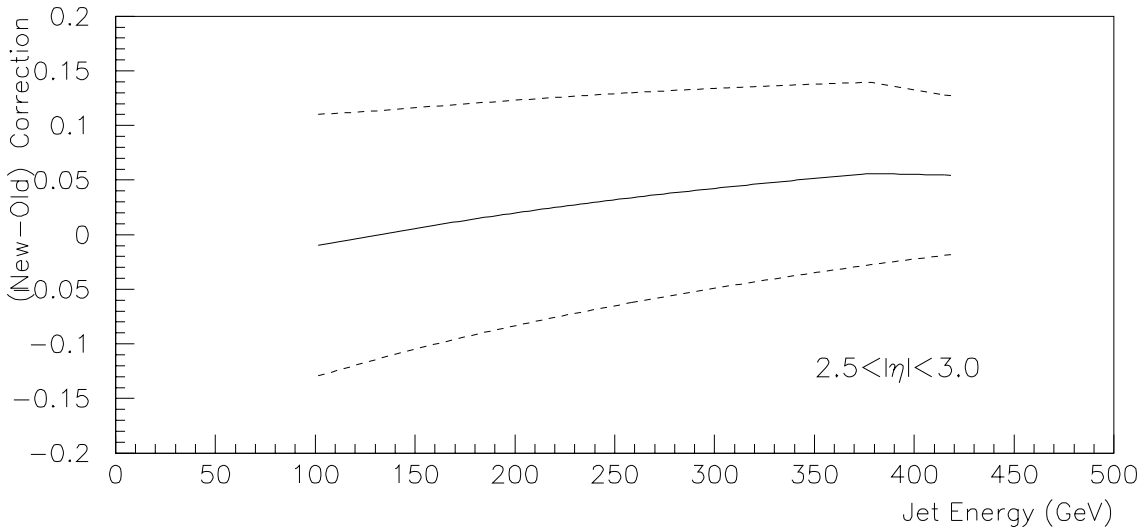

Figure 25: The difference between the new showering correction and in the one in CAFIX 5.1, in terms of response–corrected jet energy. The dashed lines represent the errors of the two corrections, added in quadrature.

7 The Showering Correction at $\sqrt{s} = 630$ GeV

Collider data during Tevatron Run Ic have been taken at a center–of–mass energy of 630 GeV. For the calibration of the jet energy scale of these data, a different offset energy has been derived, whereas the calorimeter energy response has been shown to be the same with the one at $\sqrt{s} = 1800$ GeV [9]. To test the showering correction at the lower center–of–mass energy, we generate an additional HERWIG sample and pass it through the detector simulation. We use two minimum parton p_T thresholds of 20 and 30 GeV at the generation level, and five η-bins ($|\eta| < 2$), which results in a total of 1,250 events. The results for the showering correction at 630 GeV are shown in Fig. 26. For comparison purposes, the showering correction at 1800 GeV is also shown in the plots. The errors shown in the figure are only due to the fitting. We conclude that the showering correction at $\sqrt{s} = 630$ GeV is consistent with the correction at 1800 GeV. Thus, we can use the latter at both center–of–mass energies.

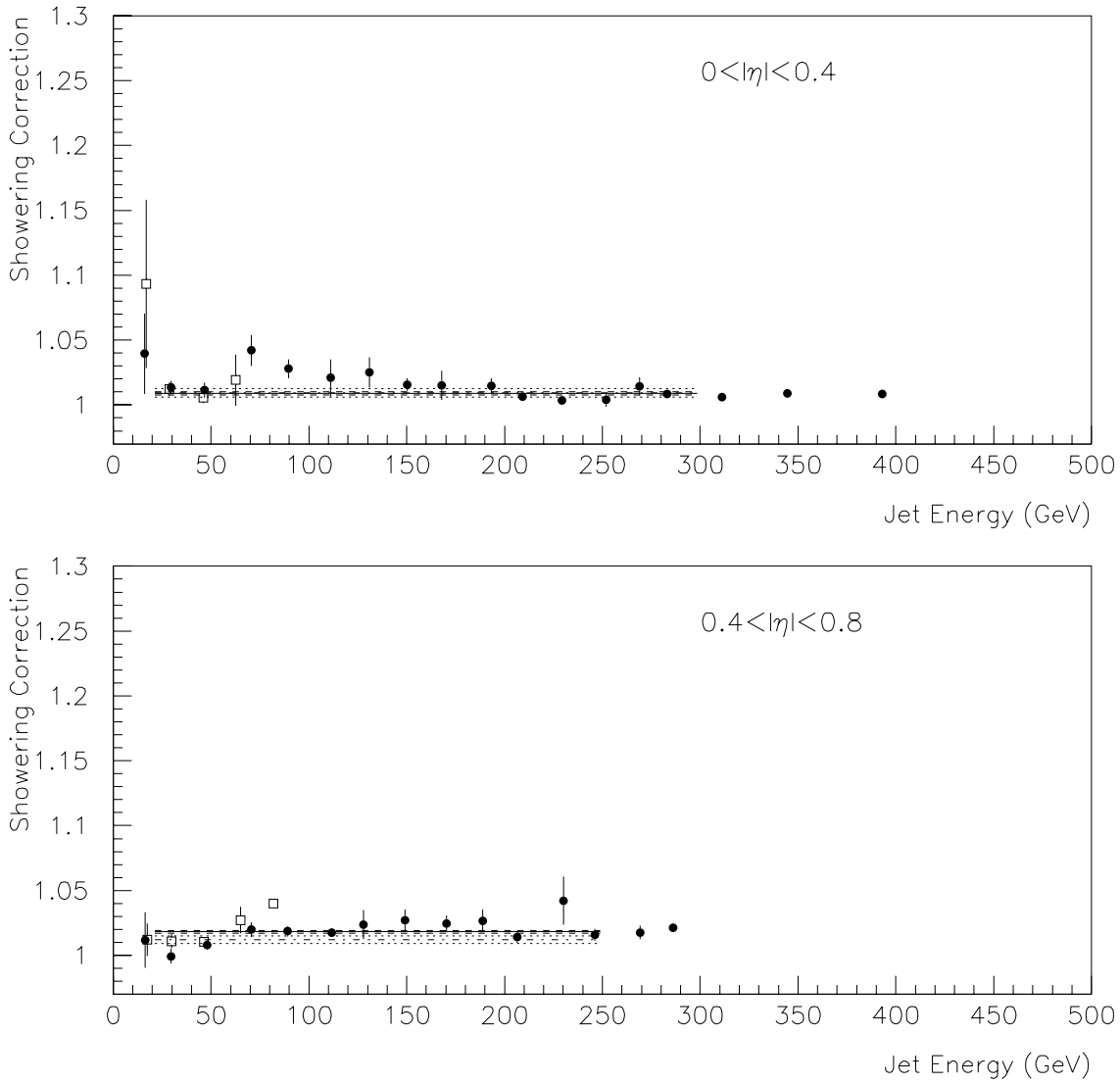

Figure 26: The showering correction in terms of response–corrected jet energy at $\sqrt{s} =$ 1800 GeV (full circles) and 630 GeV (open squares). The solid and dashed–dotted lines represent the fit to the corrections, respectively. The dashed and dotted lines represent the fitting errors.

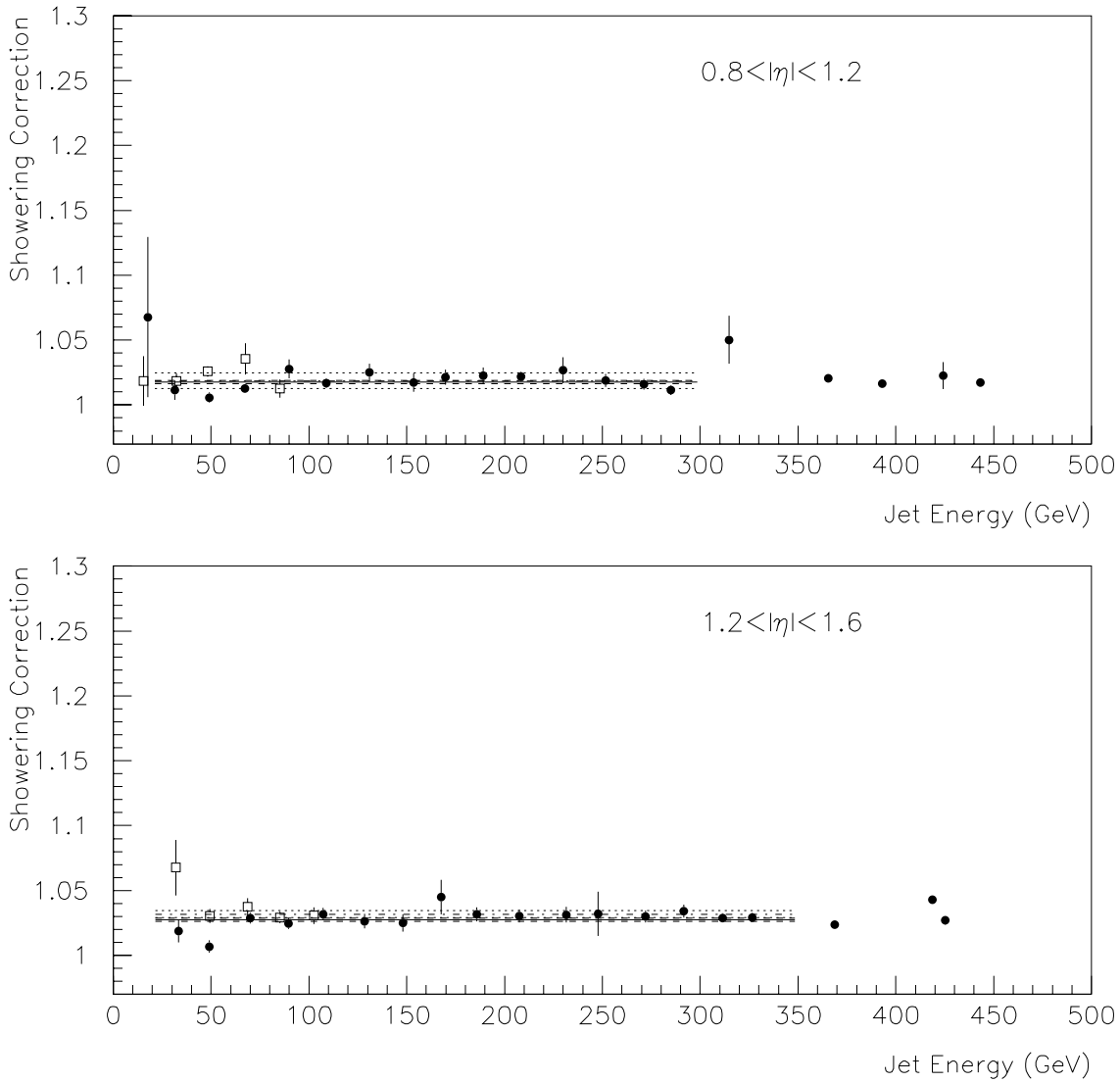

Figure 26: The showering correction in terms of response–corrected jet energy at $\sqrt{s} =$ 1800 GeV (full circles) and 630 GeV (open squares). The solid and dashed–dotted lines represent the fit to the corrections, respectively. The dashed and dotted lines represent the fitting errors.

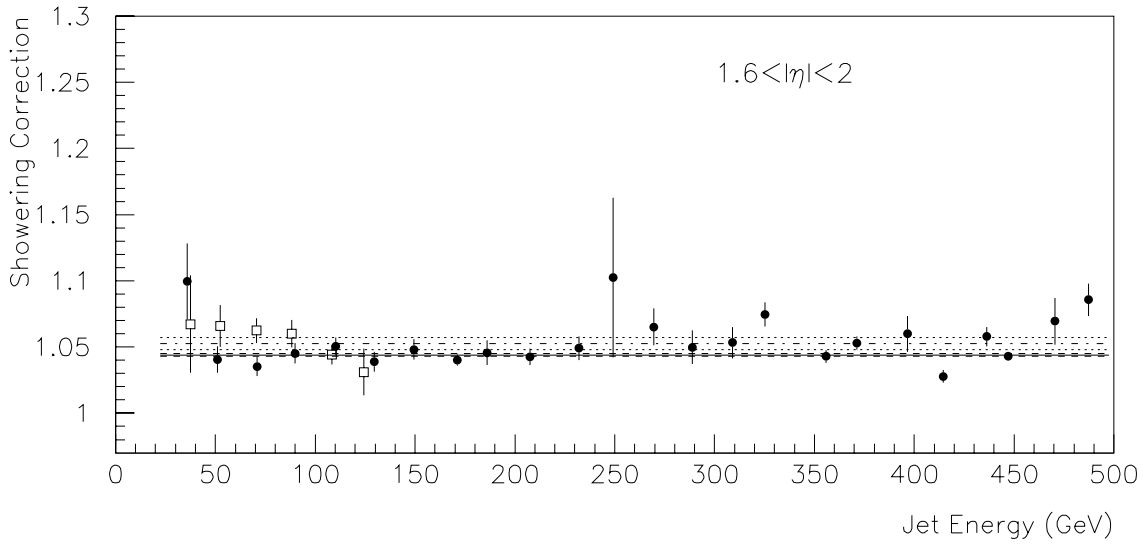

Figure 26: The showering correction in terms of response–corrected jet energy at $\sqrt{s} =$ 1800 GeV (full circles) and 630 GeV (open squares). The solid and dashed–dotted lines represent the fit to the corrections, respectively. The dashed and dotted lines represent the fitting errors.

8 Implementation of the Showering Correction

The showering correction has been derived in eight pseudorapidity bins as a function of jet energy. The correction in CAFIX 5.1, derived in a similar way, was implemented into CAFIX using a linear interpolation between the eight rapidity bins for a given jet energy. That method, however, produces a distorted shape for the correction and is subject to fluctuations in some η-bins. For the new correction, we replace the linear interpolation with a smooth fit versus pseudorapidity:

$$corr(\eta) = 1.0088 + A \cdot \eta^2 + B \cdot \eta^4 \tag{13}$$

The above equation would be exact if the showering correction was independent of jet energy in all pseudorapidities. This is true, however, only for $|\eta| < 2.5$. In the last two η-bins, $2.5 < |\eta| < 3.5$, the correction becomes a function of jet energy. To account for that, we replace eq. (13) with:

$$corr(\eta, E) = 1.0088 + A(E) \cdot \eta^2 + B(E) \cdot \eta^4 \tag{14}$$

Thus, we fit the showering correction as a function of pseudorapidity for several jet energies, and then fit the parameters A and B themselves as a function of energy. Fig. 27 shows the fits for the correction versus $|\eta|$ for selected jet energies (energies lower than 100 GeV are not relevant for the forward pseudorapidity bins, where the energy dependence turns on). Fig. 28 shows similar fits plotted together and for a larger number of jet energies. We see that the energy dependence smoothly turns on for approximately $|\eta| > 1.75$. The small spread observed at lower pseudorapidities is an artifact of the fitting and will be removed later. Fig. 29 shows the fitting parameters A and B for different jet energies. These are fitted in turn, using the following functions:

$$A(E) = a_1 \cdot \tanh(a_2 \cdot (E + a_3)) \tag{15}$$

$$B(E) = b_1 + e^{(b_2 + b_3 \cdot E)} \tag{16}$$

After extracting the set of parameters (a_1, a_2, a_3) and (b_1, b_2, b_3) and substituting equations (15) and (16) into eq. (14), we verify that the outcome of the double fitting perfectly matches the fitted functions of Fig. 27. To avoid the small spread for different jet energies at $|\eta| < 1.75$, we choose the function for $E = 160$ GeV (which is in the middle of the range spanned by different energies) as the showering correction for jets of all energies and pseudorapidities smaller than 1.75. For higher pseudorapidities, we allow the energy dependence. Examples are shown in Fig. 30. No discontinuity is observed at $|\eta| = 1.75$. Fig. 31 shows the final correction for a larger number of jet energies.

To derive the fits that correspond to the uncertainties of the showering correction, we repeat the above procedure using as starting points for the fits the lower/upper correction due to the fitting error (section 4.4) and the lower/upper correction due to the variation of the jet limit (section 4.5). In the second case, we substitute the constant 1.0088 in eq. (14) by 1.0040 and 1.0122, respectively. The results are shown in Fig. 32. The central solid lines correspond to the nominal correction. The dotted lines correspond to the fitting error and the dashed lines to the systematic error due to the variation of the jet limit. The outer solid lines show the total uncertainty in the correction, including the

2% error from the MC–data comparison (section 4.6). For all energies, the correction and the errors for $|\eta| < 1.75$ correspond to the fits for jet energy 160 GeV. The correction and errors for $|\eta| > 1.75$ are different for different energies.

The set of parameters (a_1, a_2, a_3) and (b_1, b_2, b_3) for the nominal/lower/upper showering correction are given in Table 8.

Fitting Parameters for $corr(\eta, E)$						
	a_1	a_2	a_3	b_1	b_2	b_3
Nominal	0.01029	0.00595	61.45354	0.00027	-6.01300	-0.01053
Lower Fitting	0.00980	0.00540	79.93316	0.00026	-6.19716	-0.00935
Upper Fitting	0.01077	0.00643	47.23191	0.00028	-5.80752	-0.01179
Lower Jet Limit	0.00729	0.00853	-20.78278	0.00044	-5.44853	-0.01485
Upper Jet Limit	0.01231	0.00466	115.06042	0.00018	-6.10381	-0.00845

Table 8: Fitting parameters for the functional form of the showering correction as given by equations (14), (15) and (16).

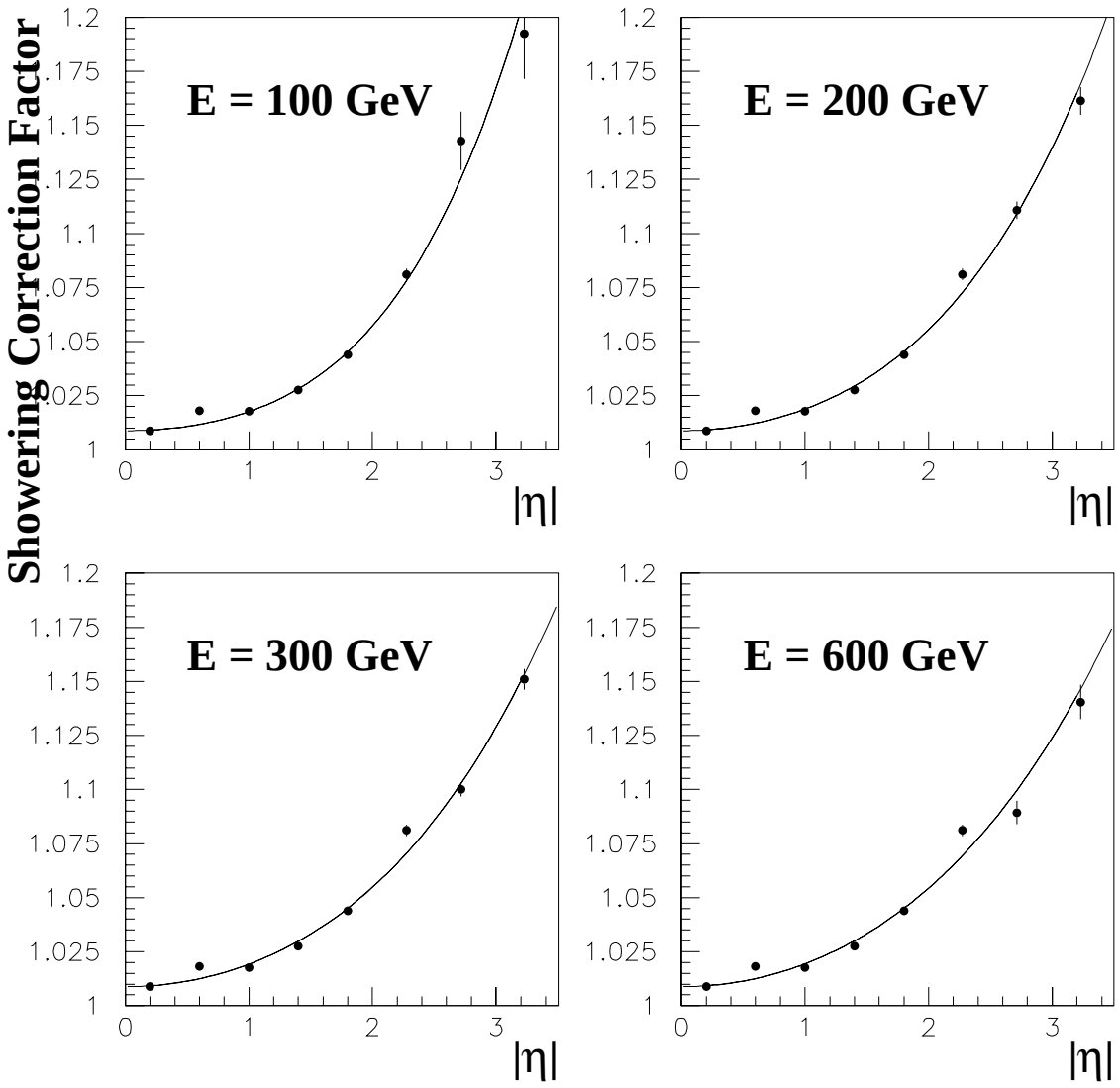

Figure 27: The showering correction as a function of absolute pseudorapidity for different jet energies. The smooth functions represent the fits to the correction versus $|\eta|$, as described in the text.

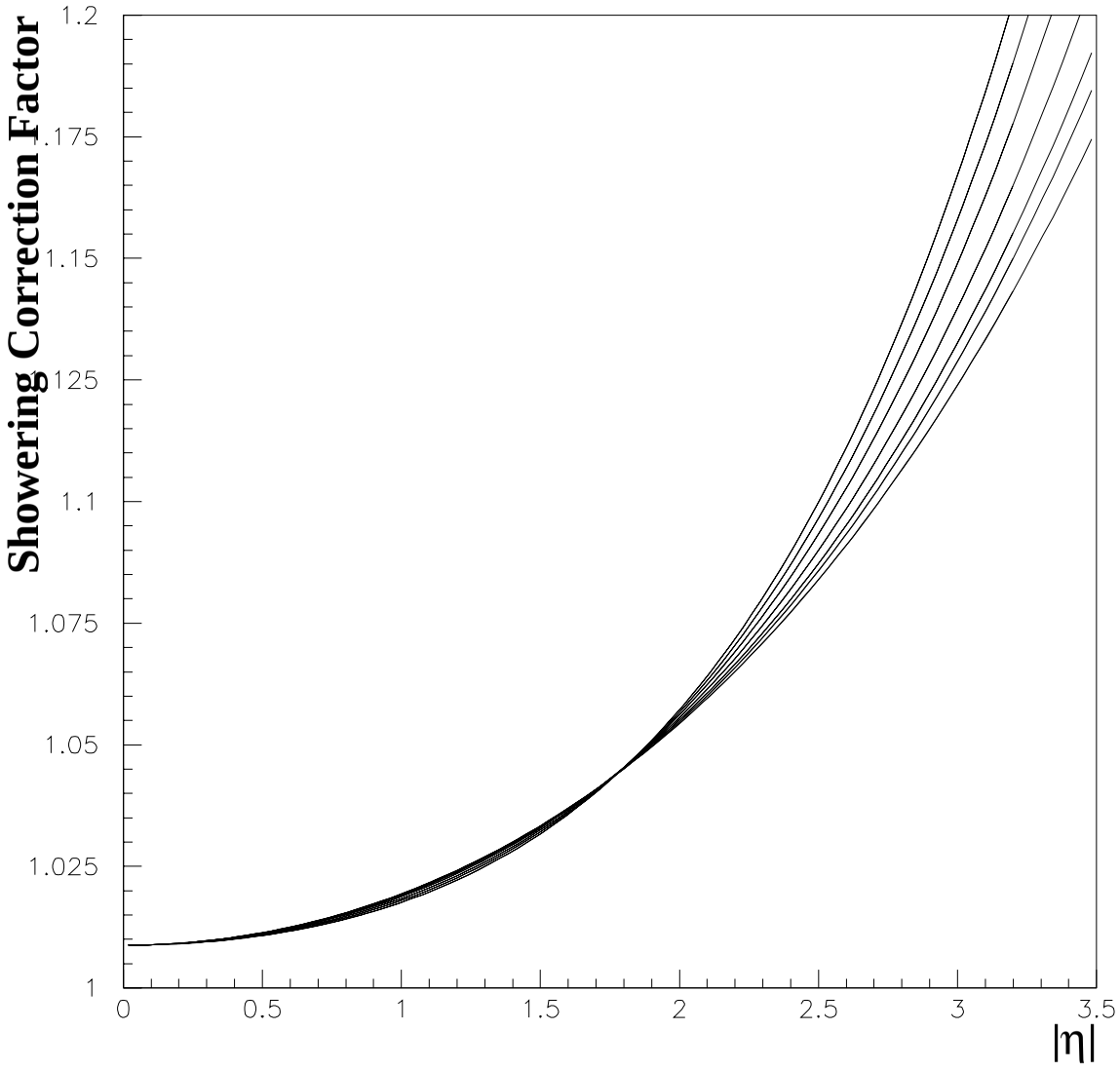

Figure 28: Fits to the showering correction as a function of absolute pseudorapidity for different jet energies: 100, 130, 160, 200, 250, 300 and 600 GeV (from top to bottom).

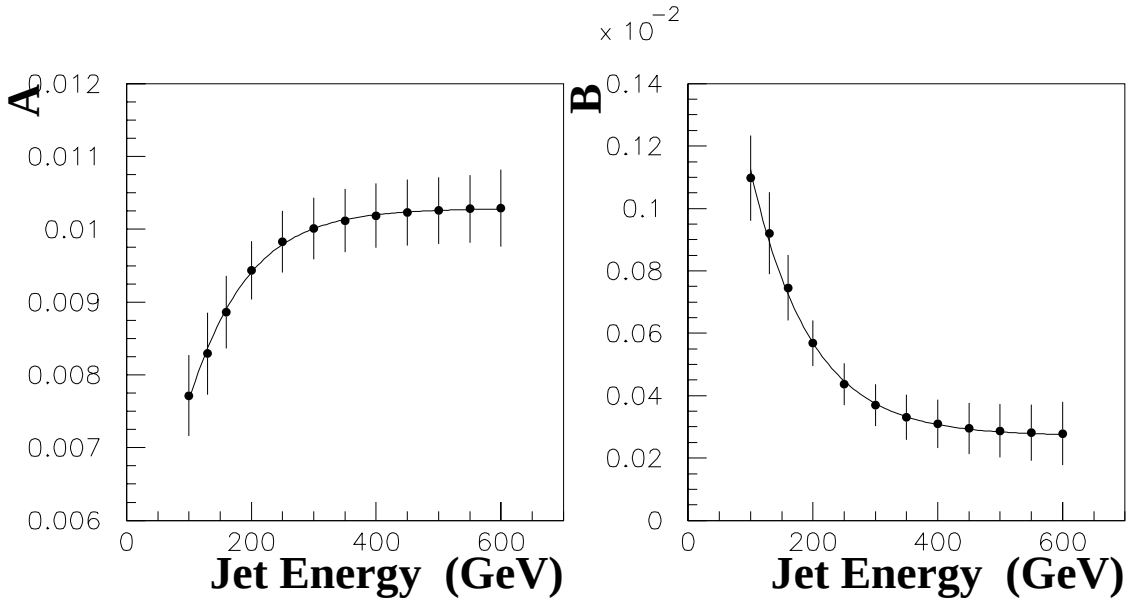

Figure 29: Fits to parameters A and B as a function of jet energy.

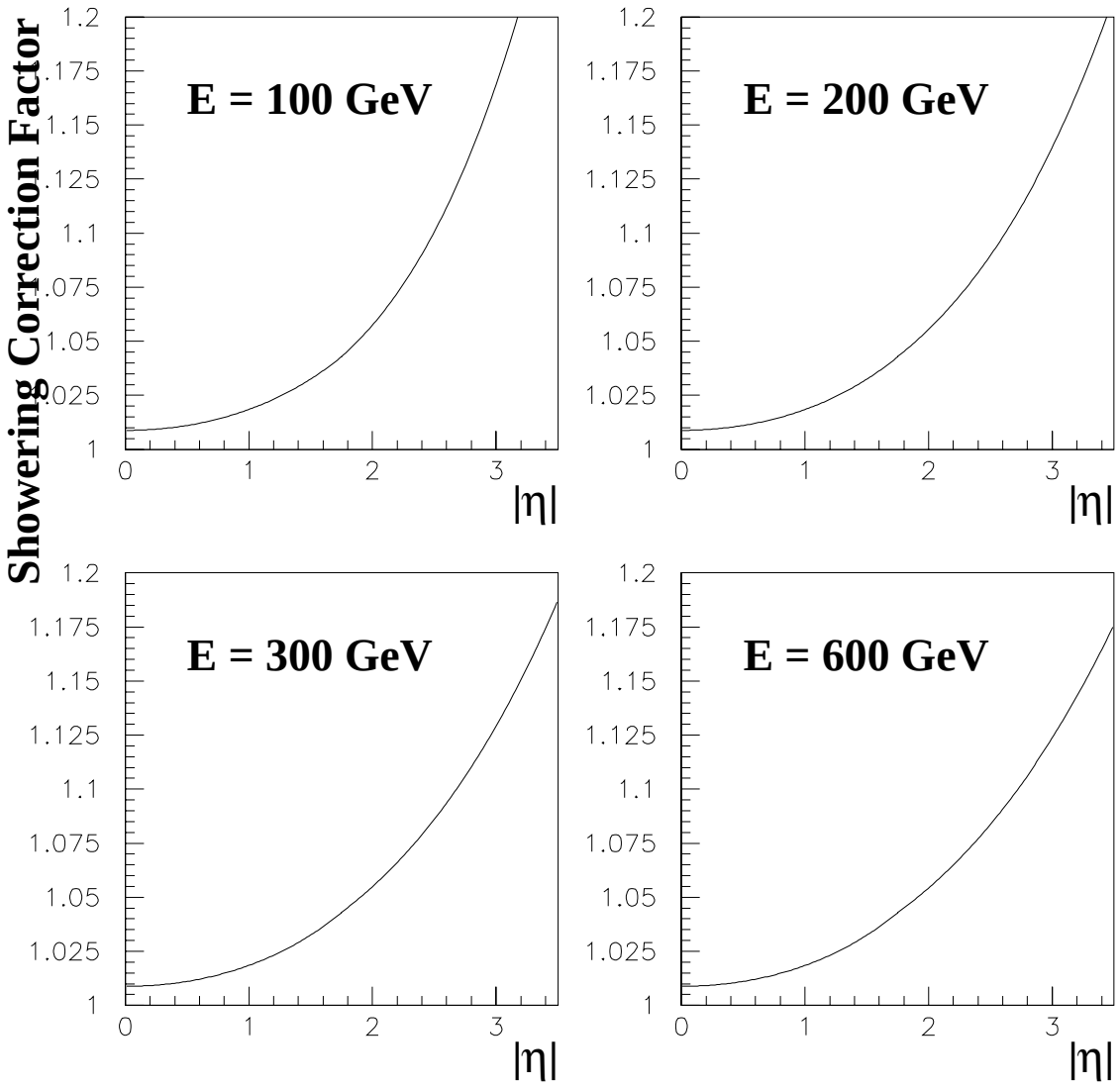

Figure 30: The output of the fitting (versus jet pseudorapidity) for the showering correction for different jet energies. For all energies, the correction for $|\eta| < 1.75$ corresponds to the fit for jet energy 160 GeV. The correction for $|\eta| > 1.75$ is different for different energies. No discontinuity in the function is observed at $|\eta| = 1.75$.

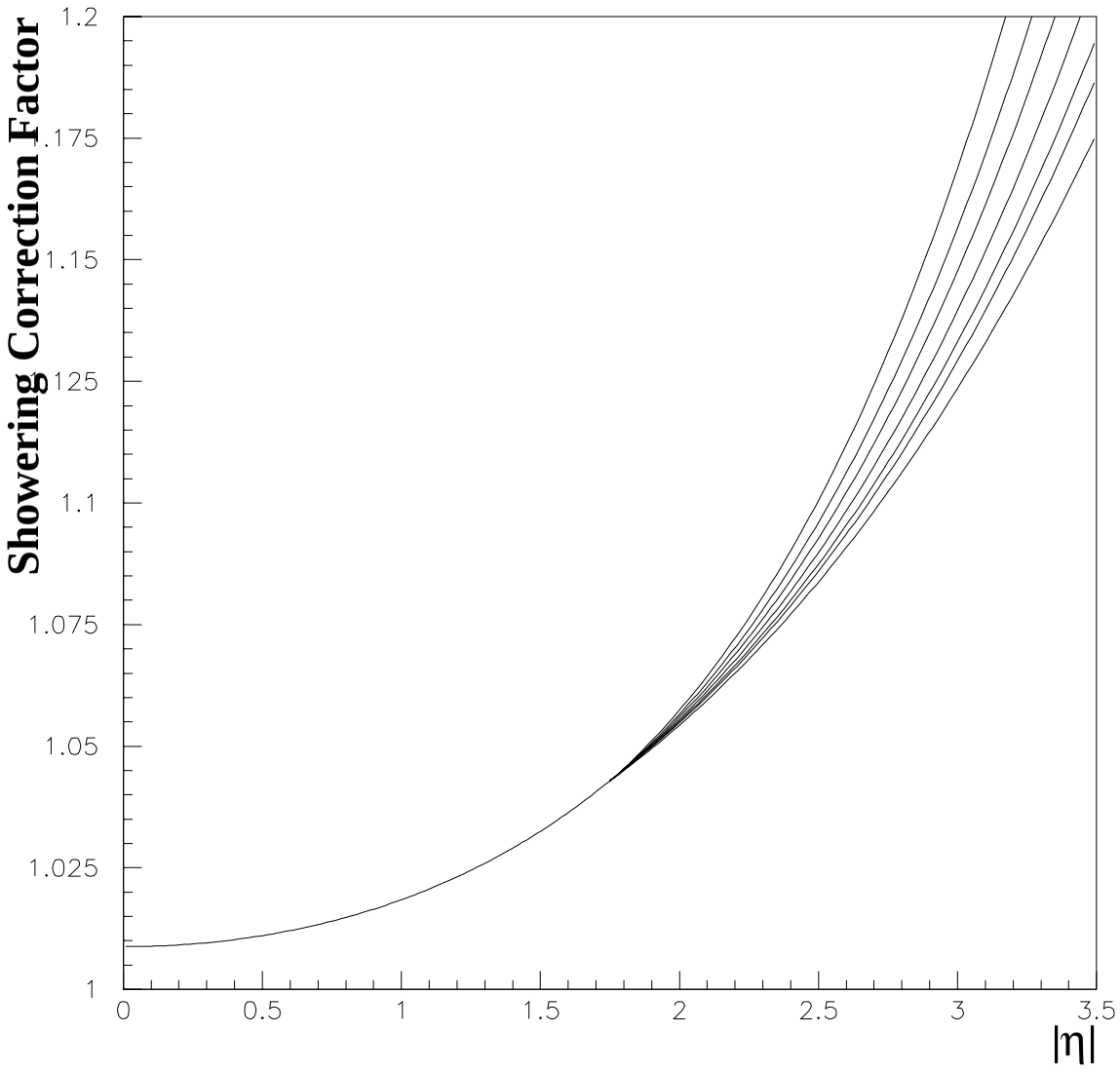

Figure 31: The output of the fitting (versus jet pseudorapidity) for the showering correction for different jet energies: 100, 130, 160, 200, 250, 300 and 600 GeV (from top to bottom). For all energies, the correction for $|\eta| < 1.75$ corresponds to the fit for jet energy 160 GeV. The energy dependence is turned on for $|\eta| > 1.75$. No discontinuity in the function is observed at $|\eta| = 1.75$.

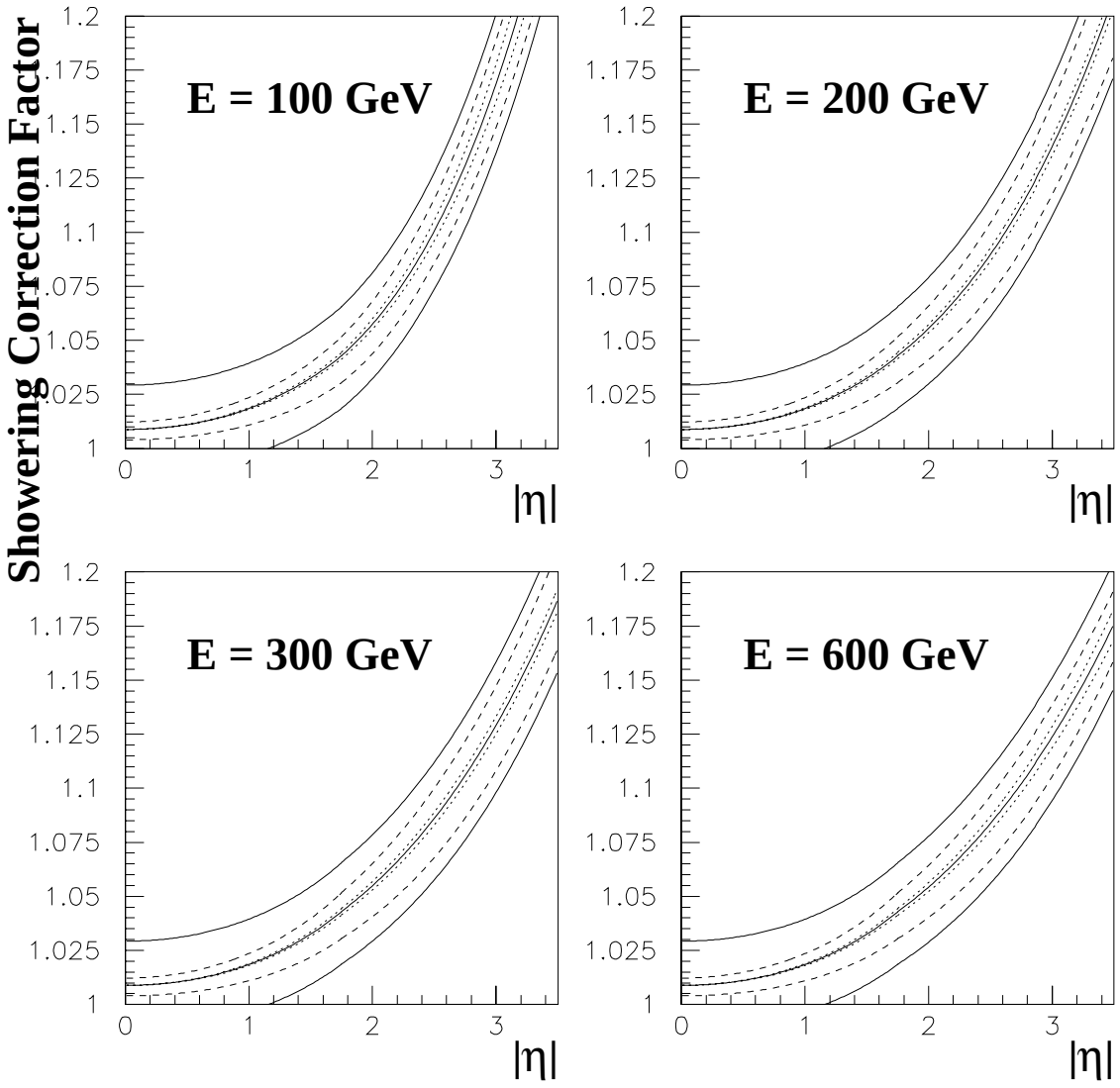

Figure 32: The output of the fitting (versus jet pseudorapidity) for the showering correction for different jet energies. The central solid line corresponds to the nominal correction. The dotted lines correspond to the fitting error and the dashed lines to the systematic error due to the variation of the jet limit. The outer solid lines show the total uncertainty in the correction (including the 2% error from the MC–data comparison). For all energies, the correction and the errors for $|\eta| < 1.75$ correspond to the fits for jet energy 160 GeV. The correction and errors for $|\eta| > 1.75$ are different for different energies.

9 Conclusions

We have derived anew the component of the jet energy scale that corrects for showering effects during the development of the jets in the calorimeter. The new correction is extracted from Monte Carlo events passed through a detailed simulation of the DØ detector. The similarity of the Monte Carlo to the data has been established by comparing the jet showering profiles between the two. The use of Monte Carlo events provides valuable control over the systematics of the correction, and reduces significantly its uncertainty in the forward pseudorapidity regions, where the showering effects are of most importance.

Acknowledgments

We are grateful to Ransom Stephens for providing the computing farm at the University of Texas at Arlington for the "plate-level" GEANT simulation of the detector over a long period of months. Special thanks to John Womersley for his valuable insight into the DØ Monte Carlo. Discussions with Daniel Elvira on the CAFIX 5.1 correction, and the help of Rob Snihur with the latest version of HERWIG, are greatly appreciated.

References

[1] The DØ Collaboration, Nucl. Instr. and Methods A 338 (1994) 185.

[2] The DØ Collaboration, "Determination of the Absolute Energy Scale in the DØ Calorimeters", Accepted by Nucl. Instr. and Methods A; Fermilab–Pub–97/330–E, hep–ex/9805009.

[3] G. Marchesini, B.R. Webber, G. Abbiendi, I.G. Knowles, M.H. Seymour and L. Stanco, Computer Phys. Commun. 67 (1992) 465.

[4] "GEANT – Detector Description and Simulation Tool", CERN Program Library Long Writeup W5013 (1993).

[5] J. Womersley, "The DØ Monte Carlo", proceedings of the *XXVI International Conference on High Energy Physics*, Dallas, Texas, 1992; Fermilab–Conf–92/306.

[6] S.J. Durston, Ph.D. Thesis, University of Rochester, 1993.

[7] V.D. Elvira, private communication.

[8] J. Womersley, private communication.

[9] A. Goussiou and J. Krane, "Jet Energy Scale at DØ for $\sqrt{s} = 630$ GeV", DØ Note 3288.